Spring 2015

Validation and applications of discrete element analysis in the hip joint

Kevin Charles Townsend
University of Iowa

VALIDATION AND APPLICATIONS OF DISCRETE ELEMENT ANALYSIS IN THE HIP JOINT

by

Kevin Charles Townsend

A thesis submitted in partial fulfillment
of the requirements for the Master of
Science degree in Biomedical Engineering
in the Graduate College of
The University of Iowa

May 2015

Thesis Supervisor: Assistant Professor Jessica E. Goetz

Graduate College
The University of Iowa
Iowa City, Iowa

CERTIFICATE OF APPROVAL

_____

MASTER'S THESIS

_____

This is to certify that the Master's thesis of

Kevin Charles Townsend

has been approved by the Examining Committee
for the thesis requirement for the Master of Science
degree in Biomedical Engineering at the May 2015 graduation.

Thesis Committee: _____
Jessica E. Goetz, Thesis Supervisor

_____
Nicole Grosland

_____
Tae-Hong Lim

ACKNOWLEDGMENTS

I would first and foremost like to thank my research supervisor Dr. Jessica Goetz for her guidance and support in my research work. Dr. Goetz's knowledge and expertise were paramount to the work I have accomplished. The encouragement and motivation I received has helped me develop as a graduate-level researcher. Additionally, I would like to thank Dr. Jim Rudert for his contributions and detail-oriented thinking in developing and performing the validation testing methods.

I am greatly appreciative of the other members of my thesis committee, Dr. Nicole Grosland and Dr. Tae-Hong Lim for their time and perspectives on my work. I would also like to thank each member of the Orthopaedic Biomechanics Lab, as many have lent advice, ideas, and feedback regarding my research. I would like to give a special thanks to Andrew Kern for his work in developing and helping me understand the DEA algorithm and segmentation code. The work presented in this thesis is built upon previous work in the University of Iowa Orthopaedic Biomechanics Laboratory, specifically development of DEA and validation in the knee and ankle. Funding for this research was provided by a grant from the NIH/NIAMS AR000533. Finally, I would like to thank my friends, family and girlfriend for their love and support in my academic journey.

ABSTRACT

Osteoarthritis is a progressive degenerative joint disease which causes pain, inflammation, and eventual loss of joint function. This debilitating disease affects approximately 3% of U.S. adults over 30 years old, with direct medical costs of over $100 billion each year. Post-traumatic osteoarthritis is a sub-set of osteoarthritis initiated by injuries such as a fracture of the joint surface. When a surgeon reconstructs a fractured joint, there are often residual incongruities on the surface, which can lead to elevated contact stresses. Increased cartilage contact stress has been shown to be a major risk factor for developing post-traumatic osteoarthritis. Computational modeling offers a method of detecting elevated contact stresses and thereby assessing the associated risk of a patient developing post-traumatic osteoarthritis. Discrete element analysis (DEA) is a computational method capable of fast and reliable contact stress predictions that has been used successfully to predict knee and ankle osteoarthritis. The purpose of this study was to validate the accuracy of DEA models of both intact and fractured hips by directly comparing experimentally measured intra-articular contact stresses in human cadaveric hips to corresponding DEA predictions. Overall correlation was greater than 90% for both intact and fractured hips. The validated DEA algorithm was then applied to a series of 3 patients with a hip fracture and another series of 19 patients with surgical hip re-alignment. As anticipated, changes in contact stress correlated well with pain and function ($p < 0.05$). This validated DEA model appears to be a clinically useful tool for identifying patients who are at higher risk for developing osteoarthritis as a result of elevated joint contact stresses.

PUBLIC ABSTRACT

Osteoarthritis is a progressive degenerative joint disease which causes pain, inflammation, and eventual loss of joint function. Post-traumatic osteoarthritis is a sub-set of osteoarthritis initiated by injuries such as a fracture of the joint surface. When a surgeon reconstructs a fractured joint, there are often remaining imperfections in the surface, which can lead to elevated contact stresses. Increased cartilage contact stress has been shown to be a major risk factor for developing post-traumatic osteoarthritis. Computational modeling offers a method of detecting elevated contact stresses and thereby assessing the associated risk of a patient developing post-traumatic osteoarthritis. Discrete element analysis (DEA) is a computational method capable of fast and reliable contact stress predictions that has been used successfully to predict knee and ankle osteoarthritis. The purpose of this study was to validate the accuracy of DEA models of both intact and fractured hips by directly comparing experimentally measured contact stresses in human cadaveric hips to corresponding DEA predictions. The validated DEA algorithm was then applied to a small series of patients with a hip fracture and another series of patients with surgical hip re-alignment. As anticipated, changes in contact stress correlated well with pain and function. This validated DEA model appears to be a clinically useful tool for identifying patients who are at higher risk for developing osteoarthritis as a result of elevated joint contact stresses.

TABLE OF CONTENTS

LIST OF TABLES

LIST OF FIGURES

CHAPTER 1: INTRODUCTION AND BACKGROUND

1.1 Introduction to Osteoarthritis

Osteoarthritis (OA) is a joint disease caused by progressive degeneration of articular cartilage and subchondral bone. The global prevalence of hip and knee OA is estimated to be 3.8% and the prevalence of hip OA in U.S. adults 30 years or older is approximately 3% [1, 2]. This disease affects millions of people, lowering their quality of life. OA patients suffer from joint pain and inflammation which can progress to loss of function in advanced stages [3]. Along with symptoms affecting an individual's quality of life, OA is responsible for substantial societal and economic costs. It is estimated that the total annual direct medical costs of OA in the U.S. is greater than $100 billion [2]. Indirect medical costs incurred due to loss of work productivity, care seeking, and care by nonprofessionals is estimated to be 1.5 times the direct cost of medical care, or $150 billion per year [4]. These costs are expected to rise due to an aging population and increased rates of obesity, two risk factors closely associated with OA. Other risk factors include poor nutrition, genetic predisposition, repetitive intense joint loading, joint dysplasia, and joint injury [1-3].

OA is the complex result of mechanical, cellular, and biochemical events. The disease typically begins with focal degeneration of articular cartilage leading to eventual widespread articular cartilage degeneration. The degeneration of cartilage changes the contact stresses in the joint, causing remodeling and sclerosis of subchondral bone and osteophyte formation [3].

Mechanical factors such as patient anatomy, material properties, and loading conditions play a role in how loads are transferred across joints, greatly influencing tissue stress and strain. Anatomic abnormalities such as hip dysplasia can change the morphological structure of the hip joint. In dysplastic hips, a shallow acetabular cup reduces the contact area with the femoral head and thereby increases the cartilage contact

stresses [5-7]. The material properties of articular cartilage such as Young's Modulus and Poisson's ratio vary between normal patients, and these changes in articular cartilage stiffness have an effect on the magnitude of cartilage contact stresses [8, 9]. Obesity and high-impact activities (i.e. running) are two factors that increase the load applied across the joint, again elevating contact stresses on the articular cartilage [10, 11]. Femoroacetabular impingement is an example of a mechanical event in which repetitive collisions between the femur and acetabulum abnormally load and cause articular cartilage damage. [12, 13]. Each of these mechanical factors shows how the development of OA is a complex process with numerous variables that determine progression of the disease, making OA a difficult disease to prevent.

Post-traumatic osteoarthritis (PTOA) is a sub-set of OA initiated and accelerated by joint injuries such as dislocations, joint ligament or capsular tears, and intra-articular fractures or contusions. PTOA currently affects approximately 5.6 million patients in the United States at a cost of $3.68 billion annually [14]. Approximately 12% of lower extremity OA cases arise from joint injury corresponding to approximately 175,000 cases of PTOA in the hip each year in the U.S. [14]. Despite advancements in treatments of articular fractures, studies have shown that as many as one in four acetabular fracture patients will develop PTOA [15, 16]. The prevalence and economic cost of PTOA make it an important health care problem.

1.2 Anatomy of the Hip

The hip is a ball-in-socket joint in which the spherical femoral head articulates within the concave acetabular cup of the pelvis (Figure 1). The ball-in-socket configuration provides a highly congruent and stable articulation that allows for flexion, extension, abduction, adduction, and internal and external rotation of the femur relative to the pelvis. Adding stability to the joint is the acetabular labrum, a fibrocartilaginous lining along the rim of the acetabular cup that acts as a seal between the acetabulum and

femoral head. The labrum helps prevent joint subluxation and displacement of synovial fluid [17].

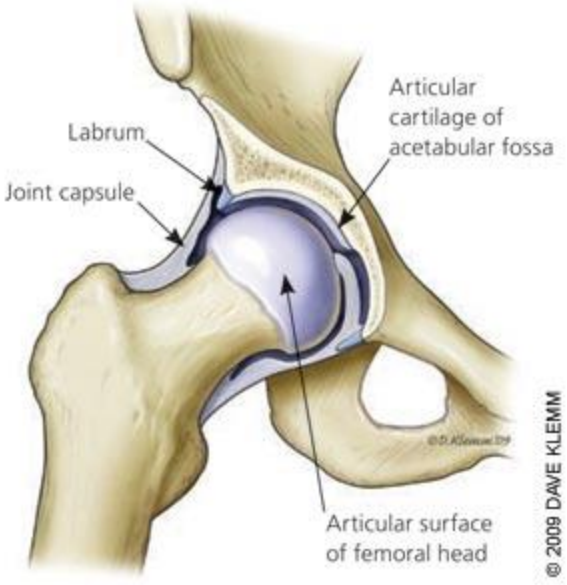

Figure 1 - Coronal view of the anatomy of the hip joint, showing the ball-and-socket configuration of the femur and pelvis. Image taken from Kuhlman et al. [18].

The range of motion of a normal hip is approximately 125 degrees of flexion, 15 degrees of extension, 45 degrees of abduction, and 30 degrees of adduction. Depending on the flexion angle, internal rotation ranges from 0 to 70 degrees and external rotation ranges from 0 to 90 degrees. There is less rotational range of motion when the hip is extended due to the surrounding soft tissues being under greater tension. [19].

Throughout a gait cycle, the resultant force across the hip changes in both magnitude and direction [20]. The maximum resultant force is dependent on the person's body weight and muscle strength, and can exceed 300% of a person's body weight at heelstrike while walking [21]. Due to the high forces exerted across the hip, it is important to have a congruent and stable anatomical joint to prevent dislocation. The acetabular articular cartilage has a horseshoe-shaped morphology that optimizes the

mechanical loading of the joint [22, 23]. This morphology makes acetabular fracture reductions very challenging by requiring precise reduction in six degrees of freedom, yet crucial in maintaining normal joint loading.

1.3 Role of Elevated Contact Stress in OA Development

Articular fractures can greatly change the geometry of the articular surface depending on the displacement of fragments and degree of comminution in the joint. Surgery is often necessary to reduce displaced articular fractures. Accurately reducing articular fractures toward an anatomical configuration is very challenging, but also critically important to patient outcomes. Residual articular surface incongruities can expose the joint to elevated contact stresses, which has been shown to increase the risk of PTOA development [24, 25].

A previous study correlated subject-specific finite element analysis- (FEA) computed contact stresses with PTOA development in 10 patients with imprecisely reduced tibial plafond fractures [26]. Five contact stress metrics were used, the first being the peak contact stress. The second metric was the area of the articular surface with a contact stress value that exceeded a damage threshold. The last three metrics used a contact stress exposure metric which multiplies the contact stress value with the time the articulating surface was exposed to that stress. One metric was a whole-joint cumulative contact stress-time dose. The fourth exposure metric was the peak cumulative contact stress-time dose and lastly, the fifth metric was the percent of area above a critical damage threshold. All damage thresholds were identified based on best-fit agreement between damage metrics and clinical outcomes. All five metrics had greater than 88% concordance with PTOA development. The area above a critical damage threshold had the best concordance with KL score (95%) and OA status (100%), defined as having a KL score ≥ 2. These findings suggest a contact stress exposure threshold exists above

which OA is likely to develop, but more work needs to be done as this study only involved 10 patients.

Using similar methods, Segal et al. conducted a study of 38 adults (age 50-79 years) currently with or at high risk for knee OA due to frequent knee symptoms, obesity, or history of knee injury or surgery [27]. Discrete element analysis computed contact stresses were correlated with cartilage morphology and bone marrow lesions using the whole-organ MRI (WORMS) scores for the femur and tibia. Results indicated that higher tibiofemoral peak and mean contact stress increased risk for cartilage degeneration, bone marrow lesions, and OA development in the knee.

Cartilage loss, bone marrow lesions, and articular fractures are not the only cause of elevated joint contact stresses. Developmental dysplasia of the hip (DDH) is a deformity of the acetabulum that creates a shallow acetabular cup, leading to joint instability and smaller contact area. This deformity can cause elevated contact stresses, putting patients at increased risk for OA development [28, 29]. All of these studies have shown that structural worsening, articular fractures, and developmental deformities can cause joint incongruity in lower extremity joints which increases contact stresses and risk of OA.

1.4 Diagnosis, Treatment, & Methods to Forestall OA

Patients with primary OA typically seek treatment with the onset of pain which begins in later stages of progression, making primary OA difficult to diagnose early. Diagnosis of primary OA in the hip is typically done using plain radiographs and one of the OA disease staging classifications, most commonly, the Kellgren-Lawrence (KL) score [30-32]. This classification is based on three indications of osteoarthritis; joint space narrowing, presence of osteophytes, and sclerosis of the bone. Scores range from 0-4, with a score of zero meaning there are no radiographic features of OA and a score of four meaning large osteophytes, joint space narrowing, and severe sclerosis of the bone.

Currently, there is no cure for OA, only preventative measures and treatments that attempt to reduce progression, relieve symptoms, or replace degenerated articular cartilage with total joint arthroplasty. Two methods pertinent to this body of work that attempt to forestall OA development are fracture reductions and pelvic osteotomies.

1.4.1 Reduction of Acetabular Fractures

Intra-articular fractures greatly increase the chance a patient will develop PTOA [15, 16]. In all but extreme cases, treatment for intra-articular fractures is reduction and fixation, a procedure in which surgeons restore a fractured fragment(s) to the correct alignment and stabilize the construct. Theoretically, this procedure will return the joint to a more anatomical state by eliminating surface incongruities and joint malalignment. While the goal is to achieve perfect anatomic reduction, it is a very difficult task to accomplish due to comminution, bone healing, and other factors. In an attempt to evaluate the quality of surgical reductions, one study defined a classification system for acetabular fracture reductions in which reductions were considered “anatomic” when there was <1 mm of maximal articular displacement, satisfactory when there was 1 to 2 mm of maximal articular displacement, imperfect when there was 2 to 3 mm of maximal articular displacement, and poor when there was >3 mm of maximal articular displacement [33]. These thresholds were based on long-term outcomes of 255 acetabular fracture patients treated within 3 weeks of injury. Anatomic reduction was achieved in 185 patients, of which 83% had excellent or good clinical results. This is in contrast to only 68% excellent or good results in the 52 satisfactory reductions, and only 50% excellent or good results in the 18 imperfect/poor reductions [33]. These results show the importance of accurate surgical reduction for preventing PTOA in the hip.

For patients with joint injuries, physicians currently have limited ability to assess risk of PTOA development. Radiographs, computed tomography (CT) scans, and magnetic resonance imaging (MRI) scans are commonly used methods for assessing joint

injury and reduction. Radiographs and CT scans are useful in evaluating displacement of fractured fragments, and MRI scans can be evaluated for articular cartilage damage. While measuring displacement of fracture fragments may provide a rough approximation of injury severity, the effect of that displacement on the articular contact stresses cannot be determined. A small stepoff in a region often exposed to high contact stress would have a greater effect on PTOA development than a large stepoff in a region exposed to lower contact stresses. By using computational modeling, patient-specific contact stress distributions could be obtained for evaluating whether an existing articular stepoff will increase joint contact stresses and the risk of PTOA development. Currently, there is an absence of a definitive relationship between PTOA development and fragment displacement or articular cartilage damage. The lack of scientific methods for guiding clinical practice leaves physicians basing their fracture reductions on observations and experience only. This has led to very little change in the outcomes of intra-articular fractures over the past 30 years, highlighting the need for improved treatment methodologies [34].

1.5 Finite Element Analysis

Computational tools have been utilized to predict contact stress in biomechanical joints to investigate the relationship between contact stress and OA and PTOA development. Numerical analysis of joint mechanics can be performed using many different approaches; however, finite element analysis (FEA) has long been the gold standard for computational modeling. This method subdivides the geometry of an object into a set of smaller 2D or 3D finite elements. One of the appealing factors of FEA is its advanced simulation capabilities including continuum modeling and contact analysis. Continuum modeling assumes a body to be made of a continuous mass rather than made of discrete particles. This assumption allows the conservation of mass, energy, and momentum laws to describe the behavior of the body. These laws are combined with

constitutive relations specific to the material in order to approximate the response of that material to physical effects such as stress, vibration, fatigue, motion, heat transfer, and fluid flow. FEA can be used to model materials with linear, non-linear, hyper-elastic, poro-elastic, rate-dependent, and many other types of mechanical behaviors [35]. Advanced multi-body and multi-scale simulations can also be performed to study complex materials such as articular cartilage [36].

Modeling articular cartilage is a complex endeavor due to its elastic, multiphasic structure which exhibits a nonlinear, time-dependent behavior [35]. Cartilage is made of proteins, mostly collagen fibers and proteoglycans, as well as an interstitial fluid composed of water and electrolytes. The porous protein structure gives the cartilage a solid phase with its own mechanical behavior, while the interstitial fluid gives the cartilage a fluid phase. The interaction between these two phases gives cartilage a biphasic response. When a dynamic load is applied, the pressure of the interstitial fluid increases which causes an increase in the stiffness of the cartilage that is time dependent on the rate at which the load is applied. Due to both the solid phase and the motion of the interstitial fluid contributing to the mechanical response of the articular cartilage, most FEA studies model articular cartilage as a poroelastic material. This biphasic approach typically involves a porous, linear elastic solid phase as well as a liquid phase [35].

To calculate contact stress using FE modeling, the bodies of interest are typically divided into hexahedral elements that are interconnected at nodes. When an element is in contact it deforms according to mathematical relationships dependent on material properties and the underlying geometry. Loading and boundary conditions can be applied to simulate different activities such as walking, running, sitting or stair ascent/descent.

Many FE models assume a simplified geometry, modeling the hip as a perfectly spherical ball and socket joint. One study compared contact stress results of subject-specific bone-cartilage interfaces to idealized spherical and rotational conchoid geometries [37]. Loading conditions simulated walking, stair-climbing, and descending

stairs. Models with spherical and conchoid geometries underestimated peak and mean contact stresses by 50% and 25%, respectively, compared to subject-specific geometry. These results demonstrate that assumptions of the joint geometry can have a significant effect on FE contact stress predictions. Therefore, the authors suggested using patient-specific geometry when studying cartilage contact mechanics.

While FEA can produce subject-specific contact stress predictions, it is a very time consuming and complex process [38]. Generating a working mesh is not a trivial task for biomedical problems due to the irregularity of the surfaces. Few meshing strategies have been designed specifically for anatomical geometries, and the quality of the computed solution is strongly dependent on the quality of mesh. Then, once a mesh is generated, the run time of a FEA model can be on the order of hours or even days. These factors preclude FEA from being a useful tool in large population studies, and highlight the need for a computationally fast and reliable contact stress assessment method.

1.6 Discrete Element Analysis

Discrete element analysis (DEA) is an alternative computational method to FEA that is based on a simplified set of equations only capable of computing contact stress. Unlike FE, all DEA algorithms treat the contact surfaces as a series of independent elastic springs which are bonded to an underlying rigid bone (Figure 2) [39]. A load or displacement is placed on one or all of the bodies, and the resultant deformation of the springs is used to iteratively solve a minimum energy principle to find contact stresses on the bodies [40].

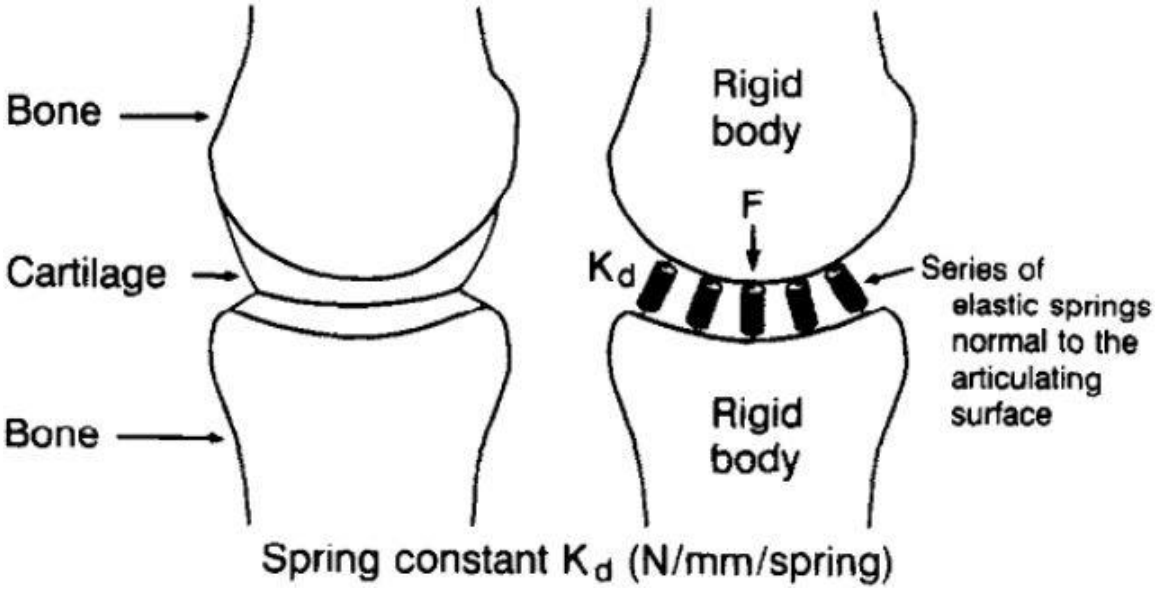

Figure 2 - Diagram depicting the fundamental basis of discrete element analysis. Each articulating surface is backed by a rigid body and has elastic springs normal to its elemental faces. When a load is applied, the spring deformation is used to calculate contact stress. Image taken from Schuind et al. [40].

Calculation of contact stresses can be done using either load or displacement control. Displacement-driven contact stress simulations are extremely sensitive to small displacement changes and require precise registration of 3D models to loaded appositions. Pose variations of ±0.1 mm can change contact stress calculations by more than 100%, requiring accuracy on the order of microns [41]. In load control, a known force is applied to the body(s) and constraints are established based on the contact with another surface. This allows two contacting surfaces to adjust into force equilibrium and achieve numerical convergence of the user-defined loading conditions. The majority of DEA studies use load control due to the simplicity of bringing the model into force equilibrium compared to the need for extremely precise registrations for displacement control.

DEA has several limitations compared to FEA in that DEA is only capable of predicting contact stress for isotropic linear elastic material. DEA is unable to model other stress or strain measures nor advanced material properties, such as poroelasticity. However, DEA also has several advantages over FEA. Most importantly, DEA allows for extremely fast computational times. A direct comparison showed DEA computation took ~7s compared to ~65 minutes for FEA for models made from the same subject [42]. Another advantage of DEA over FEA is the absence of a time consuming mesh producing procedure. When using FEA to calculate contact, there are complex relationships between the deformation of the models, external forces, boundary conditions, and regions of contact [43]. Sharp incongruities in the model often cause numerical convergence problems, requiring the mesh to be modified and further increasing the time required to develop and execute a model. The time saving features of DEA make it an attractive method for computing contact stresses in large population studies or for providing pre-operative or intra-operative contact stress predictions during articular reduction or osteotomy surgeries.

However, the speed, accuracy, and numerical stability of DEA indicate that this method could prove useful for providing pre-operative or intra-operative contact stress predictions. Such information would give surgeons biomechanical feedback before or during articular reductions and osteotomies in an effort to improve patient outcomes.

1.7 Previous Validation Studies

It is common practice to validate computational models against experimental contact stress measurements made in cadaveric preparations. For example, Anderson, et al. investigated agreement between subject-specific finite element computed contact stress and tibio-talar contact stress measured experimentally with a Tekscan pressure sensor inserted in a cadaveric ankle [44]. In two separate specimens, the discrepancy between FEA-computed and experimentally measured was 3.2% and 19.3% for mean

contact stress, 1.5% and 6.2% for maximum contact stress, and 1.7% and 14.9% for contact area. Along with agreement in these global metrics, both cases exhibited excellent point-by-point comparisons between the computed and experimentally measured contact stress distributions over the articular surface. Overall correlation coefficients were 90% and 86%.

Like FE models, DEA models have also been validated against experimental measurements, and DEA models have also been compared to FEA contact stress predictions [42, 45, 46]. The DEA algorithm used in this study is the same as the algorithm that has been previously validated in the ankle and was found to be within 4% of both experimental measurements of maximum contact stress and FEA computed maximum contact stress [46].

Although the DEA algorithm being utilized in the hip has previously been validated in the ankle [46] and the knee [45], it has yet to be validated in the hip joint which has a curvilinear ball-and-socket configuration instead of a mostly planar hinge joint like the ankle and knee. The ball-in-socket configuration causes higher shear stress compared to a mostly planar joint that is loaded normal to the surface. This raises questions of whether DEA will behave differently in the hip since the DEA model uses springs normal to the surface to calculate contact stress. If the DEA model is capable of accurately predicting contact stress in the hip there are several possible applications. One possibility is using DEA to predict changes in contact stresses following intra-articular fractures, which have been shown to significantly change the joint mechanics by altering the articular surface geometry. This requires the DEA model to not only be validated in intact hips but acetabular fractures as well.

1.8 Purpose of this Work

The purpose of this study is to experimentally validate DEA in both an intact and fractured human hip. DEA is an attractive computational method for studying a large

population of acetabular fractures due to its inherently fast computational times, ease of implementation, and ability to estimate elevated joint contact stress. In order to determine the ability of DEA to estimate contact stress in patients that have suffered intra-articular fractures, we performed a direct validation comparing experimental measurements of a malreduced fractured hip to DEA predictions. This allowed for determination of approximations regarding surface smoothing, material properties, and cartilage thickness that are acceptable and allow for the model to obtain agreement with experimental measurements. Once validated, the DEA hip model could prove to be clinically useful for making expedited contact stress predictions in patients at risk for developing PTOA after an intra-articular fracture.

CHAPTER 2: VALIDATION OF DEA IN THE HIP

2.1 Background and Motivation

Validation is an important aspect of computational modeling. A validation study determines what degree of accuracy the user can expect from the computational model, which is important when interpreting results. Every computational model requires some simplifications from physical reality, regarding boundary conditions, loading conditions, surface smoothing, and material properties. Validation against a physical experiment enhances the confidence in computational modeling assumptions by providing information about how closely the model, with its assumptions, accurately captures physical reality.

Many previous studies have focused on validation of FEA models of the hip. One such study validated a hip FE model for investigating hip stability in total hip arthroplasties [47]. A study more similar to ours performed FEA on a series of five specimen-specific hip models and compared contact stress predictions to experimentally measured contact stresses [48]. There was an average RMS error of 25% for contact stresses, and the spatial distributions of contact stresses were not visually similar between experimental measurements and FEA predictions.

There has been a single study by Abraham, et al. which used a DEA model similar to ours, and compared the stress results to results obtained from a full FEA model [48] for walking, descending stairs, and ascending stairs in the normal, intact hip [42]. That DEA hip model predicted higher maximum contact stress (9.8-13.6 MPa) and average contact stress (3.0-3.7 MPa) than the corresponding FE model (6.2-9.8 MPa and 2.0-2.5 MPa). The DEA model predicted similar contact stress distributions as FEA, specifically bi-modal contact along the lateral and posterior rims of the acetabulum. This contact stress distribution was unlike the previously reported, unicentric, equally-distributed contact stress patterns that were calculated in simplified DEA models in

which bone and cartilage geometry was obtained from 2D radiographic measures and assumed to have a spherical articulating surface [49-51]. However, the Abraham et al. DEA study only included one patient so results could be skewed from reality due to patient-to-patient variability in anatomy, weight, and cartilage thickness and structure.

Improvements have been made to DEA models by using patient-specific 3D CT data to model the cartilage-bone interfaces [52, 53], however, these studies still assumed spherical articular cartilage with uniform cartilage thickness. In reality, the cartilage thickness varies patient-to-patient as well as throughout the joint [54-56]. For our validation study, both specimen-specific and uniformly projected articular cartilage surfaces were used with cartilage thickness based on the distance between the articular surface and subchondral bone.

2.2 Validation Methods

2.2.1 Specimen Preparation

Two fresh-frozen cadaveric specimens were obtained for physical validation testing. Each specimen was comprised of a hemi-pelvis to mid-femur. The hips were intact and had no previous traumatic injuries or surgical operations. Specimen 1 was a 5’7”, 140 lbs., 71 year old male from the University of Iowa Deeded Bodies Program and Specimen 2 was a 6’0”, 175 lbs., 37 year old male from Anatomy Gifts Registry (Hanover, MD). Both specimens were carefully dissected free of all muscle, ligament, fat, and surrounding soft tissues without causing damage to articular cartilage surfaces. The labrum was removed in Specimen 1 and remained intact in Specimen 2. The specimens were kept moist with saline for the duration of the testing.

The ilium of the pelvis was cut in a transverse plane approximately 10 cm superior to the acetabulum and potted approximately 5 cm deep in polymethyl-methacrylate (PMMA). The pelvis was oriented to match previous work in which a bubble level was screwed into the acetabulum to direct the potting of the ilium [57]. This

positions the hip in approximately 15 degrees abduction and 20-30 degrees of flexion, the position of the hip during walking when maximum load occurs according to Bergmann, et al. gait data [20]. The femur was potted in a 6 cm diameter, 7 cm deep cylinder with the axis of the femoral shaft aligned to the axis of the PMMA cylinder.

2.2.2 Contact Stress Measurement

In order to experimentally quantify articular contact stress, we used a hip-specific sensor capable of measuring dynamic contact stress which was developed by Dr. Jim Rudert and manufactured by Tekscan, Inc. (Model 4402) (Figure 3) [58]. The sensor is comprised of electrically conductive strips printed on thin layers of Mylar film covering a 150˚ circumferential span. The conductive strips are arranged in 21 rings orthogonal to 52 spokes. Lines of piezoresistive ink are applied over each conductive strip in the sensing area. The sensing area can be viewed as a grid, divided into rectangles centered on the intersections of the conductive strips. Each rectangle is referred to as a sensel with sensing area comprised of 1,092 sensels total. When a pressure is applied to the sensing area, the resistance changes based on the instantaneous local compression. The sensor is connected to a computer which encodes the resistance values of each sensel as 8-bit integers (0-255) (Figure 4).

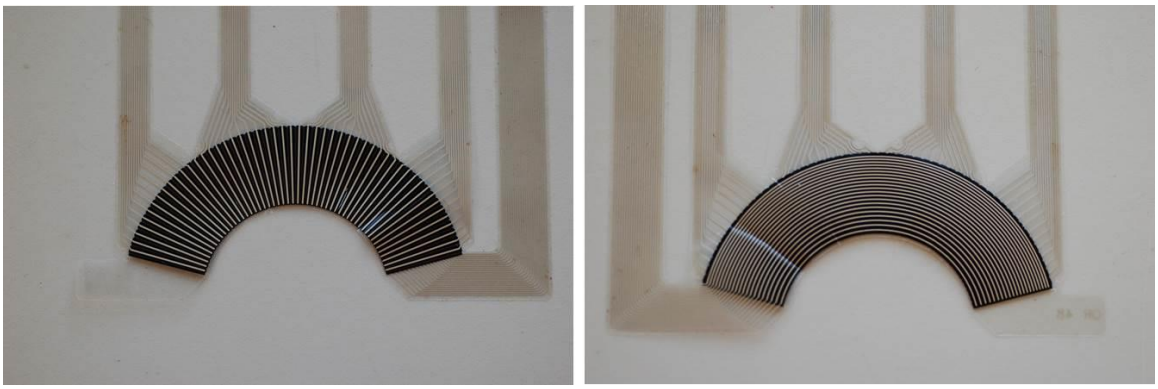

Figure 3 - The Tekscan sensor's spokes (left) and the rings on the opposite side (right). The black area which the ring and spokes cover is the active sensing area.

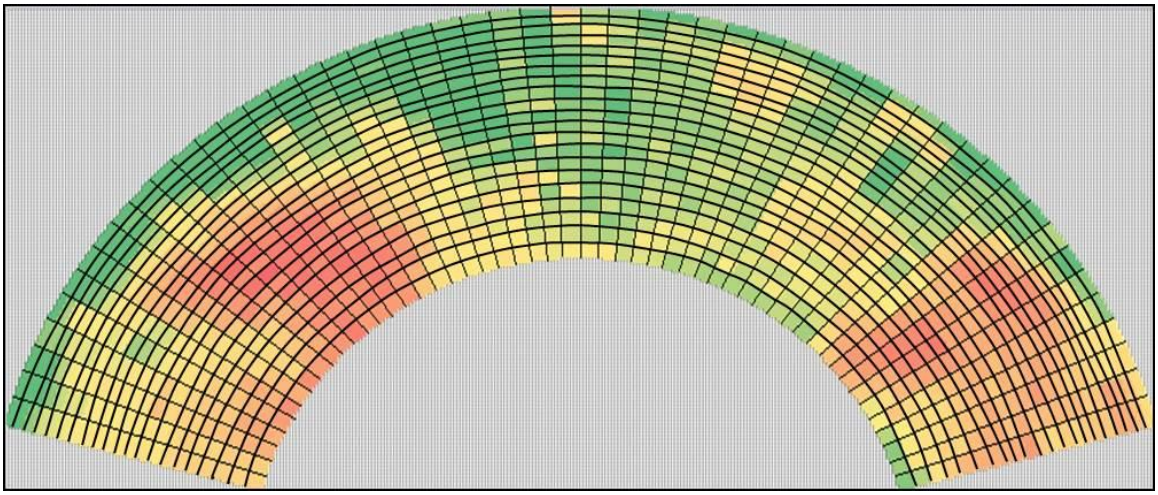

Figure 4 – Heat map representation of Tekscan data created in Excel. The black lines mark the boundaries of each rectangular sensel.

Prior to experimental testing, the sensor was calibrated by applying progressively increasing loads through an aluminum loading platen that was shaped to match a portion of the irregularly shaped sensing area and create an equal load distribution (Figure 5). A previous study noted that material of lower stiffness is more conforming to the geometric incongruities of the sensor's layers [59]. This phenomenon causes the contact area of the sensor to be greater and increases the fraction of the total load passing between conductors which are non-sensing areas. Therefore, the loading platen had a 1/32" thick 90A durometer polyurethane layer to interface with the sensor to more closely simulate the stiffness of the cartilage. The sensor was calibrated from 200N to 2,000N loads in 200N increments, and a power-law calibration curve was computed for conversion of raw Tekscan values (0-255) to stress (MPa).

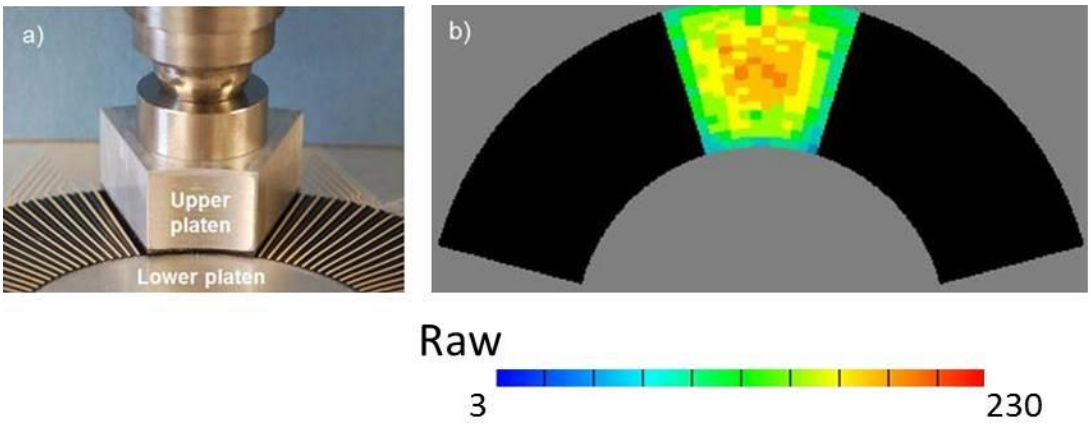

Figure 5 – Tekscan sensor calibration using the loading platen (a). The sensor's average raw output (b) was recorded at each 200N load increment and a power-law calibration curve was computed for conversion of raw pressure values (0-255) into known stress (MPa).

The sensor used in this study has an outside diameter of 48.0 mm and inside diameter of 26.6 mm, forming an area of 2,090 mm^2 with a density of 52 sensels/cm^2. The Tekscan sensor was manually positioned to maximize superior/lateral coverage of the acetabular cartilage, which covered the majority of the loaded area during walking. This meant that the medial-most cartilage was not covered by the sensor, and therefore not measured during testing. During positioning, the locations of the primary contact patches were investigated, and if pressures were located at the edge of the sensor, the load was removed and the sensor was repositioned to ensure that a significant portion of the load was not off the edge of the sensor.

Over the course of several repeated data acquisitions, sensor degradation was observed. This caused the sensor to report lower contact stresses under identical pressure. To account for sensor degradation, the sensor was recalibrated after testing and equal weighting was applied to the pre-test and post-test calibration curves when converting raw Tekscan values into contact stress. A sensor was used for a maximum of two tests to

help limit the degradation effect. All calibration curves had an R^2 value of greater than 0.999.

2.2.3 Hip Joint Loading

The loading applied to the DEA algorithm was based on the HIP 98 data from Bergmann, et al [20]. This data set was formed using instrumented hip prosthesis inserted into four subjects that underwent extensive gait analysis in a variety of activities including walking, standing, stair ascent/descent, and sitting. During the gait analysis, measurements were recorded for limb positions, rotations, forces, and moments. Before using the Bergmann data to implement the full walking gait cycle into the DEA algorithm, we chose to validate the DEA algorithm at heel-strike, mid-stance, and toe-off to represent the full gait cycle. For walking gait, Bergmann's gait analysis obtained measurements at 201 discrete time intervals over 1.103 seconds. This data was discretized into 13 evenly distributed steps. Of these 13 steps, the heel-strike position was determined by the step with the greatest amount of flexion, mid-stance position was determined by the step with 0˚ flexion, and toe-off position was determined by the step with the greatest amount of extension, corresponding to steps 4, 8, and 11, respectively. The cadaveric specimen was oriented in heel-strike, mid-stance, and toe-off according to the experimentally measured rotations in the Bergmann coordinate system at these discrete steps.

In the Bergmann pelvic coordinate system (Figure 6), the X-axis is defined by a line connecting the centers of the two femoral heads. In the left hip, positive X points in the medial direction. The Z-axis is the vertical axis. It is perpendicular to the X-axis, pointing superior through the center of the L5-S1 vertebral body in a lateral view. The Y-axis is perpendicular to X and Z and points in the ventral direction. The origin is located at the center of the left femoral head.

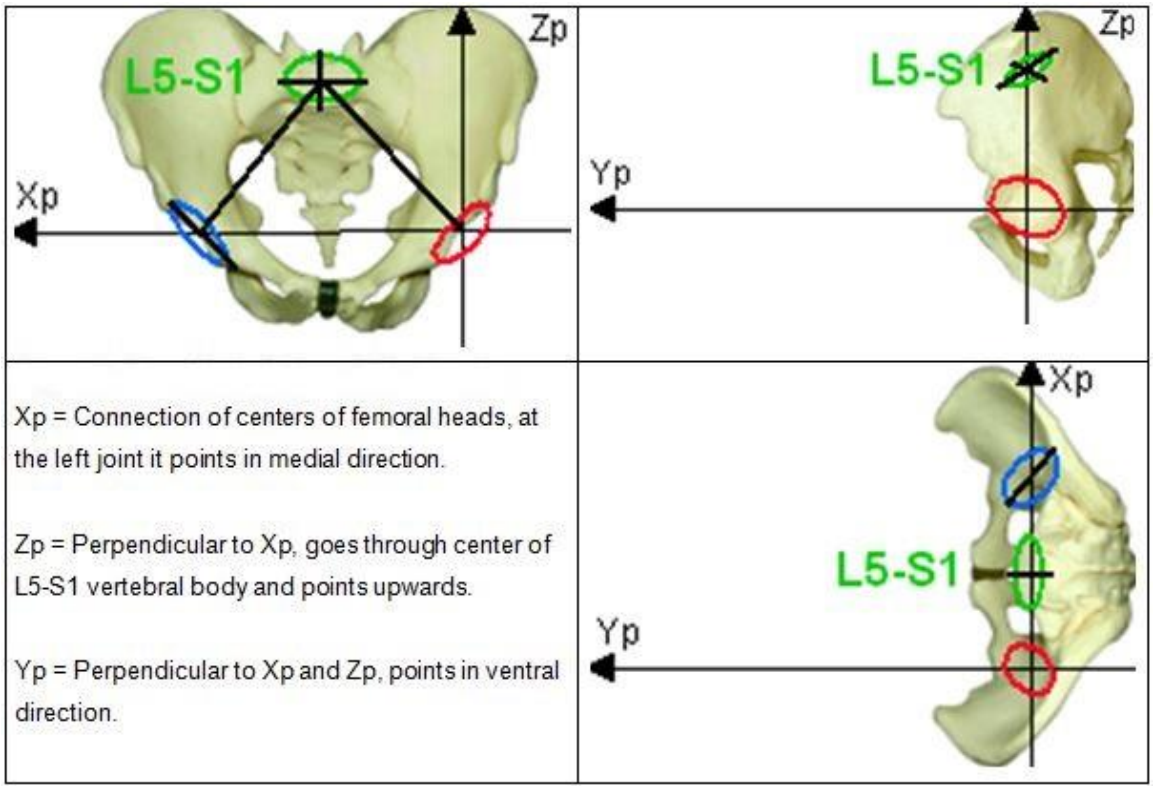

Figure 6 – Definitions of the Bergmann pelvic coordinate system [20].

In the femoral coordinate system (Figure 7), the X-axis is defined by a line through the center of both condyles. The Z-axis is coincident with a vertical line through the center of the femoral shaft. The Y-axis is perpendicular to X and Z and points in the ventral direction. The origin is at the center of the femoral head.

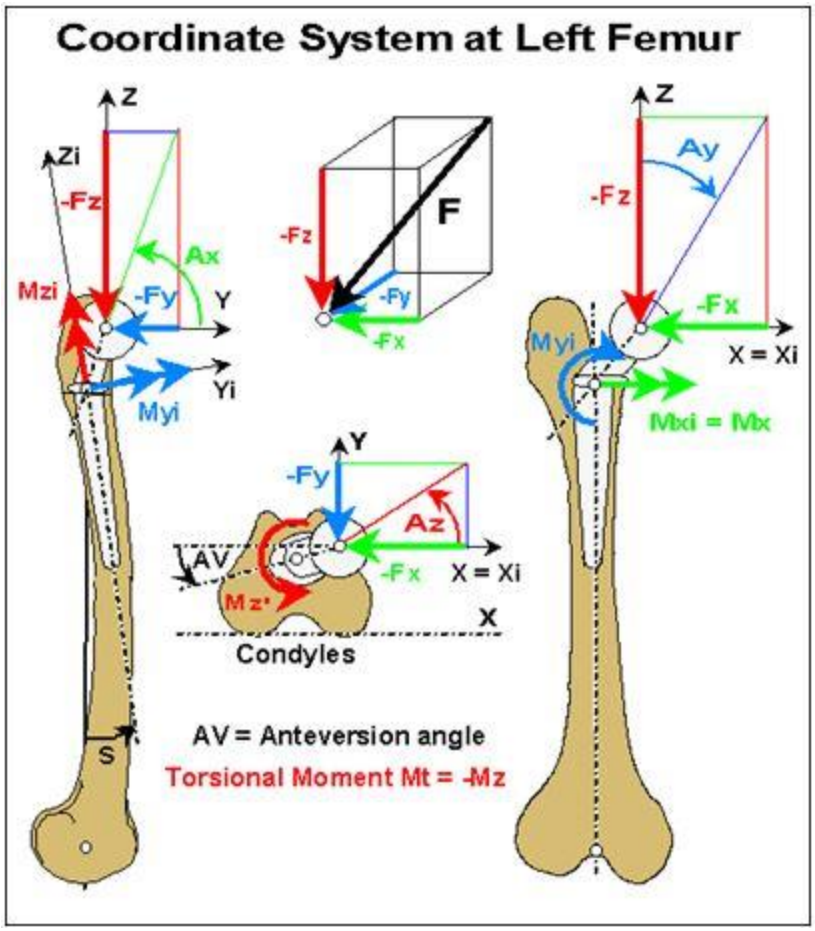

Figure 7 – Definition of the Bergmann femoral coordinate system [20].

Prior to testing, each specimen was positioned in the testing fixture in an approximate heel-strike position, and a CT scan was obtained to establish baseline position. Since the Bergmann coordinate system is defined using physical landmarks that are no longer present on the potted specimens, a full anatomical model of the Virtual Human hip was aligned to the Bergmann coordinate system and positioned in heel-strike using Geomagic Studio (Geomagic, Inc., Morrisville, NC.), a reverse engineering software with advanced surface modeling functions. The baseline scan of each specimen was registered to the Bergmann-oriented model using a least squares method. The transformation matrix necessary to move the cadaveric hip from the baseline position to

the Bergmann heel-strike position was recorded. These rotations were applied to the experimental fixture to position the cadaveric specimen in a heel-strike position. This process was repeated to move the cadaver from heel-strike to mid-stance and from mid-stance to toe-off.

A custom fixture for loading the hip specimens was designed to be compatible with the MTS Bionix 858 loading machine. The pelvic PMMA block was rigidly attached to an aluminum plate free to translate in the X and Y directions. The femoral PMMA cylinder was rigidly attached to the material testing machine in a manner that inverted the hip. A compound sine plate was used to control the flexion/extension angle about the Y-axis and the abduction/adduction angle about the X-axis (Figure 8). The MTS machine rotates the femoral PMMA cylinder to control internal/external rotation. Specimen 1 was positioned to simulate heel-strike during normal walking gait in both the intact and malreduced fractured state [20]. Specimen 2 was positioned to simulate heel-strike, mid-stance, and toe-off during normal walking gait in the intact state. During testing, a 1,000N static load, which represents approximately 225 lbs. of bodyweight, was placed across the hip joint in the direction of the femoral PMMA cylinder axis. After the load was applied for a few seconds, data was recorded at 3 discrete time intervals, each one second apart. No significant variation was observed between the three instances of data recording, ensuring no dynamic loading was occurring.

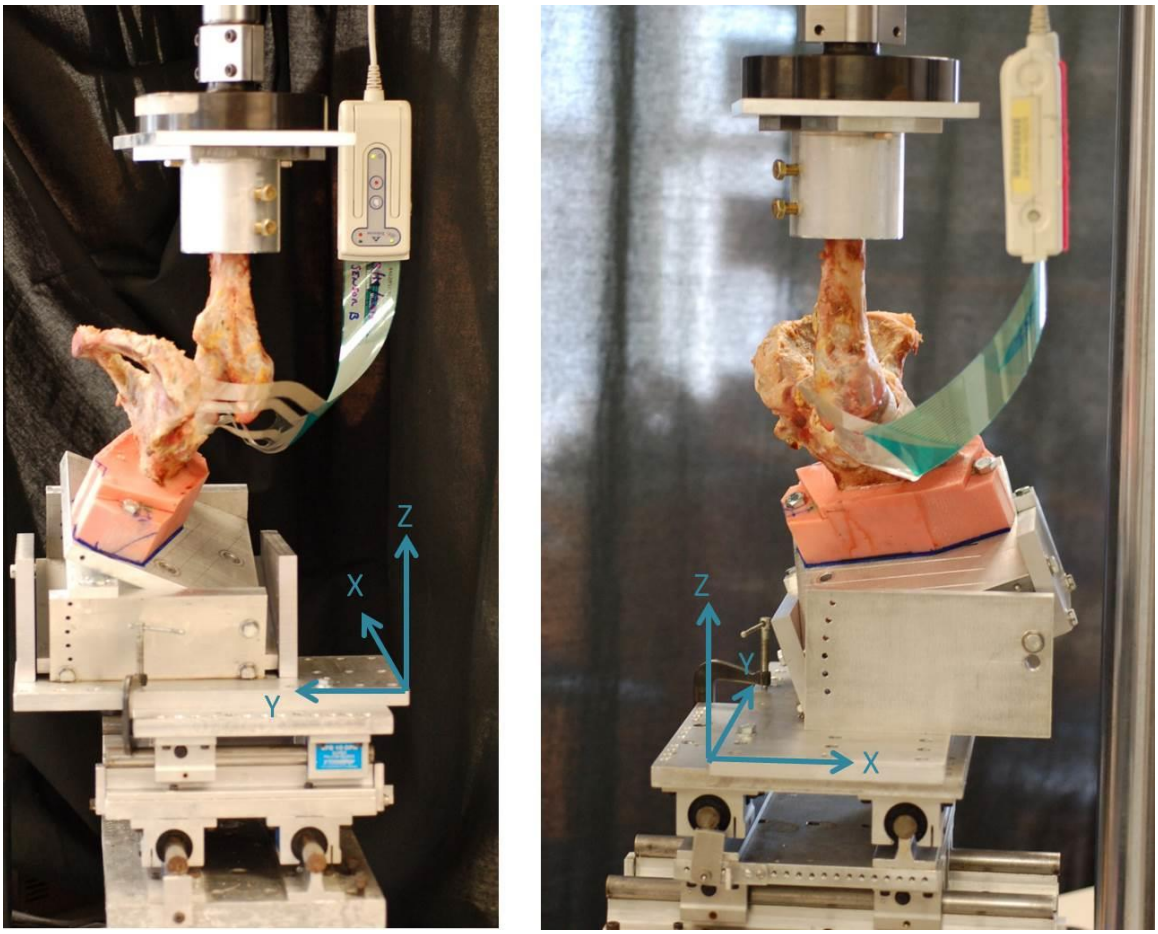

Figure 8 - Experimental setup using a custom fixture to apply a compressive force across the hip joint. The pelvis was rigidly attached to a plate that was free to translate in the X-Y directions. The femoral shaft was rigidly attached to the material testing machine in the z-direction.

After data acquisition, the specimen was locked into the loaded configuration by placing a rigid rod between the top and bottom plates of the loading fixture (Figure 9). The rod maintained the load across the hip joint after the specimen was removed from the materials testing machine. This load keeps the femur, pelvis, and Tekscan sensor in the same loaded apposition during subsequent CT imaging and prevents the Tekscan sensor from moving relative to the acetabular cartilage. Provided that no movement occurs between the sensor and the bones, there is no need for additional registration between the Tekscan sensor and the acetabular cartilage of interest.

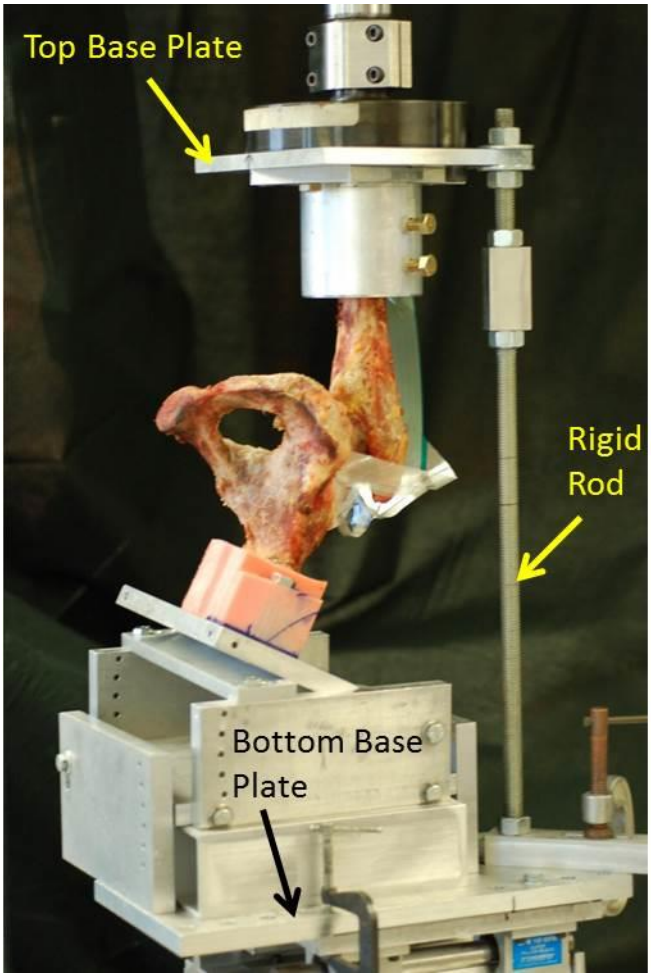

Figure 9 - Testing fixture and rigid rod used to lock the hip in the loaded apposition during imaging.

2.2.4 DEA Model Creation

After experimental testing and data acquisition, the first step to creating the corresponding DEA model was segmenting the femur and the pelvis from the CT scans of the bones in their loaded configuration. Segmentation was performed using a semi-automated program developed in MATLAB (Mathworks, Natick, MA). The program uses a custom-developed marker-based watershed algorithm [60]. The algorithm effectively identifies the edges of cortical bone, but sometimes omits portions of the cancellous bone. ITK-Snap is used to overlay the segmentations on the CT scan, and any

bone regions left unsegmented are manually edited (Figure 10). Each complete bone segmentation is converted into a polygonal surface by exporting a .stl file. The polygonal surfaces are then imported into Geomagic Studio.

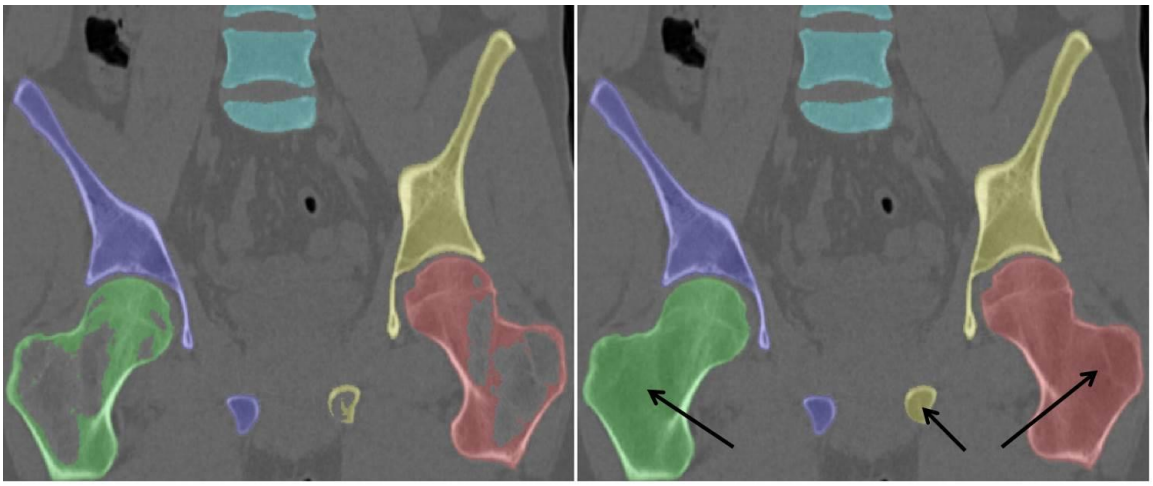

Figure 10 - Visualization of the femur, pelvis, and spine after automated watershed segmentation (Left). The algorithm labels each individual bone region, indicated by the different colors overlaid on the CT scan. After automated segmentation, minimal user input is required to fill in any previously unsegmented regions (indicated by the arrows) (Right).

Prior to physical testing, the hip specimen had been imaged using a dual echo steady-state (DESS) MRI sequence to obtain specimen-specific articular cartilage information. During MR imaging, the femoral head was slightly distracted from the acetabulum to allow for distinguishing a boundary between the articulating surfaces of acetabular and femoral cartilage. The articulating edges of the cartilage surfaces were manually traced using OsiriX software and a WACOM tablet (Figure 11). The tracing generates points (Figure 11) which are exported in a comma-separated value (.csv) file, which was then converted into a polygon file format (.ply). The .ply file contained a point cloud comprised of each point generated by the manual tracing. Geomagic Studio software was again used to create triangulated surfaces defining the articular cartilage surfaces, using the point cloud data as vertices for each triangular facet in the surface.

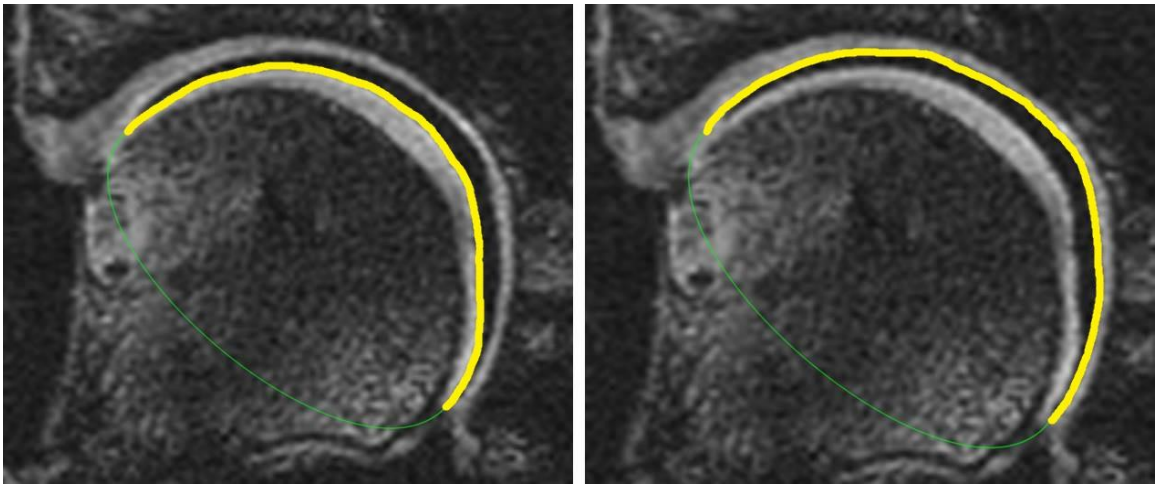

Figure 11 - MRI image slices of the manual segmentation (yellow line) of the acetabular cartilage (left) and femoral cartilage (right) which generated a point cloud. The green line is a feature of the tracing function in OsiriX software, however, because there were no points on that line, its presence has no effect on the segmentation.

The Tekscan sensor was visible in CT scan obtained after loading, and it was also segmented by manual tracing on a Wacom tablet using OsiriX software (Figure 12). A 3D surface model of the Tekscan sensor was generated in Geomagic Studio using the same method as for the cartilage surfaces.

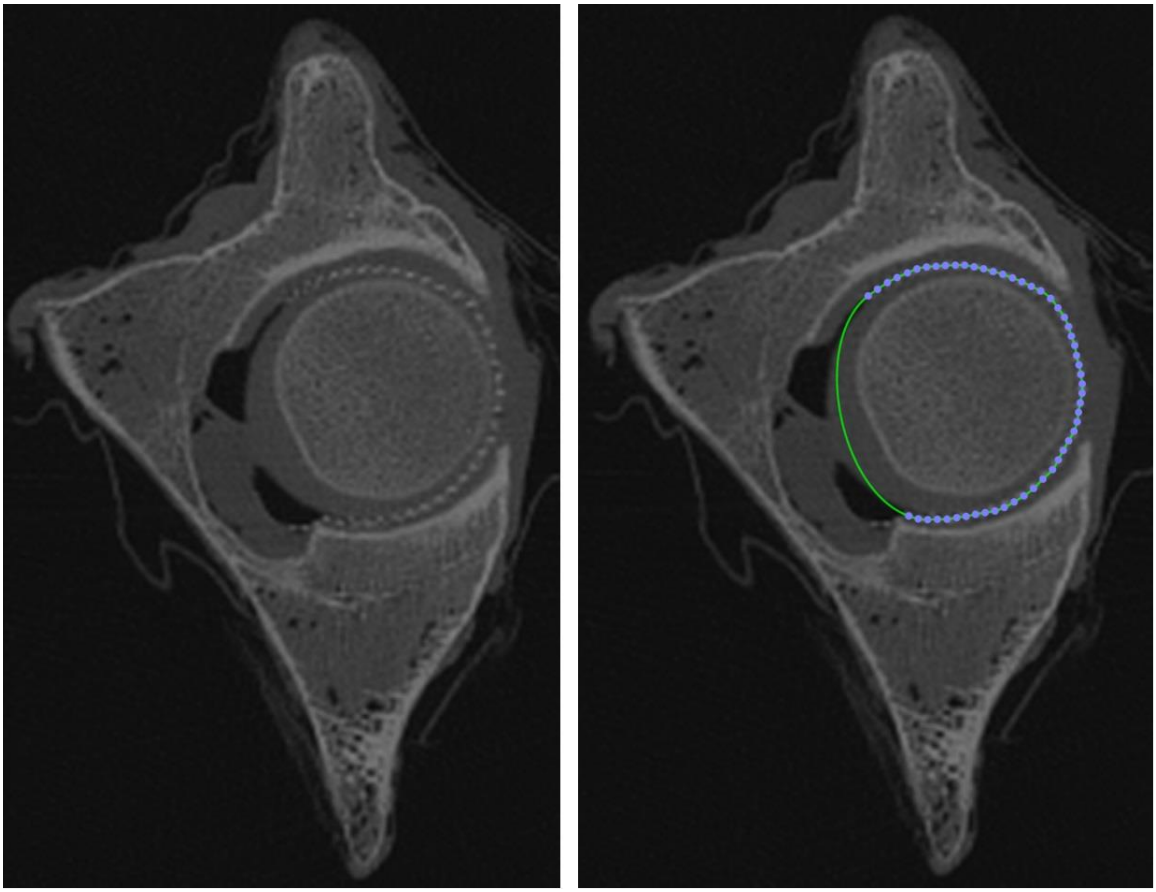

Figure 12 – CT image slice of the Tekscan sensor in the joint space (left) which was manually traced in OsiriX (right) to generate a 3D surface model of the Tekscan sensor from the point cloud comprised of the purple dots. The green line is a feature of the tracing function in OsiriX software, however, because there were no points on that line, its presence has no effect on the segmentation.

2.2.5 Cartilage Smoothing

Segmenting surfaces from CT or MRI images creates a stair-step artifact based on the voxel resolution. These surface incongruities can alter the results of computational models. In order to accurately model the smooth articular cartilage surface in the model, a surface smoothing algorithm was developed in MATLAB based on a previous cartilage smoothing method that iteratively adjusts the surface towards sphericity based on the position of neighboring facets [61].

The first step in the smoothing algorithm is to fit a sphere to the original segmentation of the articular surface and find the Euclidean distance of each cartilage surface vertex from the center of that sphere. Next, an iterative process moves each vertex by the difference between the vertex's radius and the average radius of the connected neighbors within a user-specified distance (Equation 1). The user can also specify a maximum radial change per iteration. The new coordinate of each vertex is calculated using Equation 2.

$$r_i = \frac{\sum_{j=1}^{j \le n} d_{s[j]}}{n}$$

Equation 1 – Calculates the new radius of vertex *i*, where
n: number of connected neighbors of *i*
s[j]: vertex number of connected neighbor
$d_{s[j]}$: distance of node s[j] from the center

$$x[j] = c[j] + v[j] \cdot r_i$$

Equation 2 – Calculates the new coordinate of vertex *i*, where
j: equals 1, 2, or 3 representing the x, y and z coordinates, respectively
x[j]: coordinate of vertex *i*
c[j]: center of the sphere fit to the articular surface
v[j]: direction vector between vertex *i* and the center *c*

For this study, articular surfaces were smoothed using a 0.05 mm maximum radial change for 5 iterations and a 2mm connected neighbor threshold. These constraints were empirically determined and allow a total maximum radial change of 0.25mm, approximately half the distance of a voxel. As the number of iterations and/or max step is increased, the articular cartilage approaches a spherical surface with thickness that varies according to the distance between that smoothed surface and the underlying subchondral bone (Figure 13).

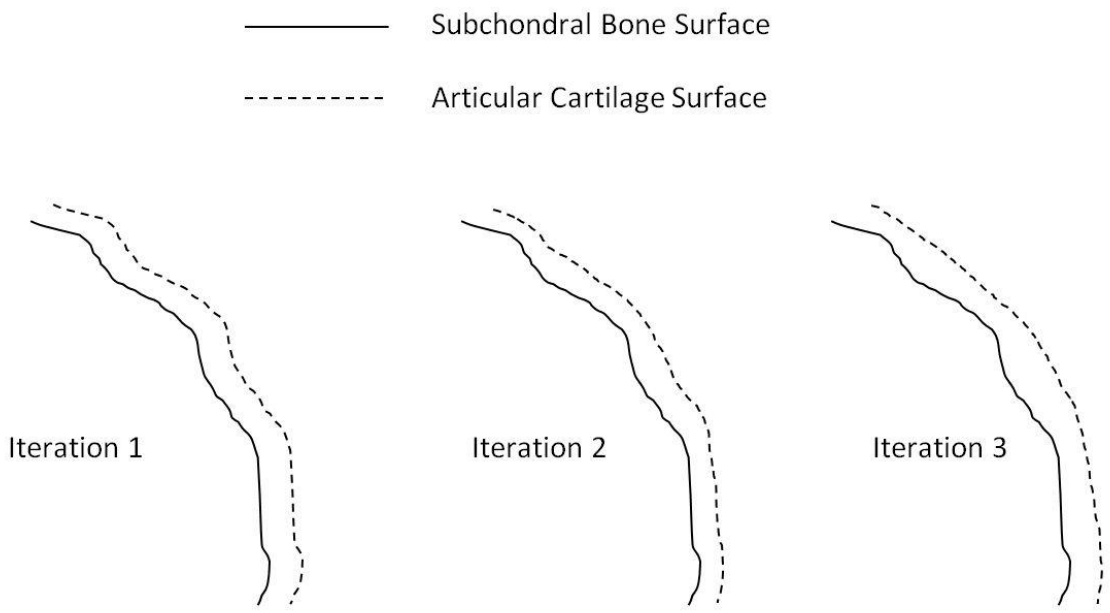

Figure 13 - Cartoon representation of the smoothing algorithm. As the number of iterations increases, the articular cartilage surface becomes more spherical with varying cartilage thickness dependent on the subchondral bone.

In future applications of DEA, MRI data may not be readily available for segmenting patient-specific articular cartilage surfaces. Therefore, it may be required that the articular cartilage be approximated based on CT images. One possible method is to uniformly project the subchondral bone segmented from the CT images a set distance. After projection, the above smoothing algorithm can be used to smooth the surface from residual incongruities of the subchondral bone surface. This method of cartilage approximation based on bony geometry is fast and easily implemented but relies on two major assumptions. The first assumption is the magnitude of the distance which the cartilage is projected from the subchondral bone. Secondly, this method assumes the cartilage surface is nearly spherical. In order to validate this cartilage approximation method, experimentally measured contact stresses were compared to DEA computed contact stresses based on a cartilage surface that was manually segmented using a MRI

and a cartilage surface that was approximated using the method described above. Identical loading conditions and material properties were used for both DEA simulations.

2.2.6 Model Alignment

The DEA model consists of the femoral head cartilage, acetabular cartilage, femur, and pelvis. Articular cartilage surfaces were segmented from MRI scans, whereas bony surfaces were segmented from CT scans, thus creating the need for registration of data between the two image modalities. To register the different data sets, the pelvis and femur bone surfaces were manually segmented from the MRI scans and registered to the pelvis and femur surfaces that resulted from segmentation of the CT scans in the experimental testing apposition. Alignment was performed with Geomagic Studio software using an iterative least squares method where the sums of squares of distances between the two sets of bones are minimized over all the rigid motions that could realign the two objects (Figure 14). The average error was less than 0.3 mm for each case which is less than the 0.5 mm voxel size of the CT scans. The transformation matrix needed to achieve bone alignment was also applied to the articular cartilage surfaces that were obtained from the MRI scan, thus orienting the cartilage surfaces in the experimental testing apposition. Because the Tekscan sensor was segmented from the CT scan, it was automatically oriented in the correct apposition.

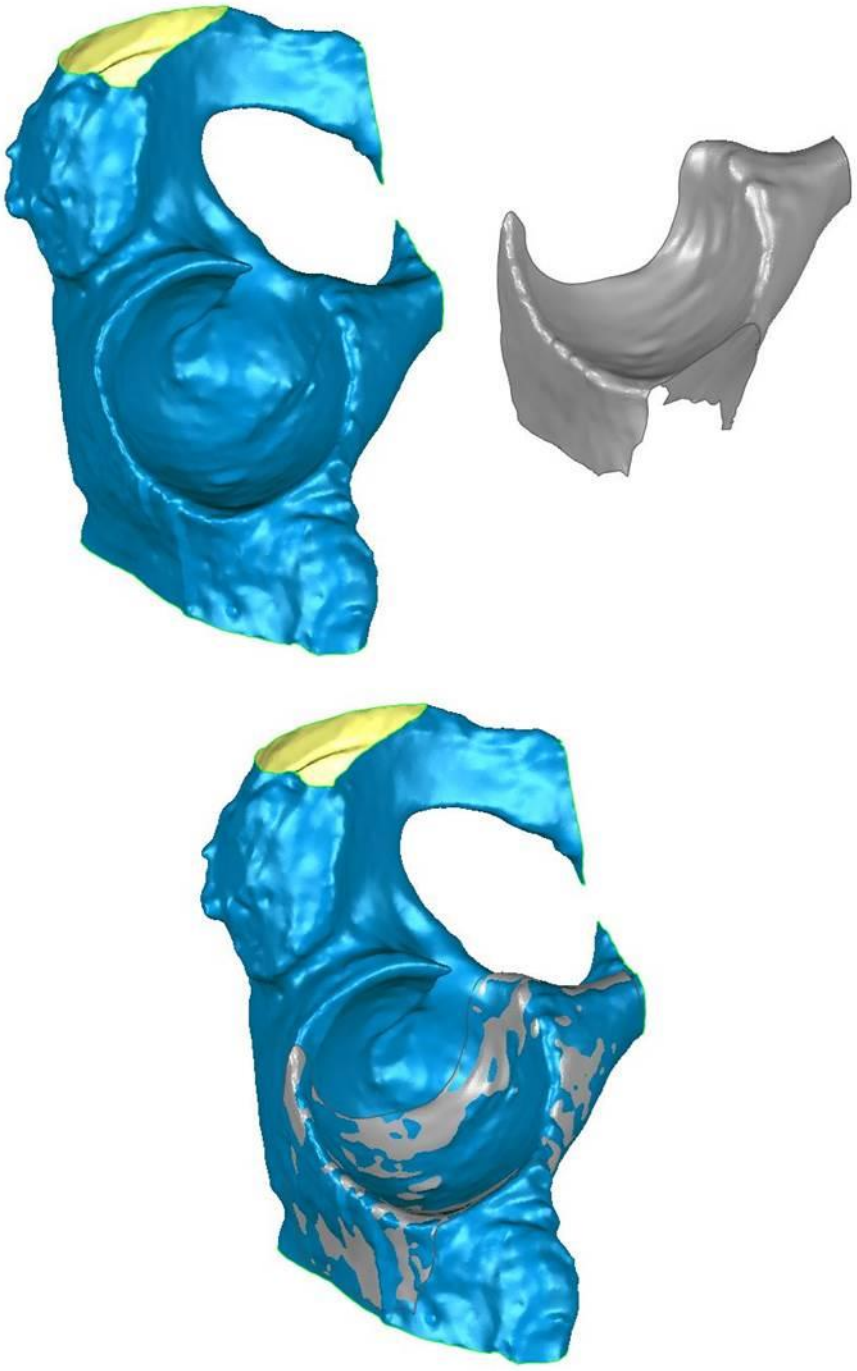

Figure 14 – Registration of the pelvic bone segmented from the MRI scan (grey) to the pelvic bone segmented from the CT scan (blue) using a least-squares method. The overlap between the two bone surfaces can be seen in the bottom image.

2.2.7 Tekscan Data Processing

In order to map the 2D Tekscan data onto the 3D Tekscan surface, the segmented surface was divided into 21 rings and 52 spokes to correspond to the physical layout of the sensor. The spacing between the Tekscan sensor's rings is inversely proportional to the distance from the center point of the rings and spokes (Figure 15). This relationship is meant to maintain an equal contact area for each sensel. When dividing the Tekscan surface model into 21 rings, the spacing was proportional to the Tekscan sensor's ring radii.

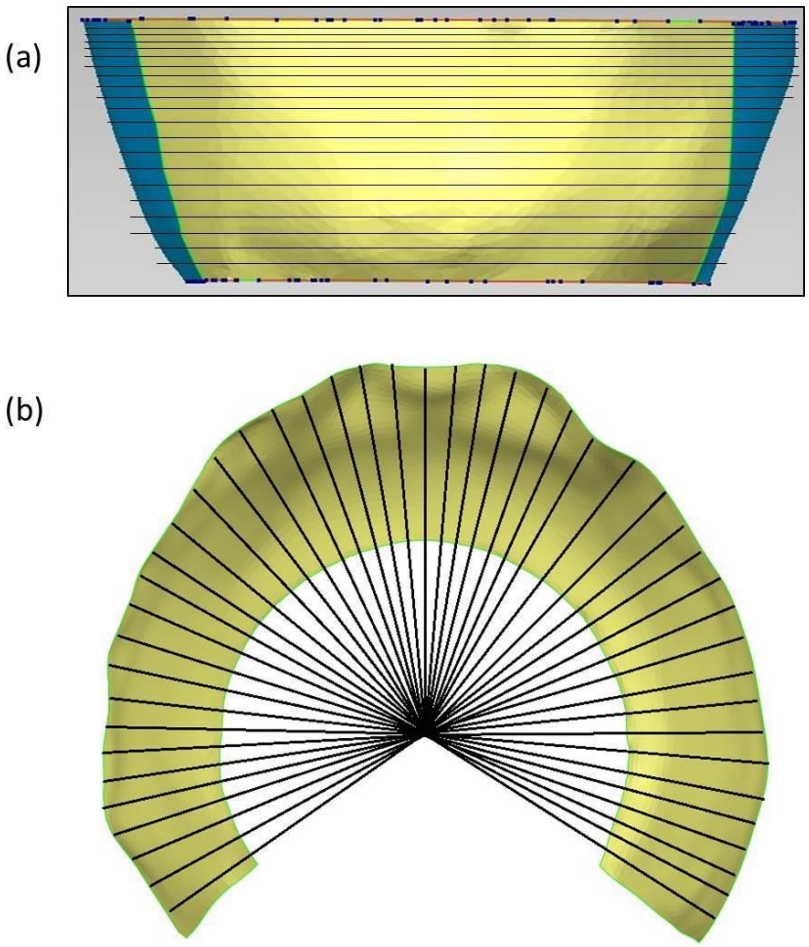

Figure 15 - (a) Orthogonal views of the 3D segmented Tekscan sensor being divided into 21 rings and (b) divided into 52 spokes.

The Tekscan sensor covers a 150˚ circumferential span when laying on a flat surface. However, when the Tekscan sensor is positioned to cover the acetabular cartilage, the sensor is deformed to cover a spherical geometry, changing the circumferential span. To divide the 3D Tekscan sensor surface into 52 evenly spaced spokes, a circle is fit to the bottom edge of the Tekscan sensor's surface. Using the center of the circle and the two corners of the sensor's surface, an angle θ is found which is divided by 52 to obtain the angle between each dividing spoke. Every face on the Tekscan sensor's surface is assigned a raw pressure value based on the row and spoke that the face's centroid is located on. The raw value is converted into contact stress (MPa) using the calibration curve obtained during sensor calibration.

Once the contact stress values are mapped to the 3D Tekscan sensor surface, the stress values are then projected onto the acetabular cartilage using a ray casting algorithm. This allows for direct comparison of the Tekscan-measured contact stress to DEA-predicted contact stress. With this algorithm, rays, or lines of infinite length perpendicular to the triangular face, are projected normal to each face on the acetabular cartilage. If a ray from the acetabular cartilage intersects a face on the surface of the Tekscan sensor, the stress value measured at that particular face of the Tekscan sensor is copied to that location on the acetabular cartilage (Figure 16). With the experimentally measured contact stress values plotted onto the acetabular cartilage, direct comparison with DEA-computed contact stresses can be made. Correlation between Tekscan and DEA was calculated using MATLAB's built-in corr2 function.

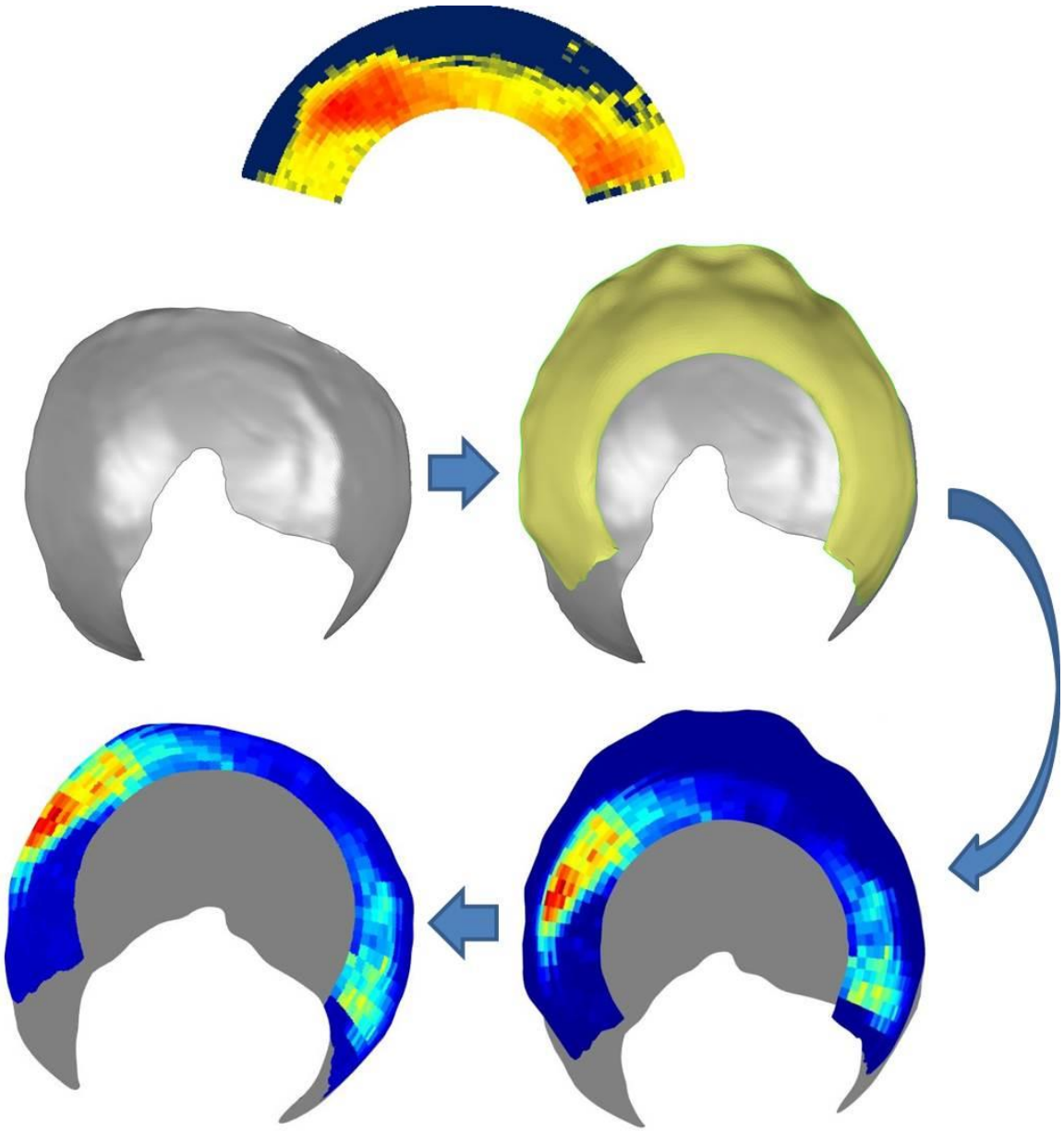

Figure 16 - Depiction of Tekscan values (Top) being mapped onto the acetabular cartilage. (Middle Left) 3D surface of the acetabular cartilage. (Middle Right) 3D surface of the Tekscan sensor (yellow) and the acetabular cartilage (gray). (Bottom Right) Tekscan data plotted onto the 3D surface of the Tekscan sensor. (Bottom Left) Result of the ray casting algorithm mapping the Tekscan values onto the acetabular cartilage. Acetabular cartilage that was uncovered by the Tekscan sensor during testing is colored grey.

2.2.8 DEA Algorithm

The DEA methodology used in this study was developed in-house by Andrew Kern [62]. The DEA model is comprised of rigid contact surfaces with a system of linear springs determining contact. The algorithm requires five inputs; (1) triangulated articular cartilage surfaces, (2) desired loads & moments, (3) cartilage thickness values for each triangular facet, (4) material properties (Young's modulus and Poisson's ratio), and (5) termination constraints for the model. The simulation consists of a series of iterative static solutions. Each iteration begins by efficiently finding the contacting faces on the opposing surfaces with a ray casting algorithm that casts a ray normal to each face until the ray intersects the opposing surface (Figure 17). If the ray does not intersect the opposing surface, the face is not considered to be in contact. A linear spring is created from the centroid of the face which the ray originated from, to the intersection of the ray with the opposing surface.

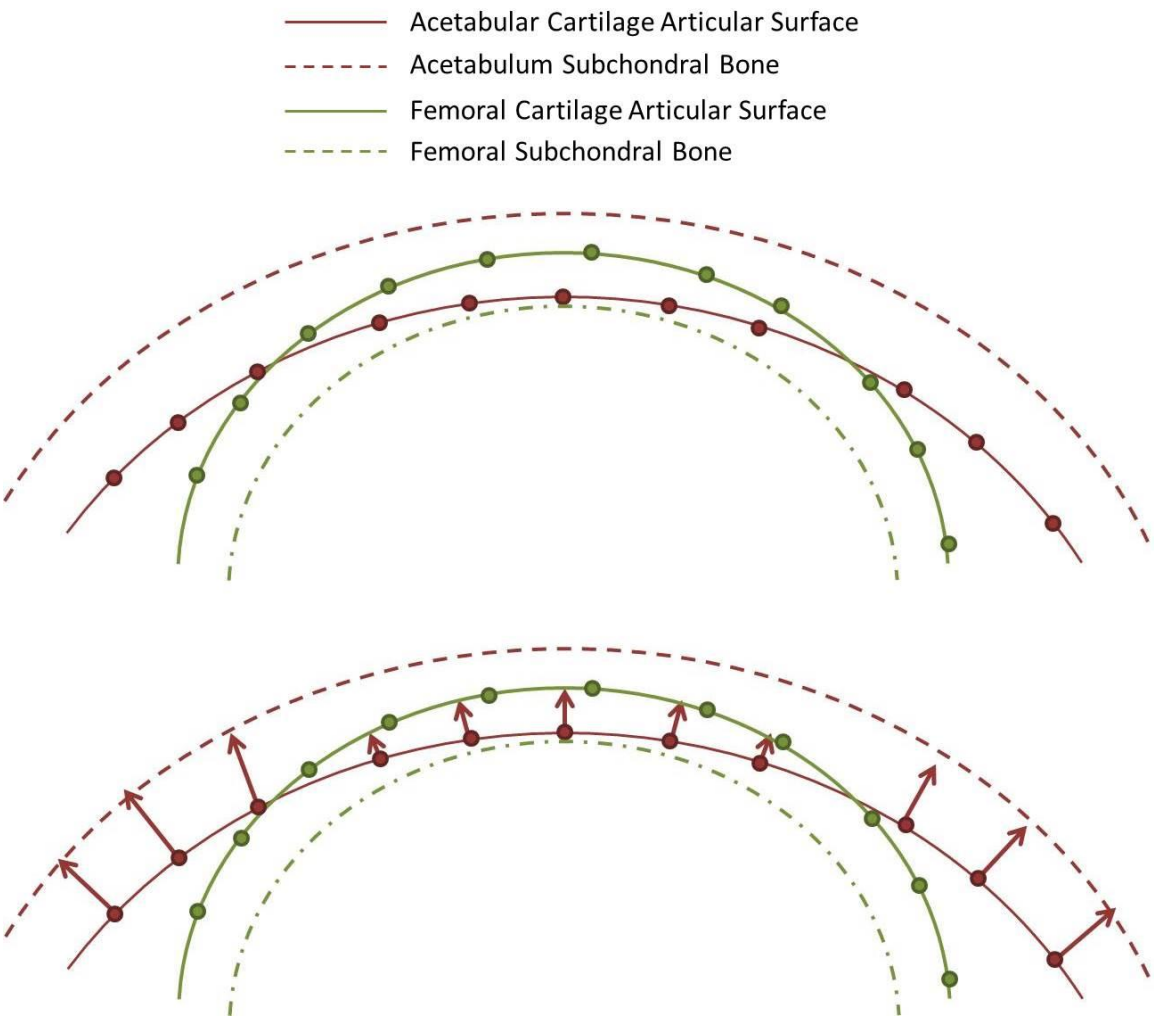

Figure 17 – (Top) Depiction of the spring system creation using the articular acetabular cartilage surface (solid red), articular femoral cartilage surface (solid green) and their respective subchondral bone surfaces (dashed). (Bottom) Rays are casted normal from the centroid of each face on the articular cartilage surface (represented by the circles) towards the subchondral bone. If a ray comes into contact with the other articular cartilage surface, the face is considered in contact. If a ray does not come into contact with the other surface, the face is not considered in contact. After determining the faces in contact, a spring is created normal to the face. The spring deformation is equal to the length of the casted ray.

After the spring system is created, contact stresses are calculated using the equation below, a force-displacement spring model, which calculates the contact stress

(p) based on spring deformation (d), cartilage thickness (h), Young's modulus (E), and Poisson's ratio (v).

$$p = \frac{(1-v)E}{(1+v)(1-2v)}\frac{d}{h}$$

Equation 3 – Contact stress calculation performed during each iteration of the DEA load balancing routine.

The amount of overclosure between the opposing surfaces determines the spring deformation used in the spring model equation to calculate contact stress. Once the contact stresses are calculated the model undergoes an iterative load control algorithm. In this load control algorithm, contact pressure and the associated area are summed to find a total contact force acting over the entire surface. Next, a Newton's method solver compares the current forces to the user defined forces. If the forces do not meet equilibrium tolerances, then a rigid affine transformation is applied to move the surfaces toward equilibrium based on the Newton's method solver's approximation of the root of the difference between user input forces and current forces. The DEA model converges when the forces engendered by the calculated contact stresses are within 1/1,000th of the applied forces.

For validation testing, the load applied to the DEA model was 1,000N, equivalent to the load applied during physical testing. The direction of the physical testing load is along the axis of the PMMA cylinder surrounding the femoral shaft. In order to apply the load along the same direction in the DEA model, the PMMA cylinder is segmented and a line is created along the axis of the cylindrical region in Geomagic Software. The load applied in the DEA model is in the direction of this axis. No moments are applied on the model. Equivalent boundary conditions are applied to the model as the physical testing

setup, where the pelvis is free to translate in the X and Y directions and constrained from all rotations.

A cartilage thickness value is assigned to each face defining the cartilage surface based on the distance between the articular cartilage surface and the subchondral bone. The distance is calculated using a nearest neighbor algorithm which iterates through every face on the articular cartilage surface and finds the face on the subchondral bone that is the shortest Euclidean distance away. This method gives the articular cartilage a subject-specific non-uniform thickness, as studies have shown cartilage to have varying thickness across different regions [54-56, 63].

Articular cartilage exhibits a poroelastic behavior that is dependent upon the rate at which it is loaded. Because DEA is unable to model poroelastic materials, cartilage was assumed to be linear elastic with a Young's modulus of 8 MPa and Poisson's ratio of 0.42 based on values reported in literature for a 30-50ms loading rate which is a physiological loading rate for walking [8, 9, 64]. A previous study noted the use of subject and region-specific material coefficients did not increase the accuracy of FEA contact stress predictions compared to experimental contact stress measurements [48]. This suggests the use of average material coefficients is sufficient for predictions of contact stress and contact area in the hip joint during walking.

2.2.9 Fracture Creation & Fixation

For DEA to be used to predict contact stresses following intra-articular fractures, the DEA algorithm must be validated in a fractured hip. After experimental testing was performed in the intact state, a posterior wall fracture was created by an orthopaedic surgeon (Dr. Michael Willey) using a previously described method [65]. The fracture began 40 degrees posterior to the acetabular vertex and extended along the acetabular rim to end 90 degrees posterior to the vertex. The fracture extended medially approximately 50% of the articular width. The fracture was created using an oscillating bone saw and

osteotome. The fragment was reduced with an intentional 2-mm step-off, a distance previously shown to be statistically significant for increasing peak contact stress [66]. Fixation of the fragment was done using a buttress plate and six screws. Two interfragmentary screws were inserted through the posterior portion of the fragment and outside the buttress plate. The other four screws were inserted through the buttress plate, two proximal to the fragment and two distal to the fragment (Figure 18).

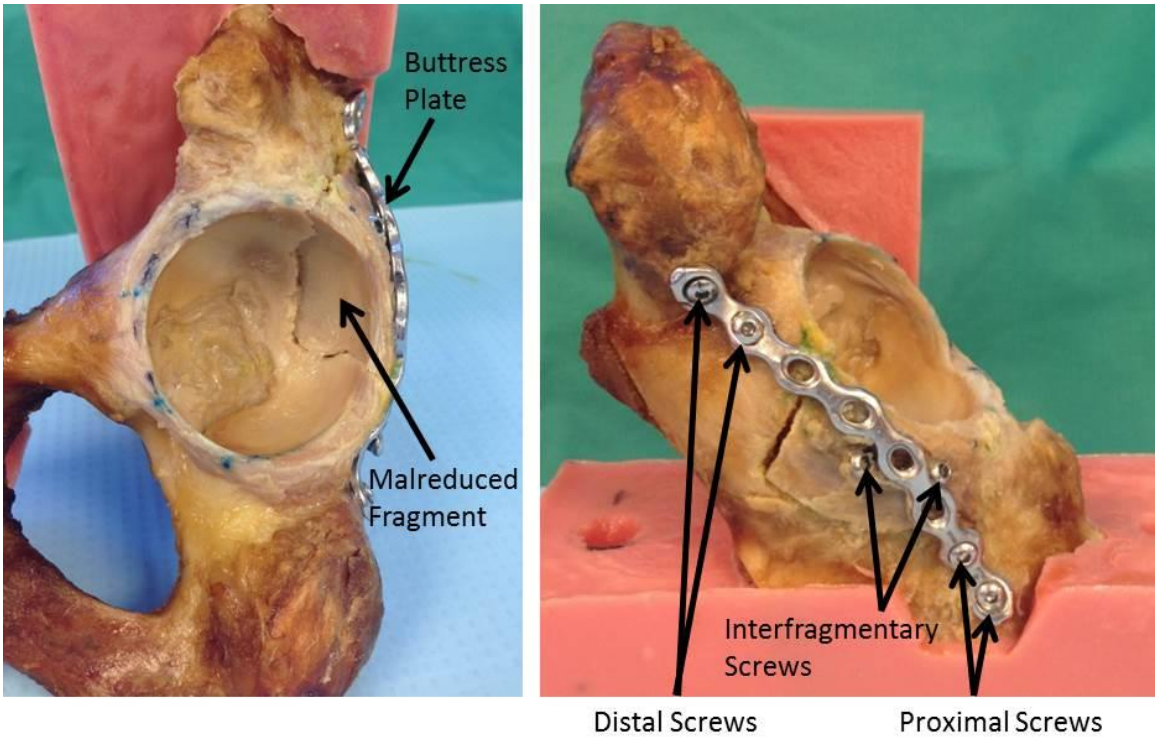

Figure 18 - Posterior wall fracture and 2-mm step-off malreduction created in Specimen #1.

2.3 Validation Results

Specimen #1 had a mean acetabular cartilage thickness value of 1.34 mm and mean femoral cartilage thickness value of 0.96 mm. Specimen #2 had a mean acetabular cartilage thickness of 1.67 mm and mean femoral cartilage thickness of 1.33 mm (Figure 19).

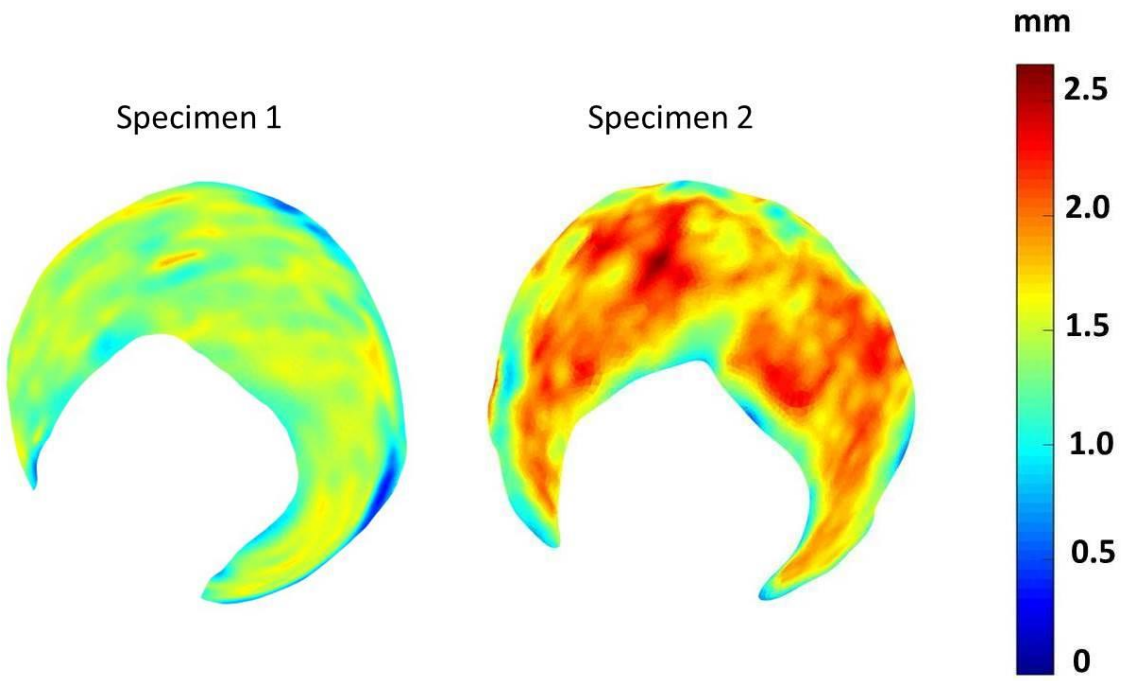

Figure 19 – Acetabular cartilage thickness maps for Specimen #1 (left) and Specimen #2 (right).

Comparisons between Tekscan measured and DEA computed contact stress for intact Specimen #1 are shown in Table 1 and Figure 20. Overall, locations of high contact stress were visually similar between the Tekscan and DEA contact stress distributions. The peak contact stress for the Tekscan was 2.76 MPa vs. 3.32 MPa for the DEA. Contact areas were 1,027 mm^2 and 940 mm^2 for the Tekscan and DEA, respectively. The posterior wall fracture and malreduction increased the contact stresses and decreased the contact area for both DEA and Tekscan. In the fractured case, the peak contact stress for the Tekscan was 4.65 MPa compared to 5.51 MPa for DEA. The contact area was 572 mm^2 and 515 mm^2 for the Tekscan and DEA, respectively.

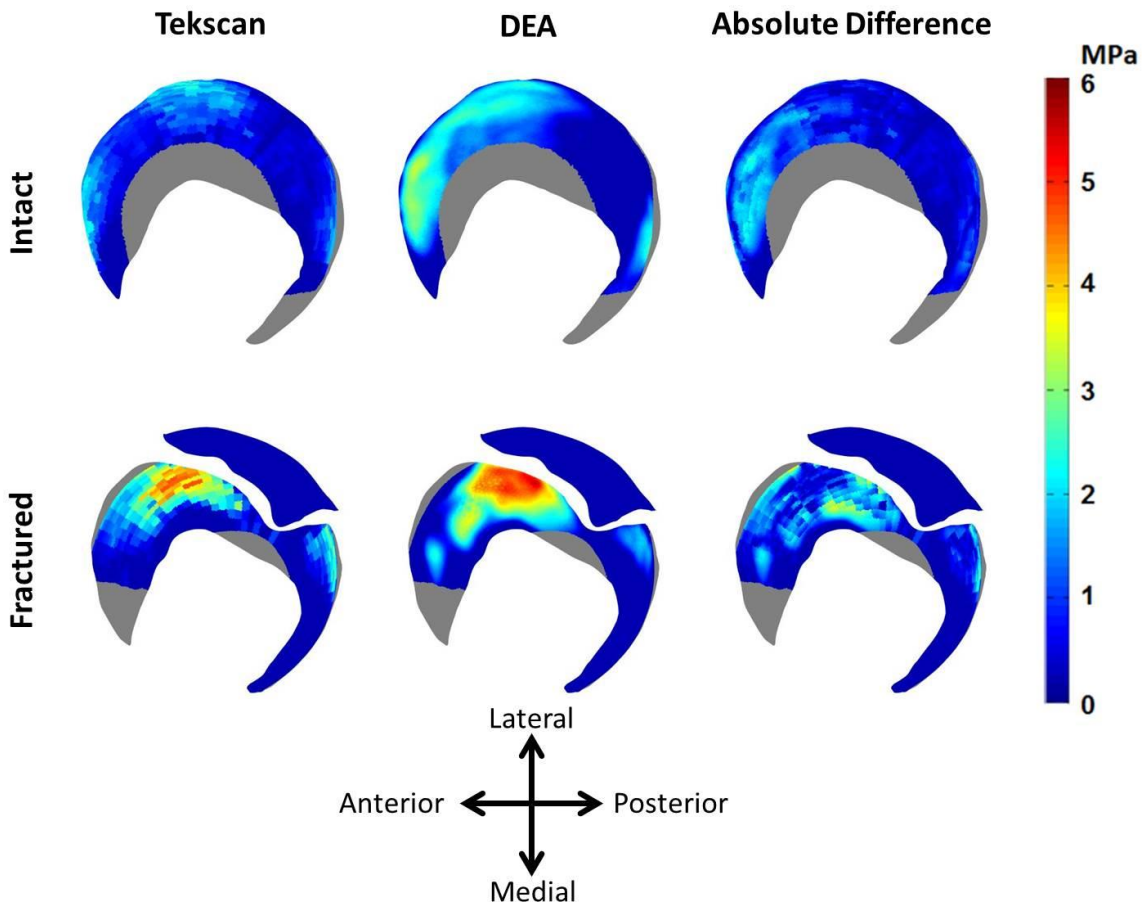

Figure 20 – Comparisons between Tekscan-measured and DEA-computed contact stresses for Specimen #1 intact (top) and Specimen #1 malreduced fracture (bottom). Areas of articular cartilage that were not covered by the Tekscan sensor during testing are colored grey and were not included in contact stress comparisons. A difference plot (right) was computed on a face-by-face basis taking the absolute value of the difference between the Tekscan measurements and DEA computations. Blue patches on the difference map show high agreement and red patches are regions with poor agreement.

Specimen #1	Max Contact Stress (MPa)		Contact Area (mm^2)	
	Tekscan	DEA	Tekscan	DEA
Intact	2.76	3.32	1,027	940
Fractured	4.65	5.51	572	515

Table 1 – Maximum contact stress and contact area comparisons between Tekscan measurements and DEA computations for the intact and malreduced fractured case of Specimen #1.

The DEA tended to predict slightly higher contact stress than the Tekscan measurements, giving the majority of the faces a positive contact stress difference. The DEA predicted a greater amount of area with high contact stress and a lower amount of area with low contact stress compared to Tekscan measurements. Overall, 81% of the articular cartilage surface area had a difference $\leq \pm 1$ MPa and 99% of the surface area had a difference $\leq \pm 2$ MPa. In the fractured case 71% of the articular cartilage surface area had a difference $\leq \pm 1$ MPa and 93% of the surface area had a difference $\leq \pm 2$ MPa. Overall correlation between the Tekscan and DEA was 97% for the intact case and 94% for the fractured case.

The spatial distribution of DEA computed contact stresses using the approximated cartilage was visually similar to the experimentally measured contact stresses with bimodal contact anterior and posterior to the fragment. The maximum contact stress was anterior to the fragment and the DEA actually had a closer peak contact stress to the experimental results (4.65 MPa) with the approximated cartilage (4.78 MPa) than the manually segmented cartilage (5.51 MPa) (Figure 21). Overall correlation between the approximated cartilage and Tekscan was 97%.

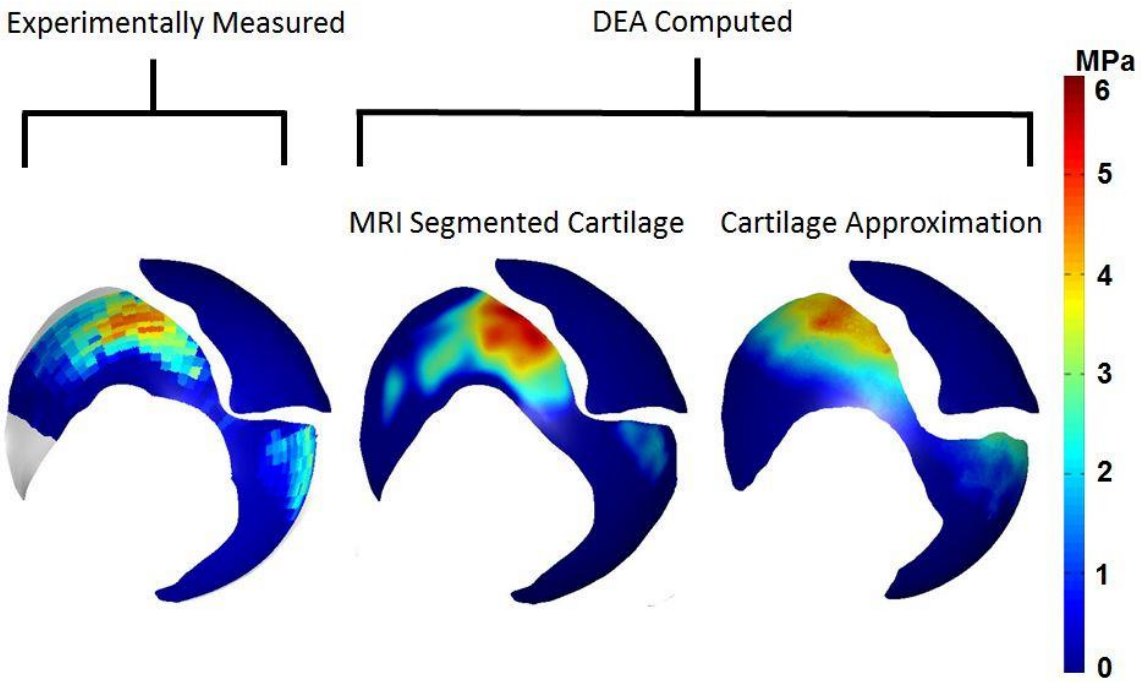

Figure 21 - Contact stress distributions for experimentally measured (left), DEA computed using manually segmented cartilage (middle) and DEA computed using cartilage approximated based on bony geometry (right).

The number of smoothing iterations performed on the approximated cartilage surface was empirically found by directly comparing the contact stress distributions and maximum contact stress at each iteration to the experimentally measured contact stresses. Using a maximum radial change of 0.05 mm per iteration, resulted in 5 smoothing iterations to most closely match experimental measurements (Figure 22).

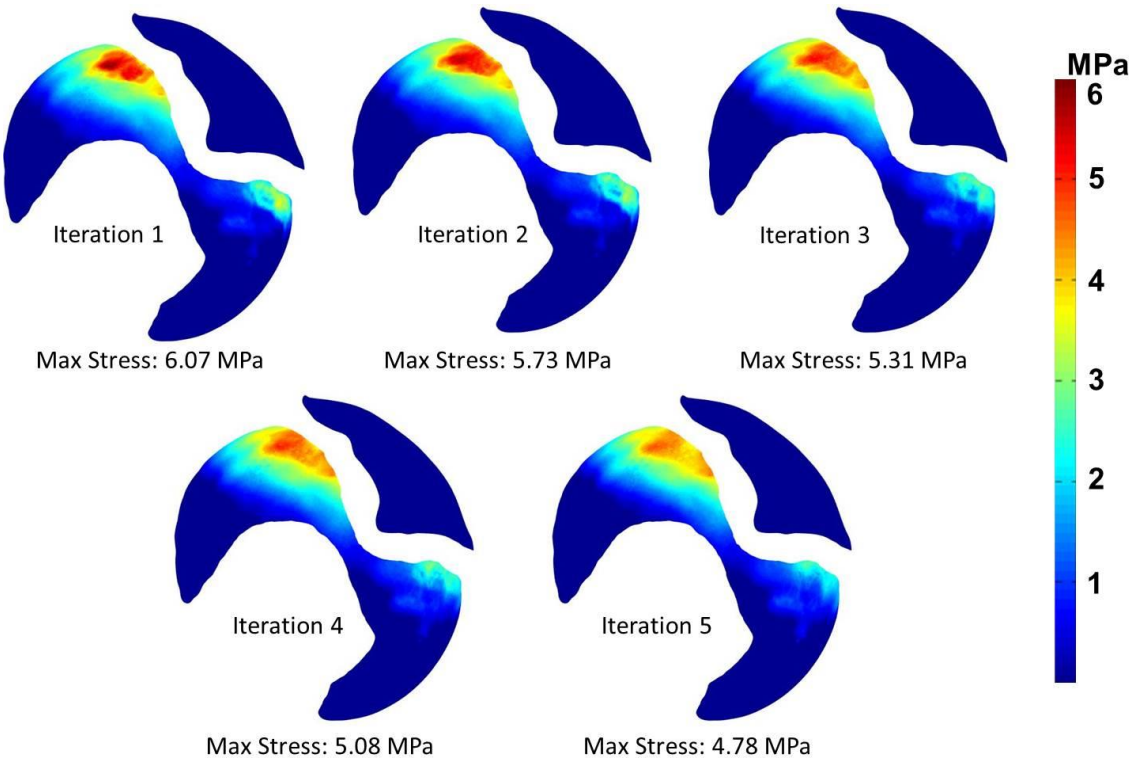

Figure 22 – DEA computed contact stress using approximated cartilage that was generated by uniformly projecting the subchondral bone 1 mm. A custom algorithm was used to smooth the cartilage surface which decreased the maximum contact stress after each smoothing iteration.

In Specimen #2, which was tested at three instances of the gait cycle, the spatial location of high contact stresses was visually similar between DEA and Tekscan measurements (Figure 23). During heel-strike, DEA predicted a maximum contact stress of 5.90 MPa and contact area of 719 mm^2 compared to Tekscan measurements of 5.74 MPa and 642 mm^2. At mid-stance DEA predicted a maximum contact stress of 6.35 MPa and contact area of 472 mm^2 compared to Tekscan measurements of 6.82 MPa and 361 mm^2. At toe-off DEA predicted a maximum contact stress of 5.47 MPa and contact area of 446 mm^2 compared to Tekscan measurements of 5.10 MPa and 396 mm^2 (Table 2)

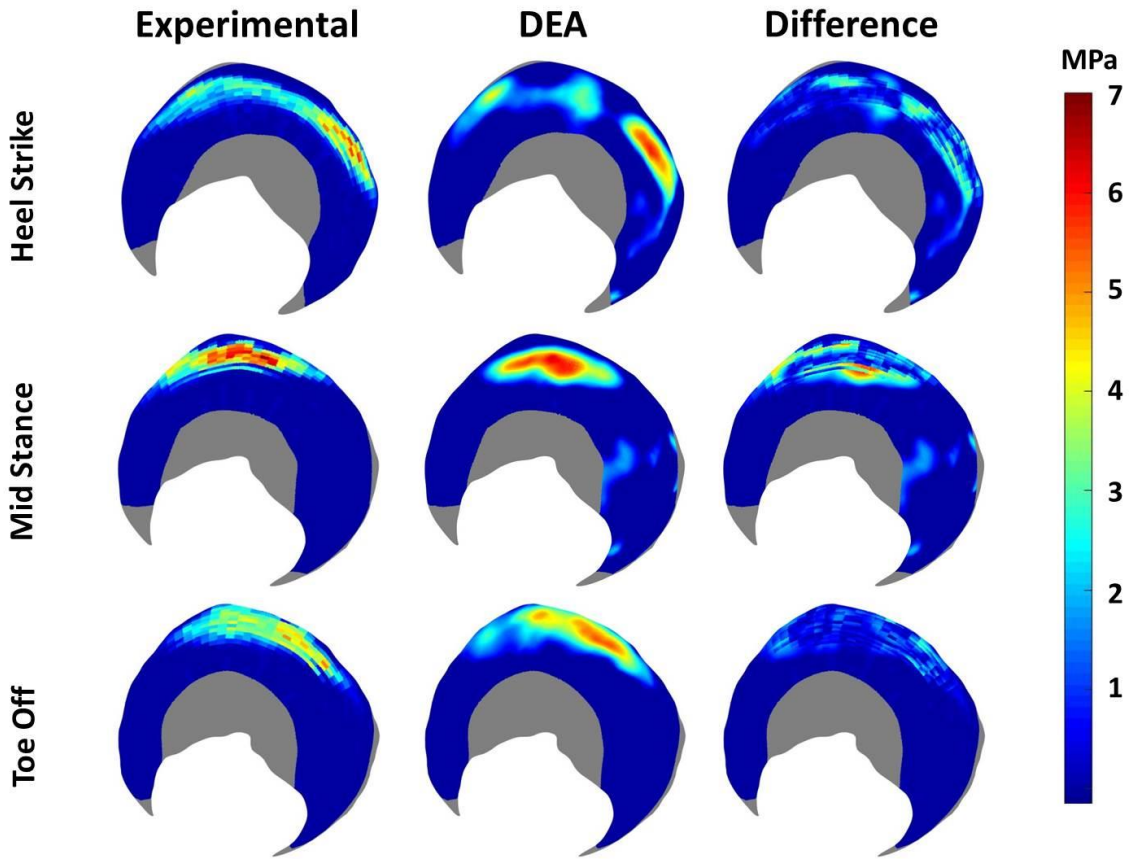

Figure 23 - Comparisons between Tekscan measured and DEA computed contact stresses for Specimen #2 during heel-strike (top), mid-stance (middle), and toe-off (bottom) using cartilage surfaces manually segmented from MR images.

Specimen #2	Max Contact Stress (MPa)		Contact Area (mm^2)	
	Tekscan	DEA	Tekscan	DEA
Heel-Strike	5.74	5.90	642	719
Mid-Stance	6.82	6.35	361	472
Toe-Off	5.10	5.47	396	446

Table 2 - Maximum contact stress and contact area comparisons between Tekscan measurements and DEA computations for Specimen #2 at heel-strike, mid-stance, and toe-off.

At heel-strike, 81% of the articular cartilage surface area had a difference ≤ ±1 MPa between DEA and Tekscan and 93% of the surface area had a difference ≤ ±2 MPa. At mid-stance 80% of the articular cartilage surface area had a difference ≤ ±1 MPa and 91% of the surface area had a difference ≤ ±2 MPa. At toe-off 92% of the articular cartilage surface area had a difference ≤ ±1 MPa and 99% of the surface area had a difference ≤ ±2 MPa. Overall correlation between Tekscan and DEA was 94% for heel-strike, 93% for mid-stance, and 98% for toe-off

For further validation of DEA accurately predicting contact stress using approximated cartilage, the cartilage approximation methodology was repeated in Specimen #2 for heel-strike, mid-stance, and toe-off (Figure 24). The DEA model predicted a maximum contact stress of 6.04 MPa at heel-strike and had a 93% correlation with Tekscan measurements. At mid-stance, the DEA model predicted a maximum contact stress of 6.48 MPa and had a 92% correlation with Tekscan. Lastly, the DEA model predicted a maximum contact stress of 5.51 MPa at toe-off and had a 93% correlation with Teskcan.

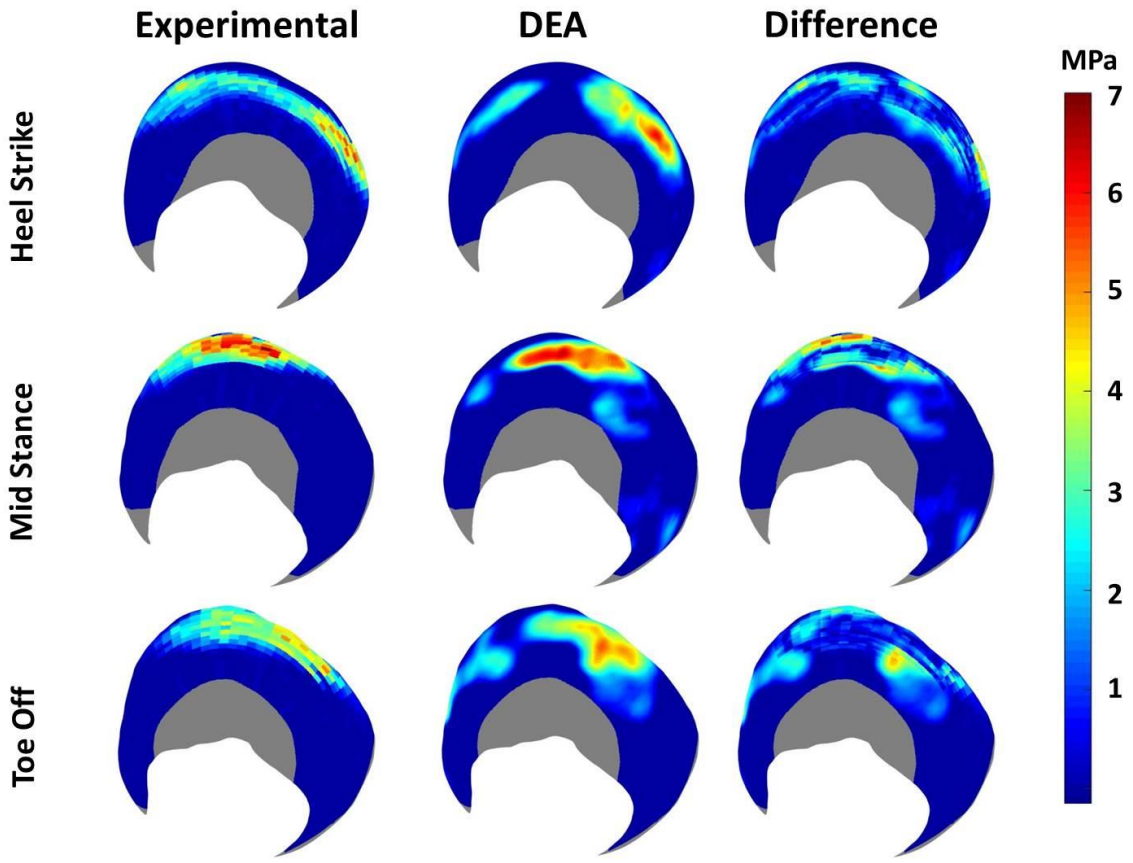

Figure 24 – Comparisons of experimentally measured and DEA-computed contact stress distributions using approximated cartilage surfaces for three phases of walking gait.

2.4 Discussion of Results

Point-by-point comparisons between physical measurements and DEA-computed contact stresses were made in both an intact hip and a malreduced fractured hip. In this study, DEA predicted slightly higher contact stresses than Tekscan measurements, confirming previous studies in which DEA has been shown to slightly overestimate contact stress values [42, 46, 62]. The DEA tended to slightly overestimate values in regions of high contact stress and also underestimate values in regions of low contact stress. Much of this discrepancy occurs along edges of contact surfaces. This tendency is likely due to the inability of DEA to model cartilage deformation occurring parallel to the

cartilage surface during physical testing. The articular cartilage surface is modeled as a set of linear springs that are perpendicular to the cartilage surface and independent from one another. The inability of faces to be influenced by neighboring faces in contact prevents the surface from adapting to regions of high contact stress through deformation. Such deformation would allow the load to be distributed over a larger area and therefore decrease the contact stress.

As expected, the fractured hip exhibited higher peak contact stress and lower contact area in both the Tekscan and DEA-computed contact stresses. In both physical testing and in DEA computations, a 2mm step-off was significant enough to prevent any contact between the displaced fragment and femoral head, decreasing the area of the acetabular cartilage in contact. This decrease in contact area caused the peak contact stress to be 68% greater in Tekscan measurements and 66% greater in DEA computations than the intact case. A previous study investigated the change in peak contact stress after malreduced transverse acetabular fractures in five human cadavers [66]. Results showed that perfectly reduced fractures did not change the peak contact stress but step-off of greater than 1 mm led to significantly increased contact stress. A step-off of 2 mm caused the peak contact stress to increase approximately 50%, a magnitude similar to our results.

The DEA computed contact stresses using the approximated cartilage for the fractured case of Specimen #1 actually had a better correlation (97%) with the Tekscan measurements than the patient-specific manually segmented cartilage (94%). The DEA predictions using approximated cartilage in Specimen #2 had high correlation (≥92%) with Tekscan measurements at three different phases of the walking gait cycle. These results suggest the cartilage approximation method is sufficiently accurate for predicting patient-specific contact stresses in hip joints when MRI data is not available for cartilage segmentation.

During initial testing on Specimen #2, there was an error in replicating the orientation of the hip in the heel-strike, mid-stance, and toe-off positions. When going

from heel-strike to toe-off, the majority of the motion is flexion/extension of the femur. However, an error relating the Bergmann coordinate system to the cadaveric coordinate system caused the changes in the hip position to be primarily in adduction. This created an opportunity to validate the DEA model in another range of motion important in movements such as sit-to-stand, turning, and running [67-69]. Between the three testing instances, the range of abduction was -4˚ to 11˚. The highest contact stresses occurred at 11˚ which was 6.84 and 6.80 MPa for the DEA and Tekscan, respectively. At 5˚ abduction, DEA predicted a maximum contact stress of 4.88 MPa compared to Tekscan measurement of 4.66 MPa. At -4˚ abduction DEA predicted a maximum contact stress of 5.53 MPa and Tekscan measured 5.27 MPa. Again, these results were not only similar in magnitude but in location (Figure 25).

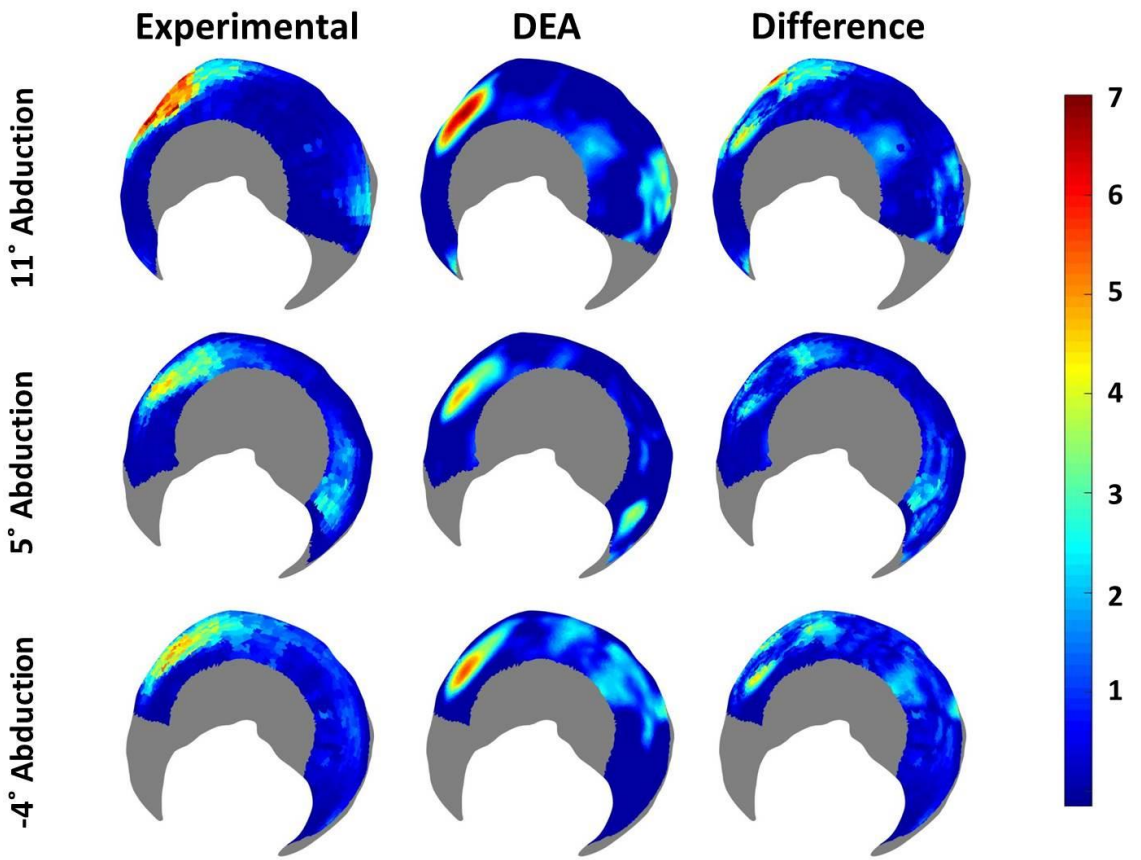

Figure 25 - Comparisons between Tekscan measured and DEA computed contact stresses for Specimen #2 during different degrees of abduction.

There are several limitations to this study. First, imperfect segmentations can alter cartilage thicknesses and the morphology of contact surfaces in the DEA model. Since the DEA models are based on semi-automated and manual segmentation of cartilage and bone surfaces, there will be some degree of error resulting from human interaction. Even sub-millimeter changes in cartilage thickness or a few degrees of rotation can alter the DEA contact stress distribution [62]. Secondly, the true stiffness of each specimen's cartilage under a prolonged static load is unknown. The contact stresses calculated by the DEA model scale linearly with Young's modulus, which was one of the estimated parameters based on values in the literature. Since DEA tends to over-predict contact

stress, decreasing the estimated Young's modulus would bring the contact stress magnitudes closer to Tekscan measured values. Lastly, the mechanism and to what degree the cartilage was smoothed is an important factor in the contact stress calculations. Under-smoothing the cartilage surface maintains incongruities from segmentation artifact which do not actually reside on the specimen's cartilage and can cause patches of elevated contact stress. Over-smoothing the cartilage surface can create a perfectly spherical surface absent of any minor imperfections that are present on the specimen's cartilage. A larger degree of smoothing would increase the contact area and decrease the DEA computed contact stress.

In conclusion, DEA proved to be a reliable computational method capable of expedited contact stress estimations in both healthy and fractured hips throughout the gait cycle. The DEA method is a stable computational method that had no convergence issues with any model we used. Run times were on the order of 1-2 minutes, making DEA an appealing computational method for large population studies with hundreds or more patient-specific models. DEA also provides a significant reduction in investigator time compared to FEA which requires a mesh generation process. In the future this validated DEA model may prove useful for predicting contact stresses in a variety of clinical applications.

CHAPTER 3: PERIACETABULAR OSTEOTOMY-INDUCED CHANGES IN JOINT MECHANICS

3.1 Background and Motivation

3.1.1 Developmental Dysplasia of the Hip

Developmental dysplasia of the hip (DDH) is an abnormality that involves irregular development of the acetabulum and/or the femoral head. Dysplastic hips have a shallow acetabular cup and may also have other concurrent deformities such as a shortened femoral neck or non-spherical femoral head [6]. Because of the shallow acetabulum and inadequate lateral coverage of the femoral head, the normal forces across the hip joint are applied over a smaller area, leading to increased loading along the acetabular rim. DDH has a wide spectrum of severity, from nearly concentrically located to severely dysplastic and dislocated [5, 6]. Mild dysplasia often does not become apparent until adulthood when the patient begins to develop OA, whereas severe dysplasia is likely to cause dislocation early in life and be acted upon during infancy. Approximately 11 in 1,000 children have DDH severe enough to be born with a dislocated or subluxated hip [7]. For less severe cases to be detected, it is recommended for physicians to perform physical examinations on newborns using dynamic tests such as the Barlow and Ortolani maneuvers [70, 71]. The Barlow maneuver is performed on an infant laying supine on a table by adducting the hip while applying pressure on the knee, directing the force posteriorly. If the hip is posteriorly dislocated, the test is positive. The Ortolani maneuver is used to relocate the femoral head anteriorly into the acetabulum while feeling and hearing for a distinctive ‘clunk’, signaling successful relocation and confirming a positive Barlow test. If these tests are inconclusive, medical imaging is necessary for the diagnosis of hip dysplasia [72].

Diagnosis is largely based on the center edge angle, a measure of the femoral head coverage derived from anterior-posterior radiographs. The angle is defined between

a vertical line through the center of the femoral head and a line from the rim of the acetabulum to the center of the femoral head (Figure 26). The mean center-edge angle in normal hips is 33˚ with a 95% confidence interval of 23˚-43˚, with smaller center-edge angles indicating greater dysplasia [73].

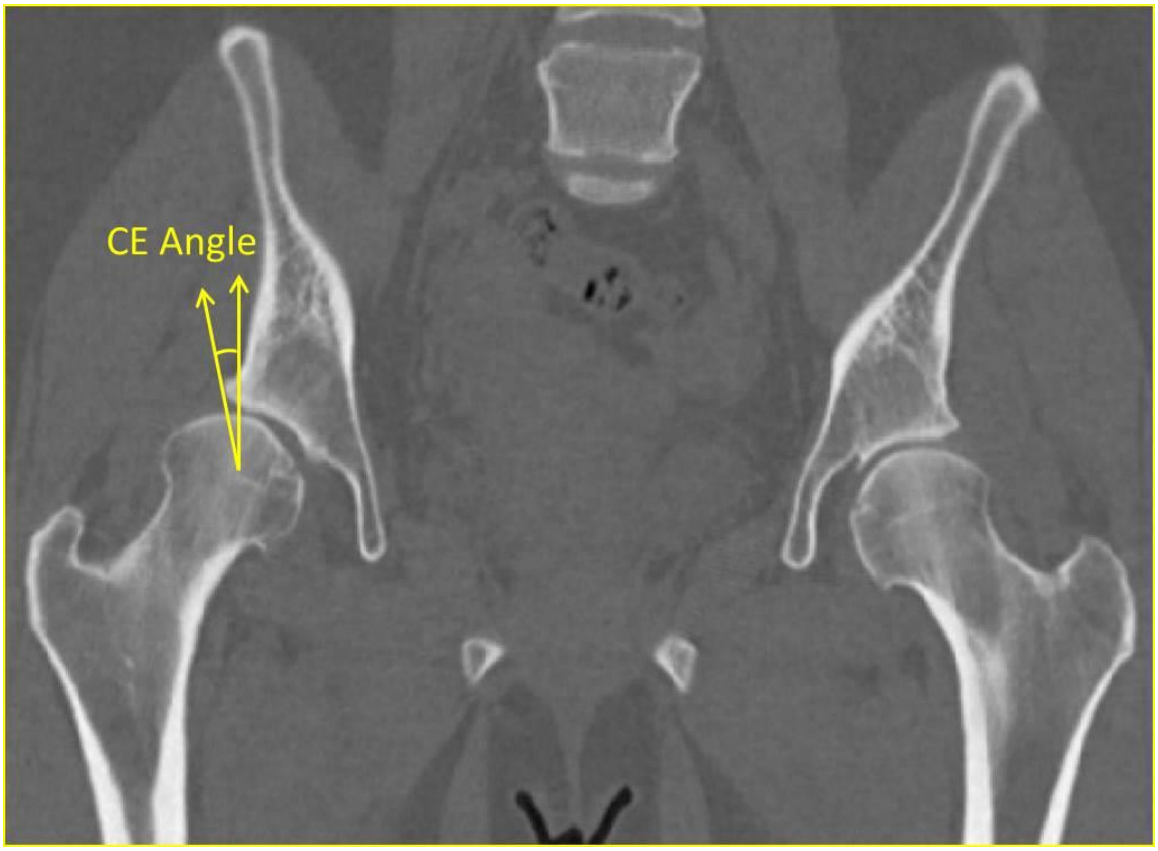

Figure 26 – Coronal CT image of a patient with severe hip dysplasia in the right hip. The shallow acetabular cup drastically decreases the CE angle.

Computational models based on CT data have shown that the maximum load along the acetabular rim can be more than double in dysplastic hip joints compared to nondysplastic hip joints [74]. A similar study showed calculated pressures were 23% greater in dysplastic hips compared to nondysplastic hips, and contact area was 26% less

in dysplastic hips [75]. Over time, this increased stress can lead to labrum hypertrophy, degeneration of the articular cartilage, and osteoarthritis [5-7].

If untreated, DDH has been shown to increase the risk of OA development at a much earlier age than normal hips. Up to 45% of young adults (< 50 years old) that develop OA in the hip do so because of hip dysplasia [76]. DDH is the cause of up to 29% of hip replacements in people under the age of 60 [77].

Treatment of DDH is dependent upon both the severity of the deformity and the time of detection. The aim of any DDH treatment is to achieve concentric reduction of the hip to an anatomical position while avoiding avascular necrosis. For cases that are mild or detected in infancy, a non-surgical approach such as the Pavlik harness has been shown to have a success rate of 95% [78, 79]. For non-infant or more severe cases, a surgical approach is often necessary.

3.1.2 Periacetabular Osteotomy

In 1984, orthopaedic surgeon Dr. Reinhold Ganz performed the first periacetabular osteotomy (PAO) for hip dysplasia [80]. Since then, this method has become the most commonly used surgical procedure for treating DDH in young adults. The goal of the surgery is to increase the contact area in the hip joint in order to stabilize the joint and reduce contact pressure. The PAO procedure allows for re-alignment of the entire acetabulum, and thus the acetabular cartilage relative to the femoral head. Reorientation causes medial and lateral displacement of the acetabulum [80]. Three osteotomy cuts are performed; a partial osteotomy of the ischium at the infracotyloid groove, complete osteotomy of the pubis immediately adjacent to the acetabulum, and a biplanar roof shaped osteotomy of the ilium (Figure 27). The posterior column remains intact. The acetabular fragment is rotated anteriorly and laterally while maintaining anteversion and is then medialized. After preliminary fixation of the fragment with Kirschner wires, the motion of the hip is tested and if necessary improved by

reorientation of the acetabular fragment. The re-alignment leads to better distribution of forces across the hip joint and can prevent damage to the acetabular labrum and articular cartilage. This procedure is currently the preferred method due to its ability to provide correct alignment while minimizing surgical exposure and complications. A single incision enhances recovery time and preservation of the posterior column of the acetabulum enables weight-bearing activities post-operatively.

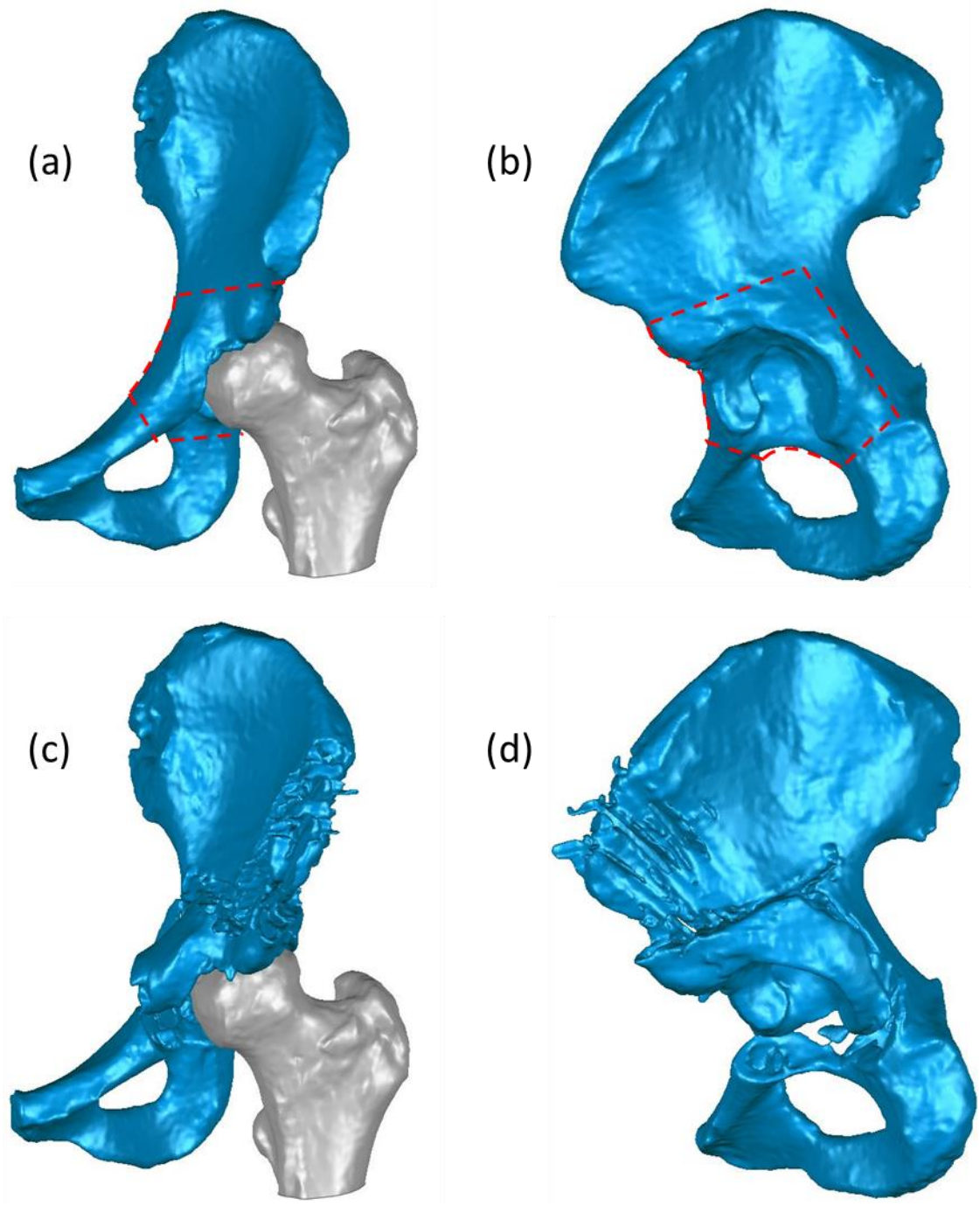

Figure 27 - Virtual representation of a periacetabular osteotomy. Pre-operative coronal view (a) and sagittal view (b) of the pelvic bone cut around the acetabulum (dashed lines). Post-operative coronal view (c) and sagittal view (d) of the rotation of the acetabulum to increase coverage of the femoral head.

Previous surgical techniques used to treat DDH were double or triple osteotomies [81, 82]. These techniques were limited by attached muscles and ligament connections to the sacrum, resulting in notable asymmetry of the pelvis [80, 83]. Compared to previous osteotomy techniques, the PAO procedure has several advantages. (1) Only one incision is required; (2) freedom of reorientation in all directions including medial and lateral displacement; (3) blood supply to the acetabulum is preserved; (4) the posterior column of the hemipelvis remains intact, allowing for walking immediately after surgery without external fixation devices; (5) the shape of the pelvis is unaltered, eliminating any increased risk of complications during future child delivery in female patients.

Perry et al. reviewed PAO outcomes from 13 different studies by looking at the rate of survivorship, with survival defined as not requiring total hip arthroplasty or arthrodesis [76]. They found survivorship ranged from 60% (n = 41) after 20 year follow-up to 100% (n = 24) after 1 year follow-up. Radiological progress of arthritis was seen in as few as 5% (n = 123) of patients after 4 years [84]. The 20 year follow-up study may have underestimated the success of the PAO as it included patients with multiple diagnoses besides PAO. There have also been several refinements to the PAO technique over the past 20 years such as precise correction of the acetabulum in all planes with special attention to avoid retroversion and a concerted effort to keep the labrum intact due to its role in joint stability. Overall, these studies show the success of the PAO procedure to treat hip dysplasia.

3.1.3 Previous Studies on Periacetabular Osteotomy-Induced Changes in Joint Mechanics

Many previous studies have used computational modeling, experimental testing, and evaluation of clinical outcome scores to assess the changes in joint mechanics following PAO surgery. One study used a stereologic method to compare reconstructed CT scans of 6 dysplastic hips that underwent PAO surgery and found that the contact area

on the femoral head increased by 50% on average [85]. Another study using a rigid body spring model found an increase in contact area following PAO surgery and predicted that subluxation was nonexistent in hips with a center edge angle greater than 30 degrees [86]. Clinical studies have found outcome scores improved after PAO surgery. A comparison of pre-operative and 1 year post-operative Harris Hip Score (HHS) in 25 PAO patients showed an average increase from 78.08 (47 to 96) to 95.36 (88 to 100) [87]. These studies suggest periacetabular osteotomies cause beneficial changes in joint mechanics which can help prevent osteoarthritis development in dysplastic hips. With better understanding of how periacetabular osteotomies alter hip joint mechanics, improvements can be made to surgical planning, intra-operative assessment of acetabular reorientation, and ultimately patient outcomes.

Currently, reorientation of the acetabulum is mostly based on the surgeon's experience and best judgment, and very little formal pre-operative planning occurs for PAO procedures. In an effort to preemptively determine optimal surgical correction, Zou et al. used CT scan based subject-specific FEA to identify optimal positions of the acetabulum in a PAO procedure [88]. Each model was iteratively rotated in 5˚ increments, up to a maximum of 20˚ from the original CE angle. The optimal position was selected as the center-edge angle with the minimum contact pressure and maximum contact area. While this methodology is able to find the center-edge angle that optimizes contact stress and contact area, the study largely ignores the effect of anteversion, which has been shown to have a significant impact on the outcome of PAO procedures [89].

Armiger et al. utilized DEA to perform 3D mechanical evaluation of 12 PAO patients and attempted to correlate mechanical results to 2 and 10 year clinical outcomes [52]. The DEA model predicted a lower maximum contact pressure in eleven of the twelve patients, with one patient having a 5% increase in maximum contact pressure, likely due to a large increase in anteversion. All twelve patients showed an increase in contact area. Correlations between DEA results and clinical outcomes were poor due to

the small number of cases. Statistical power analysis based on the data observed in the study showed that 50 cases would have been required to demonstrate significant correlation. While there have been previous good studies which have used computational modeling to estimate optimal patient-specific center edge angles [52, 88], little work has been done to characterize patient-specific changes in joint mechanics following PAO. In an attempt to better correlate clinical outcome scores to changes in joint mechanics following PAO surgery, we performed a study on a larger number of PAO patients using the validated DEA methodology to compare patient-specific changes in joint mechanics to three clinical outcome scores.

3.2 Contact Stress Computational Methods

Nineteen subjects were chosen retrospectively for analysis based on the completeness of their SF-36, HHS, and WOMAC clinical outcome scores for correlation with changes in joint mechanics (Table 3). All patients were operated on by the same orthopaedic surgeon at the University of Iowa Hospitals & Clinics in Iowa City, IA, USA between 2007 and 2009. The median age of the 19 patients was 29 years (14-50 years). Institutional Review Board approval was obtained for this work.

Patient ID	Age (years)	Weight(kg)	Pre-Op CE Angle (˚)	Post-Op CE Angle(˚)
1	33	93.29	32	43
2	29	59.78	42	44
3	14	71.6	20	34
4	38	100.6	18	43
5	15	46.3	25	37
6	24	88	27	31
7	26	86.5	15	33
8	42	102.8	15	38
9	34	102.9	12	32
10	17	81.64	26	38
11	19	96.9	29	38
12	19	72.9	13	30
13	47	72.39	19	44
14	36	71	3	29
15	45	65	17	31
16	28	88.09	16	36
17	31	107.39	20	34
18	17	75.69	22	29
19	50	61	23	37

Table 3 – Patient summary information including age, weight, and pre-op and post-op center-edge angles.

3.2.1 Model Creation & Alignment

Patient-specific model pairs were generated by segmenting the femur, pelvis, and spine from pre-operative and post-operative CT scans using the same semi-automated program developed in MATLAB that was used for validation model development [60].

After segmentation, the models had to be aligned to a common coordinate system for loading. The alignment step was required because CT acquisition is performed with the patient lying down, and the patient's hip is not in the same apposition every time. Therefore, each model was aligned to the Bergmann coordinate system [20] using

Geomagic Studio. In the program, the centers of the femoral heads and the center of the L5-S1 vertebrae defined the X-Z plane. A line passing through the center of the femoral heads defined the X-axis, pointing in the medial direction. The Z-axis was perpendicular to the X-axis and goes through the center of the L5-S1 vertebrae in a lateral view. The Y-axis is perpendicular to the X-axis and Z-axis, pointing in the ventral direction. The origin is located at the center of the left femoral head (Figure 28).

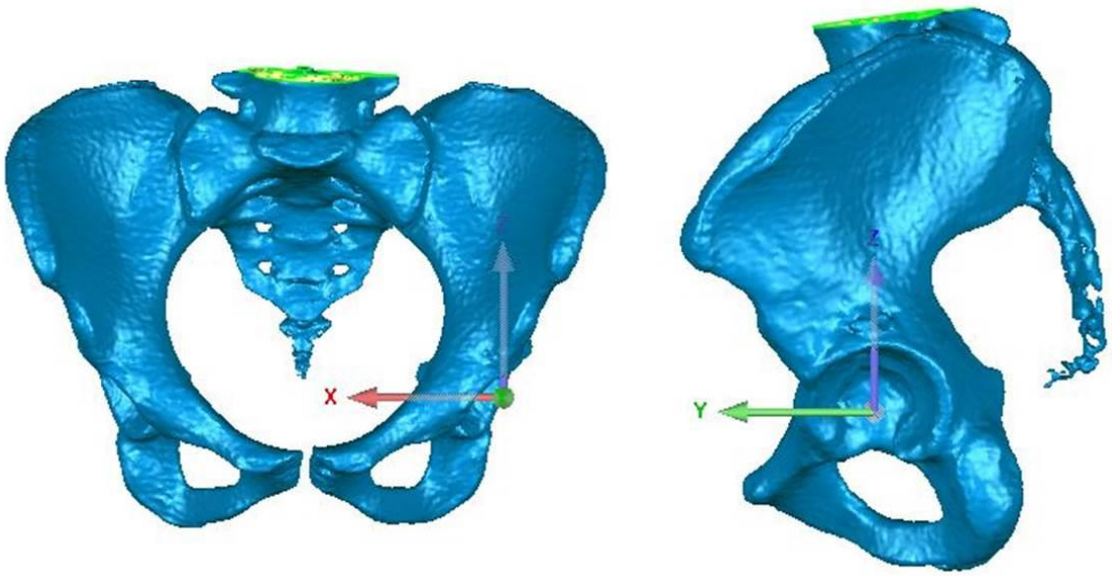

Figure 28 – Coronal view (left) and sagittal view (right) of the hip after alignment to the Bergmann coordinate system.

3.2.2 Cartilage Approximation

Without the addition of contrast, articular cartilage is not visible on CT scans. Therefore, the articular cartilage was approximated based on the underlying bony geometry. After model alignment, the acetabular and femoral head subchondral bone surfaces were uniformly offset into the joint space 1 mm based on previous studies of hip cartilage thickness values [55, 56, 63]. However, due to inter-patient variance in cartilage thickness values, a 1 mm uniform projection from both the acetabular and femoral

subchondral bone caused the articulating surfaces to intersect in areas where the inter-bone distance was less than 2 mm. To account for this, a method similar to one used by Marchelli, et al. [90] was implemented in MATLAB in which cartilage was projected half the inter-bone distance in areas with inter-bone distance less than 2 mm.

After projection from the subchondral bone, the articular cartilage surface required surface smoothing due to the patient's inherent incongruities of the underlying subchondral bone surface. To do so, the previously described custom smoothing algorithm developed in MATLAB was used with a 0.05 maximum radial change per iteration for 5 iterations and a 2mm connected neighbor threshold.

3.2.3 Loading and Boundary Conditions

After model alignment, cartilage approximation, and surface smoothing, the bone and cartilage surfaces were imported into MATLAB for subsequent DEA contact stress estimations. All models were loaded through a normal walking gait cycle using forces and rotations measured from four subjects with instrumented hips [20]. The gait cycle was discretized into 13 discrete static loadings for use in DEA. Forces were scaled based on the subject's body weight. An elastic modulus of 8 MPa and Poisson's ratio of 0.42 was assumed [8, 9].

3.2.4 Clinical Outcome Scores

The median follow-up time was 1.1 years (0.4 – 3.6 years). Clinical data included visual analog scale (VAS) pain scores, Western Ontario and McMaster Osteoarthritis Index (WOMAC), and SF-36 patient health survey. VAS pain scores range from 0-10, with a higher score indicating more severe pain. Several patients had VAS pain scores reported over a range. For simplicity, the score was converted to the mean. For example, a score of 4-6 was assumed as a 5. WOMAC scores range from 0-100 in three different categories; pain, stiffness, and function. A higher score indicates *less* pain, stiffness, and functional limitations. The SF-36 survey has a scaled score based on vitality, physical

functioning, bodily pain, general health perceptions, physical role functioning, emotional role functioning, social role functioning, and mental health. A higher score indicates less disability.

3.3 Contact Stress Evaluation in Periacetabular Osteotomy Patients

In general, PAO increased the lateral coverage of the femoral head in all patients. The median increase in center edge angle was 14˚ (1˚-26˚). The patient with an increase of only 1˚ had a pre-operative center edge angle of 42˚ and didn't require an increase in the lateral coverage of the femoral head but required a change in acetabular anteversion.

DEA contact stress distributions were computed for nineteen subjects during an entire walking gait cycle that was discretized into 13 static poses. Subject #14 had a pre-operative CE angle of 3˚, and the DEA model was unable to converge due to the lack of contact area. This patient was excluded from contact stress comparisons. For the other 18 subjects, the average maximum contact stress was 8.20±2.26 MPa pre-operatively compared to 7.24±1.68 MPa post-operatively, a 12% decrease. Ten patients had a decrease in maximum contact stress, 4 patients had very little change (<1 MPa), and 4 patients actually had an increase (Table 4). As expected, the biggest decreases in maximum contact stress were in patients who had very low pre-operative CE angles. Pre-operatively, the maximum contact stress during the gait cycle tended to occur between mid-stance and toe-off along the acetabular rim, due to the lack of lateral coverage of the femoral head (Figure 29). Post-operatively, the additional coverage of the femoral head provided by the PAO lowered the maximum contact stresses during mid-stance and caused the maximum contact stress to most often occur during heel-strike, the point at which maximum load is applied.

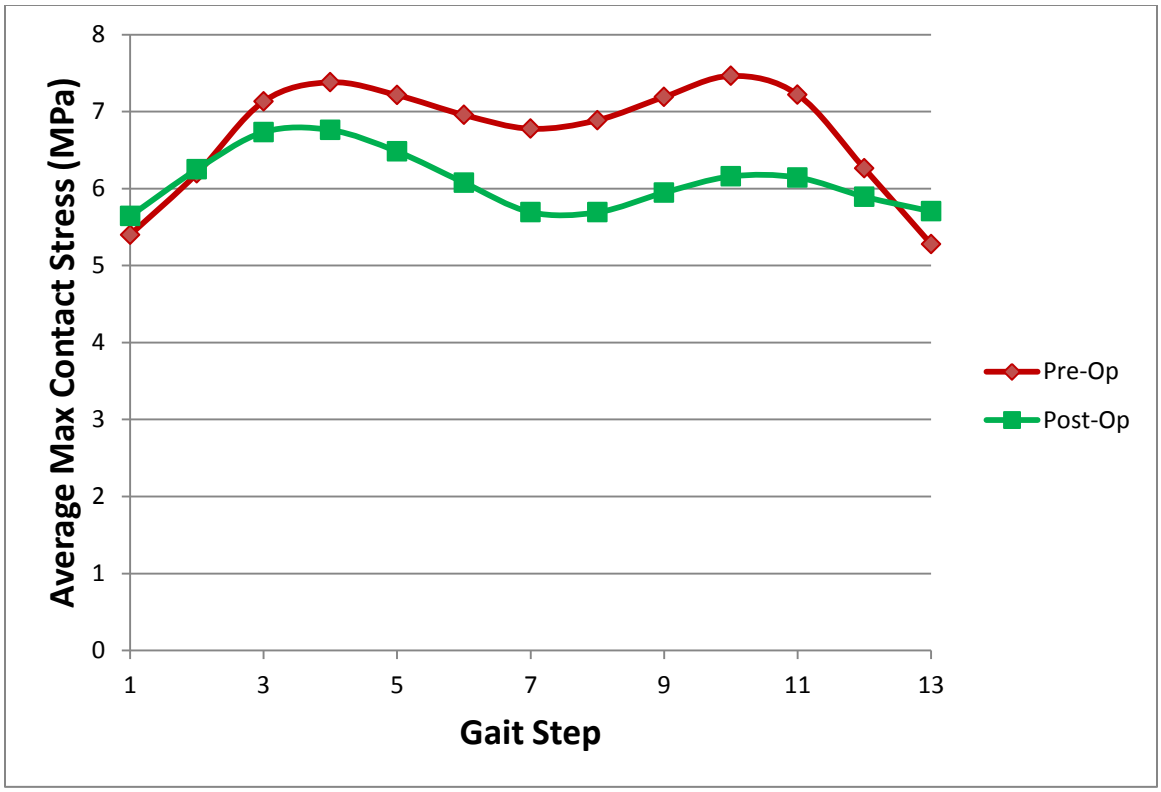

Figure 29 – Plot of the pre-operative (red) and post-operative (green) average maximum contact stress at each step in the gait cycle. Each dot plotted represents an averaged maximum contact stress for all the patients at that particular step.

DEA pre-operative and post-operative results showed the average combined contact area for all patients over the entire gait cycle increased from 888±265 mm^2 pre-operatively to 1,026±267 mm^2 post-operatively, a 16% increase (Figure 30). The biggest difference in contact area pre-operatively and post-operatively was during heel-strike which had a 23% increase post-operatively. Sixteen of the nineteen patients had increased average contact area over the full gait cycle, and seventeen of the nineteen patients had an increase in contact area during heel-strike.

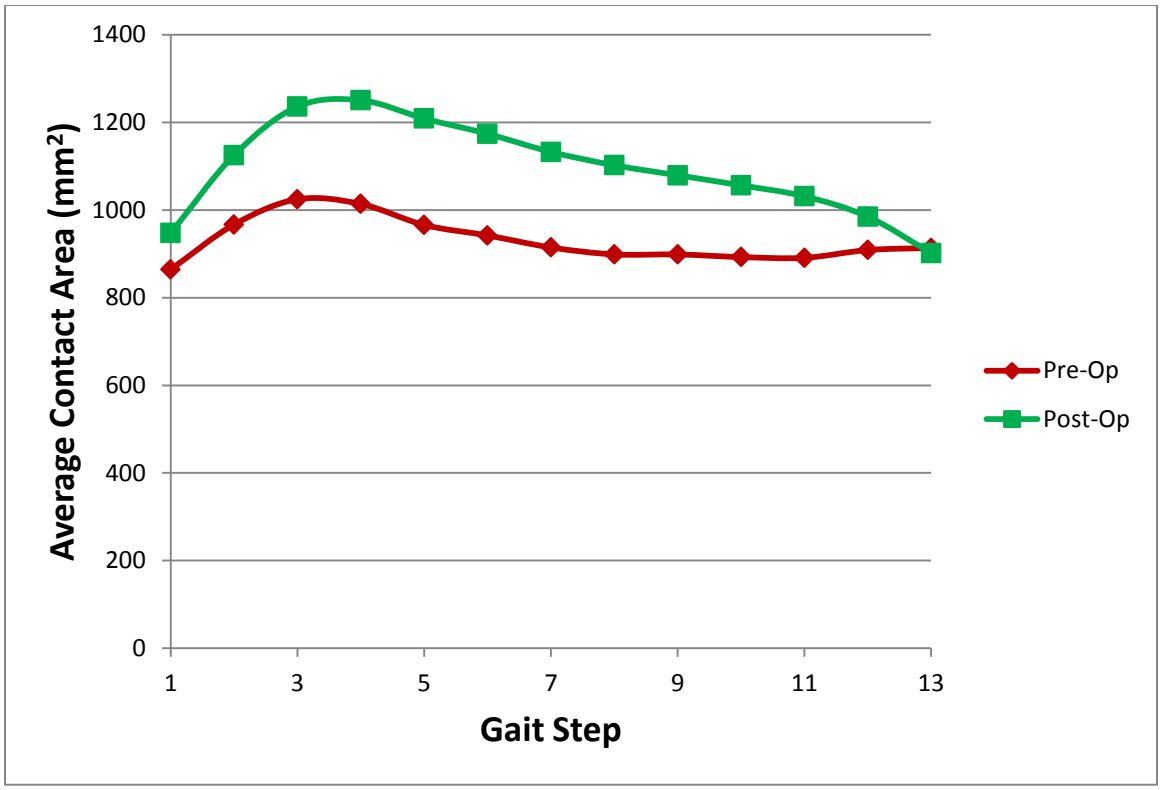

Figure 30 – Plot of the pre-operative (red) and post-operative (green) average contact area at each step in the gait cycle. Each dot plotted represents an averaged contact area for all the patients at that particular step.

Patient ID	Maximum Contact Stress (MPa)		Average Contact Area (mm^2)	
	Pre-Op	Post-Op	Pre-Op	Post-Op
1	8.29	7.26	1,333	1,476
2	4.84	6.07	1,288	1,228
3	5.51	5.75	958	1,065
4	11.85	7.9	759	1,069
5	4.74	3.66	689	783
6	8.06	11.53	1,120	1,263
7	9.33	7.86	921	1,369
8	11.22	7.13	691	1,134
9	11.62	8.39	687	957
10	4.58	5.67	1,050	1,107
11	7.07	8.05	1,340	1,274
12	9.74	6.97	730	792
13	8.28	9.58	733	731
14	N/A	6.28	N/A	674
15	8.39	7.97	651	622
16	9.94	6.68	675	962
17	8.91	7.72	823	891
18	7.56	5.45	964	1,059
19	7.67	7.59	574	699

Table 4 – Summary of maximum contact stress and contact area for the 19 PAO patients.

Figures 31 and 32 show the contact stress distributions for subject #16 over the entire gait cycle. This subject had a 33% decrease in maximum contact stress and 42% increase in average contact area. From the DEA stress maps, it was clear that the patient exhibited higher contact stresses along the acetabular rim pre-operatively (Figure 31). Reorienting the acetabulum decreased the contact stresses over a broader area and shifted the contact stress distribution medially (Figure 32).

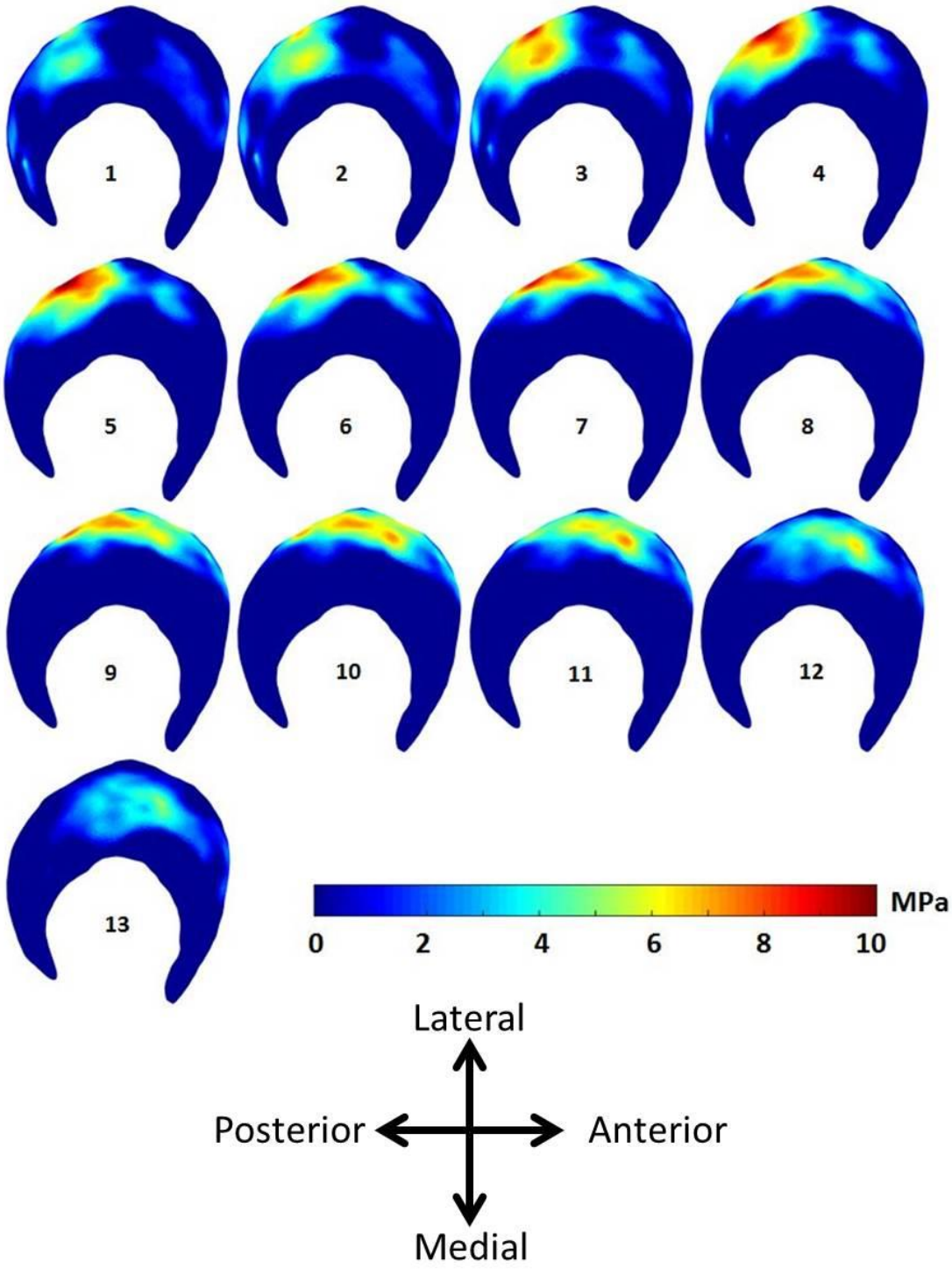

Figure 31 – Pre-operative DEA contact stress distributions of all 13 gait steps in the right hip of Subject #16 who had a low CE angle of 16˚, causing elevated contact stresses along the lateral rim of the acetabular cartilage. The anterior direction points to the right.

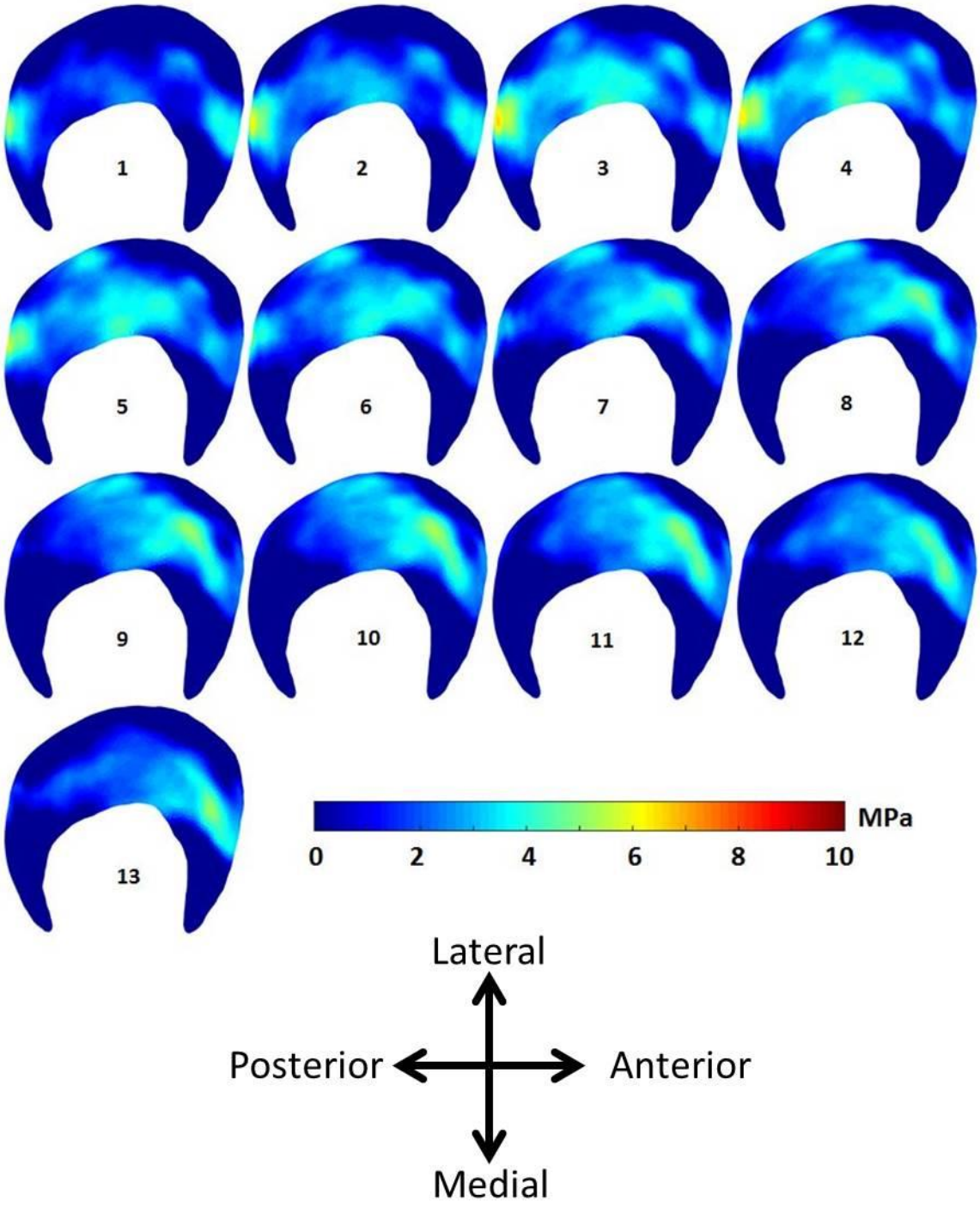

Figure 32 – Post-operative DEA contact stress distributions of all 13 gait steps in the right hip of Subject #16. The CE angle was 36˚ post-operatively, causing the contact stress distribution to be shifted medially over a larger contact area which reduced the contact stresses. The anterior direction points to the right.

3.3.1 Contact Stress Correlation with Short-Term Patient Outcomes

VAS pain scores range from 0 to 10, with higher scores indicating more pain. Changes in VAS pain scores (post-op – pre-op) correlated well with changes in max contact stress ($n = 18$, $R^2 = 0.6024$, $p = 0.001$). DEA tended to predict a lower maximum contact stress post-operatively in patients who experienced a decrease in pain following PAO surgery (Figure 33). DEA also tended to predict an increase in maximum contact stress for patients who experienced an increase in pain.

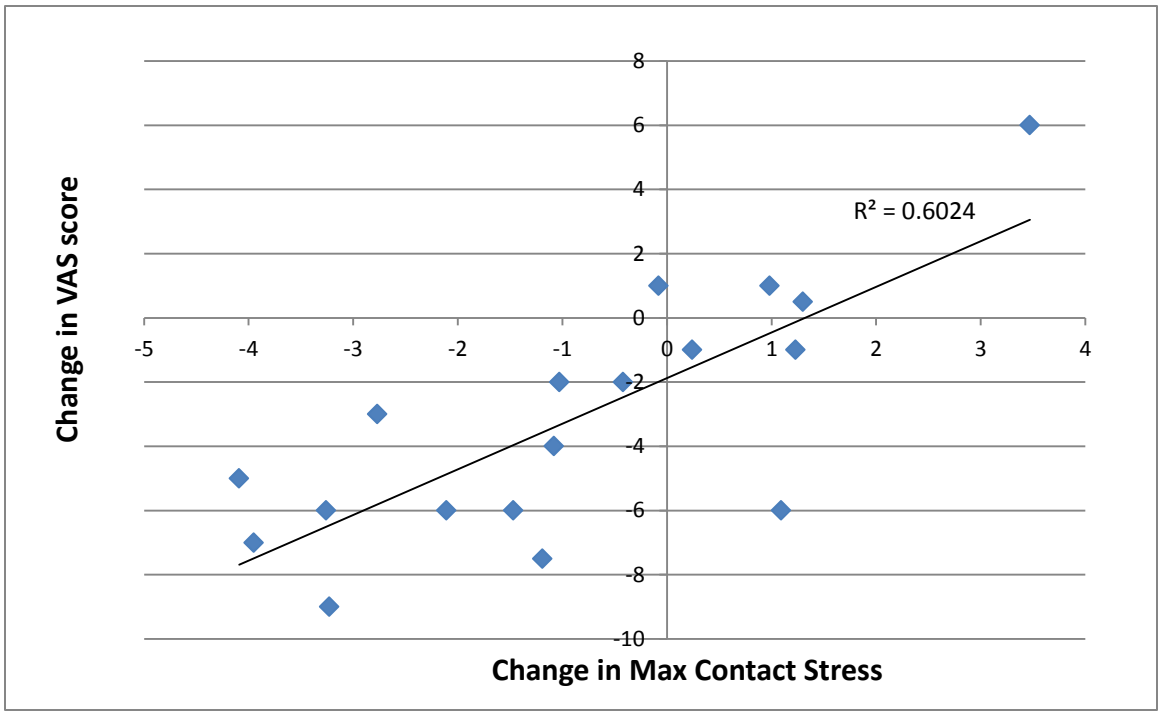

Figure 33 – Pearson correlation between changes in VAS score (post-op – pre-op) and change in maximum contact stress. The DEA tended to predict lower contact stress in patients who experienced less pain.

WOMAC scores range from 0 to 100 in three different categories; pain, stiffness, and function, with a higher score indicating *less* pain, stiffness, functional impairment. For simplicity, each of the three scores was weighted equally and averaged into one

score. Changes in the combined WOMAC score correlated moderately with changes in maximum contact stress (n = 11, R^2 = 0.373, p = 0.046) (Figure 34).

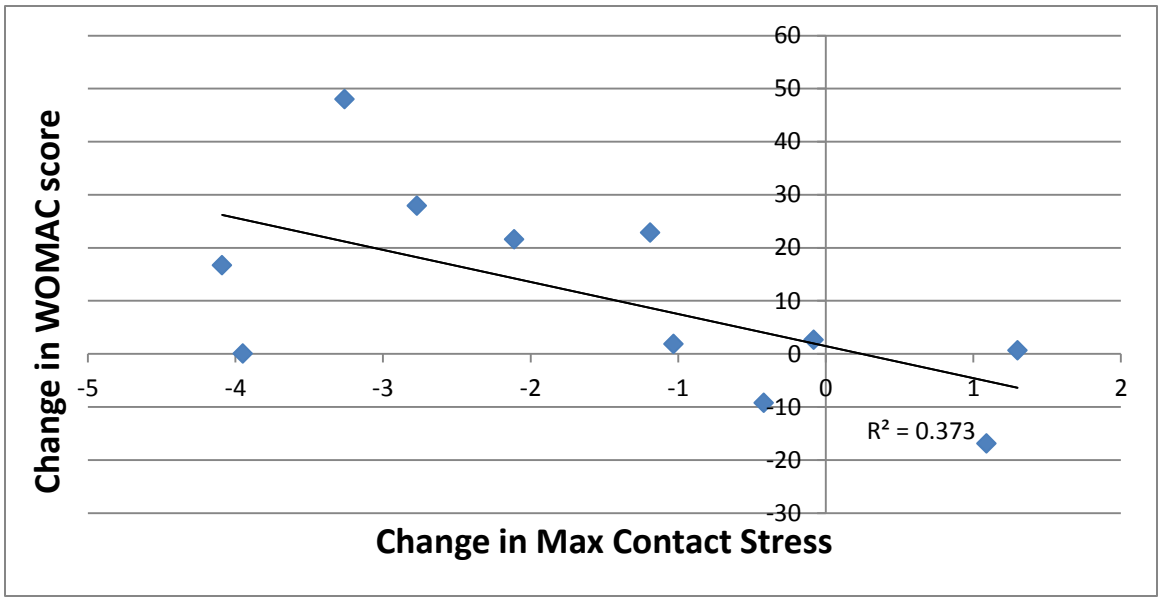

Figure 34 – Pearson correlation between changes in WOMAC score (post-op – pre-op) and change in maximum contact stress. The DEA tended to predict lower contact stress in patients who had improved WOMAC scores.

SF-36 patient outcome surveys consist of eight scores in vitality, physical functioning, bodily pain, general health perceptions, physical role functioning, emotional role functioning, social role functioning, and mental health. The scoring provides a physical and mental component with *higher* scores indicating *less* disability. For this study, only the physical component score was considered. Changes in SF-36 scores correlated well with change in maximum contact stress (n = 11, R^2 = 0.5239, p = 0.012) (Figure 35). A summary of clinical outcome scores for all the patients is shown in Table 5.

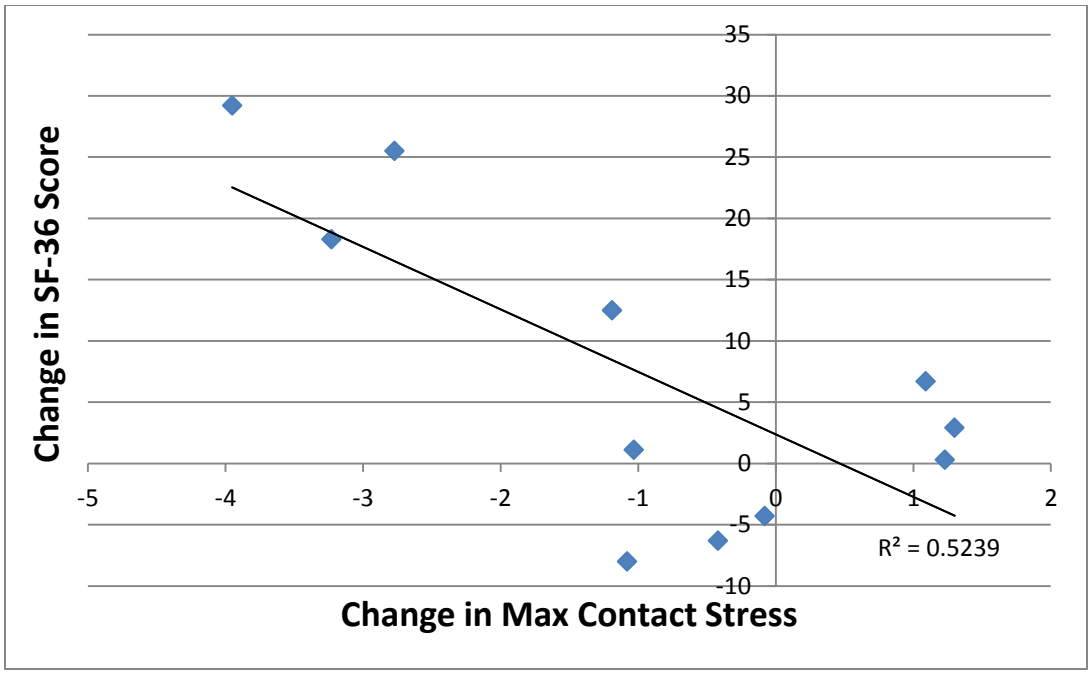

Figure 35 – Pearson correlation between changes in SF-36 scores and change in maximum contact stress. The DEA tended to predict lower contact stress in patients who had improved SF-36 scores.

Patient ID	VAS		WOMAC		SF-36	
	Pre-Op	Post-Op	Pre-Op	Post-Op	Pre-Op	Post-Op
1	4	2	90/62.5/92	80/75/95	50.1	51.2
2	2	1	-	-	51.4	51.7
3	4	3	-	-	-	-
4	7	0	50/50/70	10/63/98	19.2	48.4
5	7	3	-	75/100/93	53.7	45.7
6	3	9	-	-	-	-
7	6	0	90/100/100	-	64.3	-
8	7	2	50/75/65	75/75/90	27.5	-
9	9	0	-	100/100/100	40.2	58.5
10	6	0	100/100/90	80/75/84	35	41.7
11	6	7	-	70/50/65	-	33.6
12	9	6	80/50/58	100/75/97	33.5	59
13	3.5	4	41/100/92	80/75/80	37.5	40.4
14	3	3	65/75/81	85/88/95	-	50.4
15	7	5	65/75/65	75/38/65	34.6	28.3
16	7	1	30/25/43	70/75/97	-	51.3
17	8.2	1	65/75/79	100/88/100	41.9	54.4
18	6	0	75/63/98	100/100/100	-	57.6
19	2	3	85/75/79	100/75/72	46.3	42

Table 5 – Clinical outcome scores for each patient. Incomplete scores are marked by a dash.

Five of the six patients that had an increase in maximum contact stress had an increase in the acetabular anteversion angle which is measured on a transverse plane viewed inferior to superior using a vertical line and a line between the posterior and anterior rim of the acetabulum, at the level of the femoral head center. An increase in the acetabular anteversion angle causes the patient to have less anterior coverage of the femoral head, reducing the contact area (Table 6).

Patient ID	Pre-Op AV Angle (˚)	Post-Op AV Angle (˚)
2	4.69	17.76
3	10.14	11
6	14.01	20.03
10	11.59	9.75
11	5.04	9.31
13	16.09	29.03

Table 6 – Acetabular anteversion (AV) angles for the six patients that had an increase in maximum contact stress. A higher AV angle indicates less anterior coverage of the femoral head which reduces the contact area, causing elevated contact stress.

For patients with CE angles below the normal range (<25˚), the maximum contact stress tended to decrease as the CE angle increased. Throughout the normal CE range (25˚- 40˚), the maximum contact stress remained relatively constant with most patients experiencing between 6 and 8 MPa. The patient with the highest post-operative contact stress had a CE angle of 44˚, suggesting contact stress may increase at CE angles above the normal range. Figure 36 shows a plot of the maximum contact stress vs. CE angle with a 2nd order polynomial best fit which had an R value of 0.653 and standard error of 1.512.

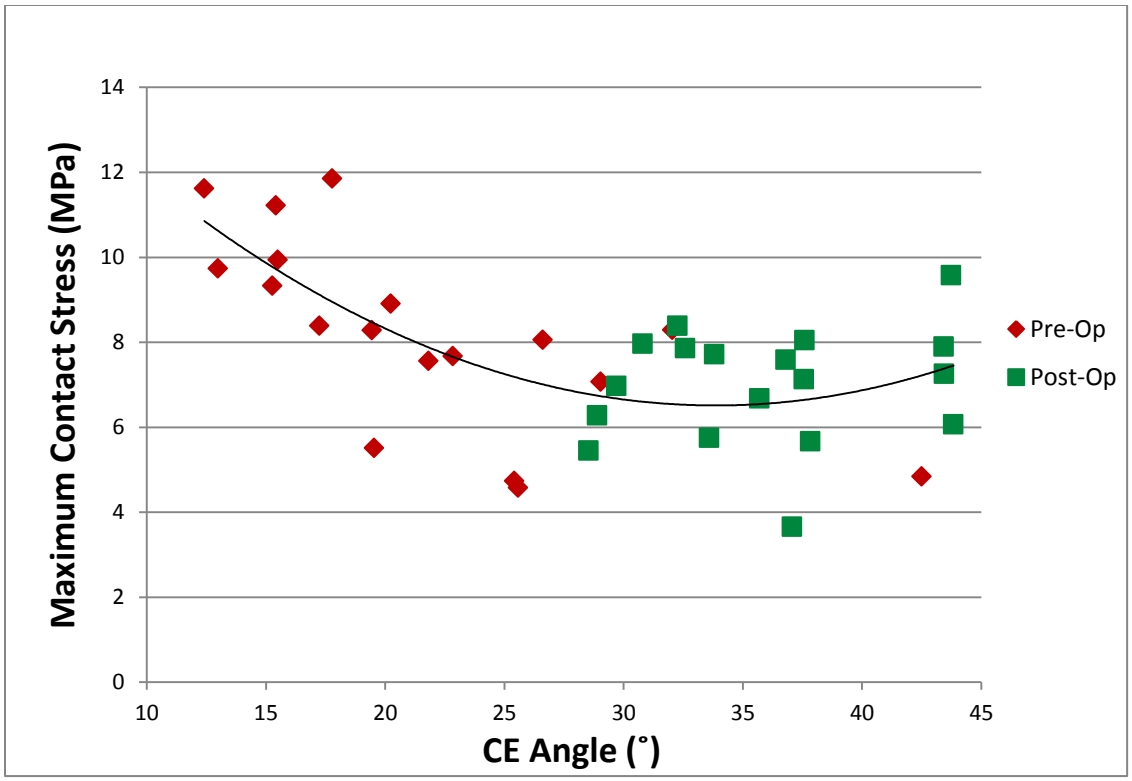

Figure 36 – Plot of the maximum contact stress vs. center-edge angle for pre-op (red) and post-op (green) cases.

3.4 Discussion of Results

In this study we examined the contact area and contact stress distributions of 19 patients who underwent periacetabular osteotomy. The goal of this study was to characterize PAO-induced changes in joint mechanics using DEA and correlate changes with short-term patient outcomes. Averaging the maximum contact stress for all patients showed a 12% decrease from pre-operatively (8.20±2.26 MPa) to post-operatively (7.24±1.68 MPa). This decrease in maximum contact stress was smaller than expected due to predictions of increased contact stress in four of the 19 patients. Also, the reported values do not take into account at what phase of the gait cycle the maximum contact stress occurred. These maximum stress values have similar magnitude as those reported in other DEA and FEA contact studies of PAO patients [50, 52, 53, 88] as well as *in vivo*

contact pressure measurements obtained from an instrumented femoral head prosthesis which showed a peak pressure of 6.72 MPa during walking gait [91].

Comparisons of contact stress with clinical outcomes showed good correlation. Clinical followup was incomplete on several patients (SF-36 (n=11) and WOMAC (n=11)), causing these outcomes to correlate less with maximum stress than VAS pain scores (n=18). However, correlation of the data observed in this study showed the relationships between the change in maximum contact stress and change in all three clinical outcome scores were statistically significant ($p < 0.05$). Correlation between contact area and clinical outcome scores was statistically insignificant. Inclusion of more cases could further improve the correlation between clinical outcomes and mechanical results.

Results from patients who experienced an increase or minimal change in contact stress after PAO suggest that reorientation of the acetabulum does not necessarily guarantee lower contact stress, confirming the findings in previous studies [49, 52, 88]. One of those studies used FEA to find the patient-specific optimal CE angle that minimized contact stress and maximized contact area [88]. Their finite element model predicted a parabolic trend between maximum contact stress and CE angle, similar to Figure 36, which suggests there is a possibility of overcorrection. Armiger et al. used a DEA algorithm to asses contact stress before and after PAO [52]. The patient with the highest CE angle (19˚ pre-op, 42˚ post-op) was the only patient out of twelve that saw an increase in contact stress. The other post-operative CE angles ranged from 23˚-36˚. These findings indicate a possible “sweet spot” that is patient-specific. Janzen et al. investigated the three dimensional geometry of 15 subjects with normal hips and found a mean CE angle of 33 degrees with a 95% confidence interval of 23 – 43 degrees [73]. A parabolic fit between peak stress and CE angle in our results suggest a CE angle of 34 degrees for minimizing peak contact stress, which is very similar to the mean CE angle in normal hips.

Although the lateral coverage of the femoral head is often the major focus of PAOs, the anterior coverage also plays a pivotal role in hip joint biomechanics. Cases with an increase or very little change in contact stress could be due to insufficient anterior coverage. In the study done by Armiger et al., the patient that saw an increase in contact stress not only had the highest CE angle but also saw the largest decrease in anterior coverage out of all 12 patients. In our results, 5 of the 6 patients who had an increase in maximum contact stress also had a decrease in anterior coverage. The post-operative maximum contact stress was located along the anterior rim of the acetabulum in every subject that had a decrease in anterior coverage post-operatively. The only one of our patients who had an increase in both maximum contact stress and anterior coverage had peak contact stresses located medially on the acetabulum. This patient also had a pre-operative CE angle of 26˚, which is in the normal range, and a post-operative CE angle of 38˚. Due to a high post-op CE angle and peak stresses located medially, the increase in maximum contact stress for this patient is likely due to overcorrection of lateral coverage instead of insufficient anterior coverage.

DEA is unable to accurately model the mechanical response of soft tissues so the DEA model in this work lacked a labrum, the fibrocartilaginous lining along the acetabular rim. In cases with minimal lateral coverage of the femoral head, a greater portion of the load is transferred through the labrum. A finite element study found that the labrum supports 4-11% of the total load transferred through the joint in dysplastic hips compared to only 1-2% of the load in normal hips [92]. However, there were insignificant changes in cartilage contact stress when the labrum was removed from the FEA model for both the normal and dysplastic hips. An experimental study also found no significant changes in cartilage contact stresses in cadaveric hips after removal of the labrum, suggesting that the labrum functions to stabilize the joint, not to decrease cartilage contact stresses during normal daily activities [93].

One limitation of this study was the requirement to approximate the cartilage thickness values based on the distance between the subchondral bone and articular cartilage surface. In order to implement actual patient-specific cartilage thickness values, either a MRI scan or a CT scan with contrast injected into the joint space would be needed. Another factor to consider is that the clinical follow up times varied a considerable amount, ranging from 0.4 years to 3.6 years. This variability in follow-up time enables the patients to be exposed to PAO-induced changes in joint mechanics for different durations of time which may have an effect on their clinical outcome scores.

DEA was able to predict contact stress in 18 of the 19 patients. The one patient the DEA model was not able to converge on had a center-edge angle of 3˚ which caused extremely high pressures on the lateral rim of the acetabular cartilage that were unable to balance the force equilibrium. The DEA model was able to converge on other patients with center-edge angles as low as 12˚. The good correlation between DEA estimated contact stress and clinical outcome scores indicate DEA is a useful computational modeling technique for evaluating joint mechanics in patients with developmental dysplasia of the hip. By comparing pre-operative and post-operative joint mechanics, we can obtain better understanding of the effect that PAOs have on reducing contact stresses in the hip joint and improving patient outcome.

CHAPTER 4: SUMMARY & APPLICATIONS OF DISCRETE ELEMENT ANALYSIS

Discrete element analysis is a clinically applicable computational method of calculating joint contact stress. Subject-specific models can be generated to assess the contact stress unique to a given patient's anatomy. By validating the DEA model in a variety of anatomical poses for healthy and fractured hip joints, it was shown that this computational method can yield useful numeric data for multiple applications. One of the proposed applications is assessing patient risk for PTOA development. It is known that elevated joint contact stress is a critically important risk factor for PTOA development. Hip dysplasia and residual articular incongruities following intra-articular fractures are two known causes of elevated joint contact stress [5-7, 24, 25, 74]. Patients with acetabular fractures or hip dysplasia who are at risk of developing PTOA could potentially be diagnosed by utilizing DEA to detect elevated contact stress.

To demonstrate the ability of DEA to predict contact stress in acetabular fractures, post-operative CT scans of three patients with reduced acetabular fractures were analyzed. The subject-specific models were created using the same methodology as described previously for PAO subjects. For these subjects the intact contralateral side of the hip was used as a baseline for contact stress comparison. The first subject had a posterior wall fracture similar to Specimen #1 in the validation study (Figure 37). As expected, DEA predicted significantly higher contact stress and lower contact area for the fractured hip (Figure 39) than the intact contralateral side (Figure 38). The maximum contact stress for the fractured hip was 7.98 MPa compared to 4.19 MPa in the intact contralateral hip, a 90% increase (Figure 40). The average contact area for the fractured hip was 710 mm^2 compared to 1,289 mm^2 for the intact contralateral hip, a 45% decrease (Figure 41). DEA was able to predict contact stress in a variety of acetabular fracture severities (Figure 42).

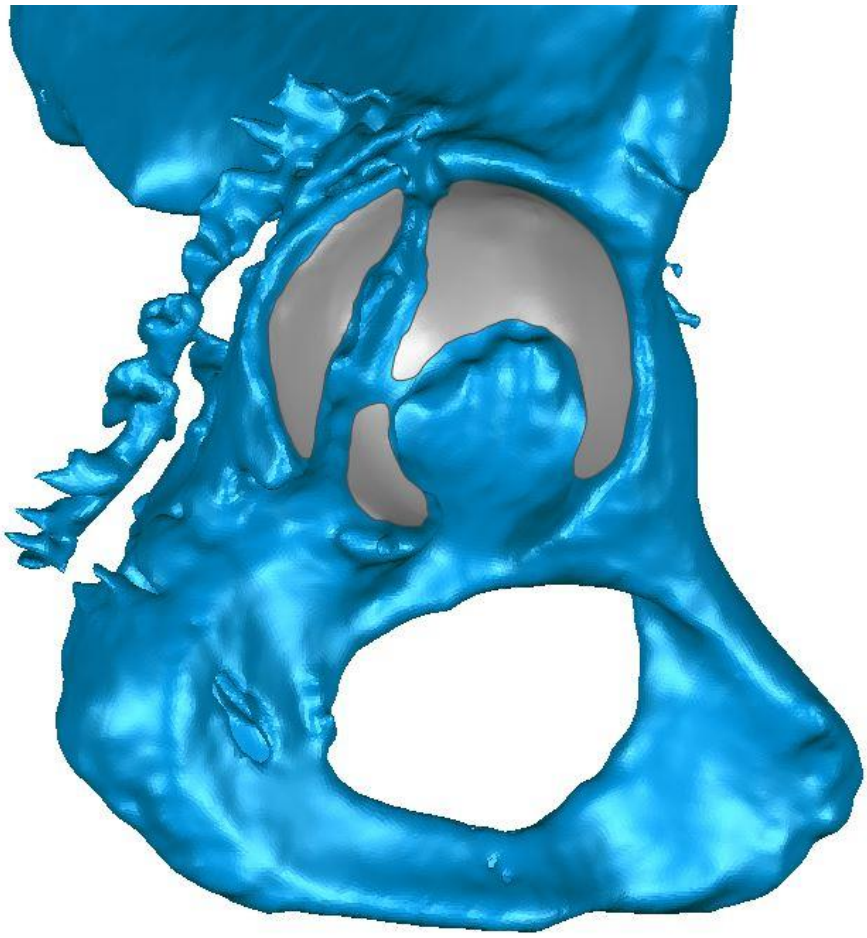

Figure 37 – Visualization of Fracture Subject #1's fractured hip. Cartilage is colored grey and the pelvis is colored blue. The fracture fixation hardware is the cause of the ragged segmentation artifact posterior to the acetabulum.

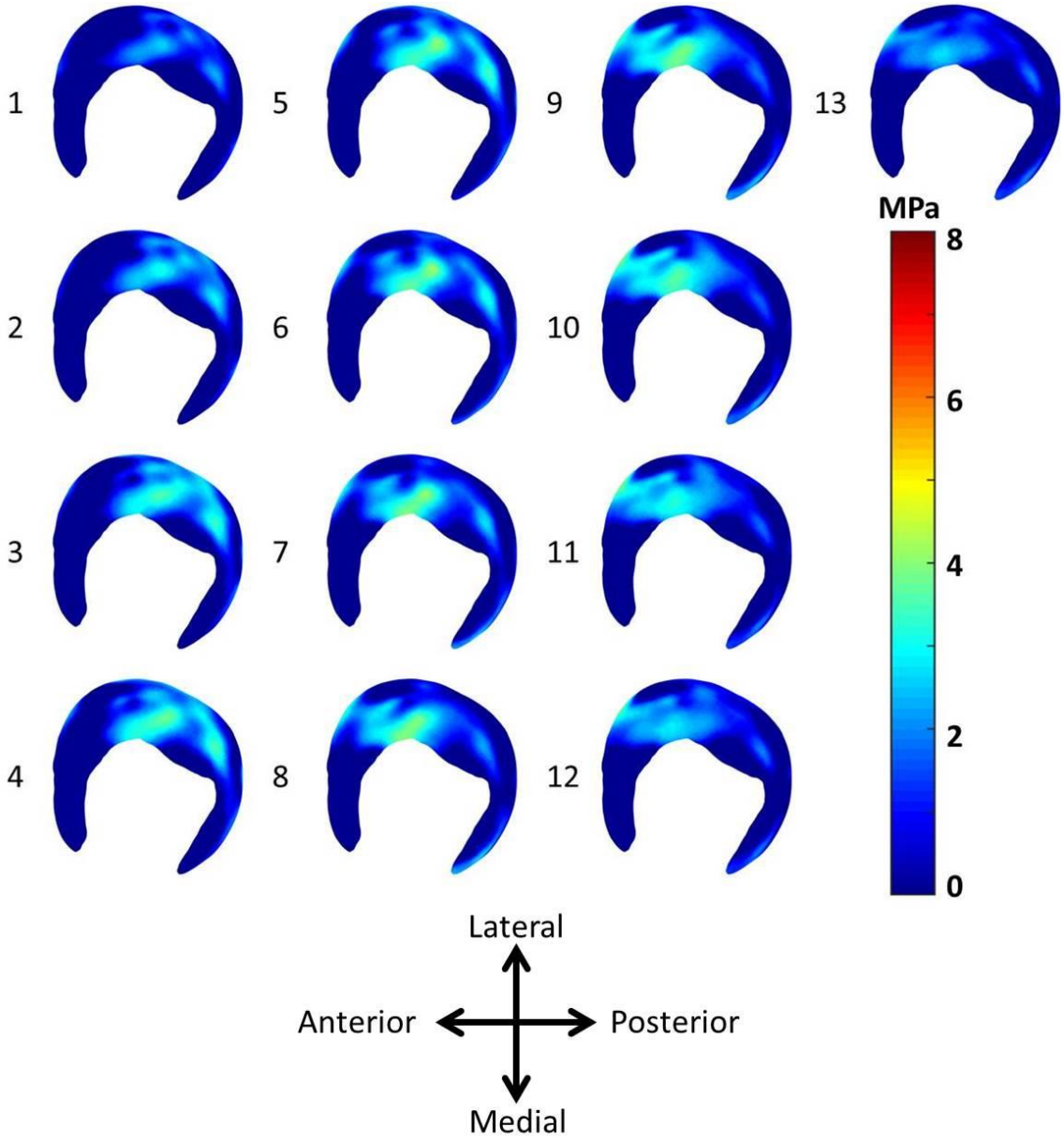

Figure 38 – DEA contact stress distributions on the intact contralateral side of Fracture Subject #1 during a walking gait cycle discretized into 13 steps. The contact stress is evenly distributed over a large contact area. The anterior direction points to the left.

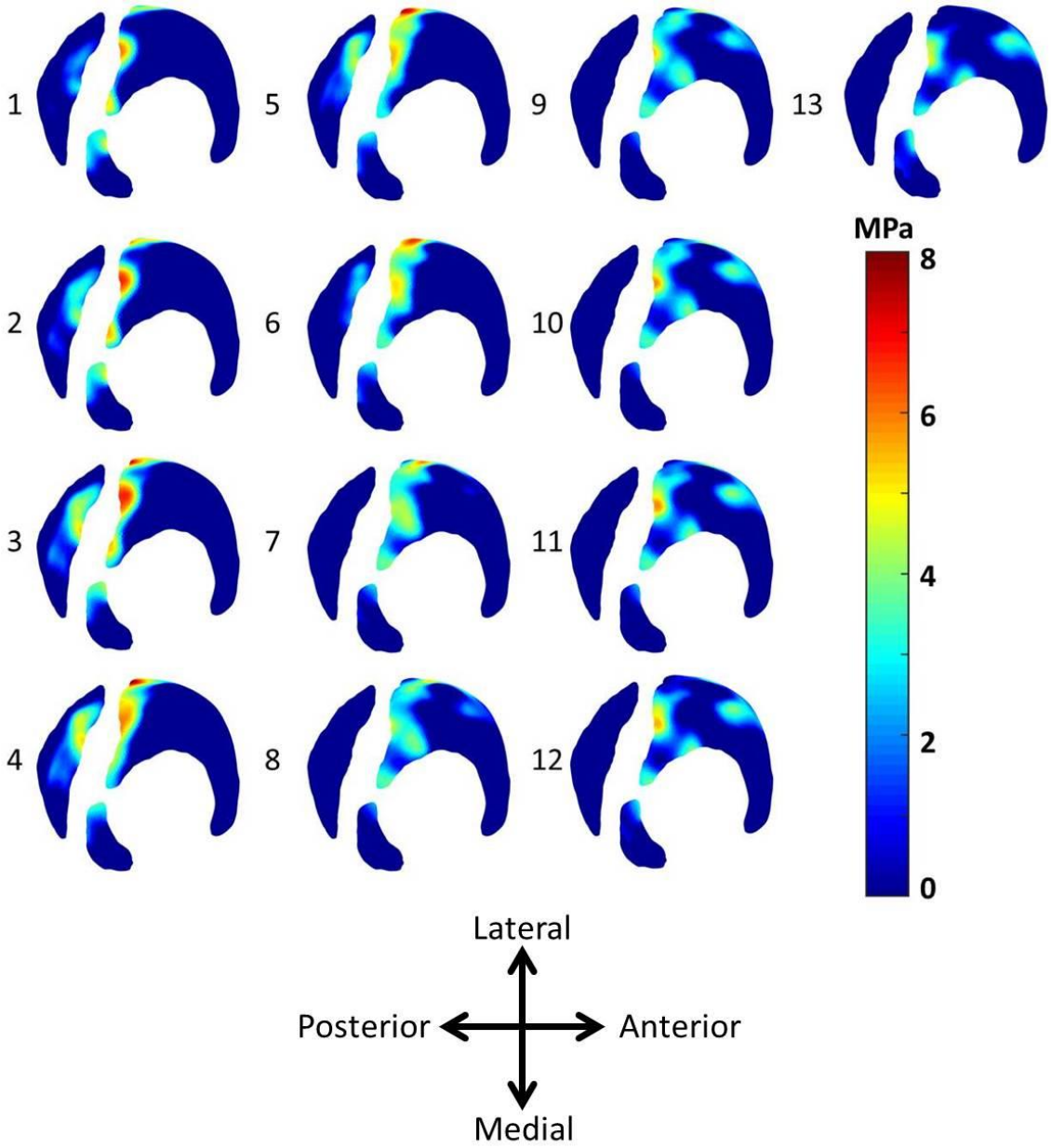

Figure 39 - DEA contact stress distributions on the fractured side of Fracture Subject #1 during a walking gait cycle discretized into 13 steps. The maximum contact stress tended to occur along the edges of the fracture lines due to the articular step-off. The anterior direction points to the right.

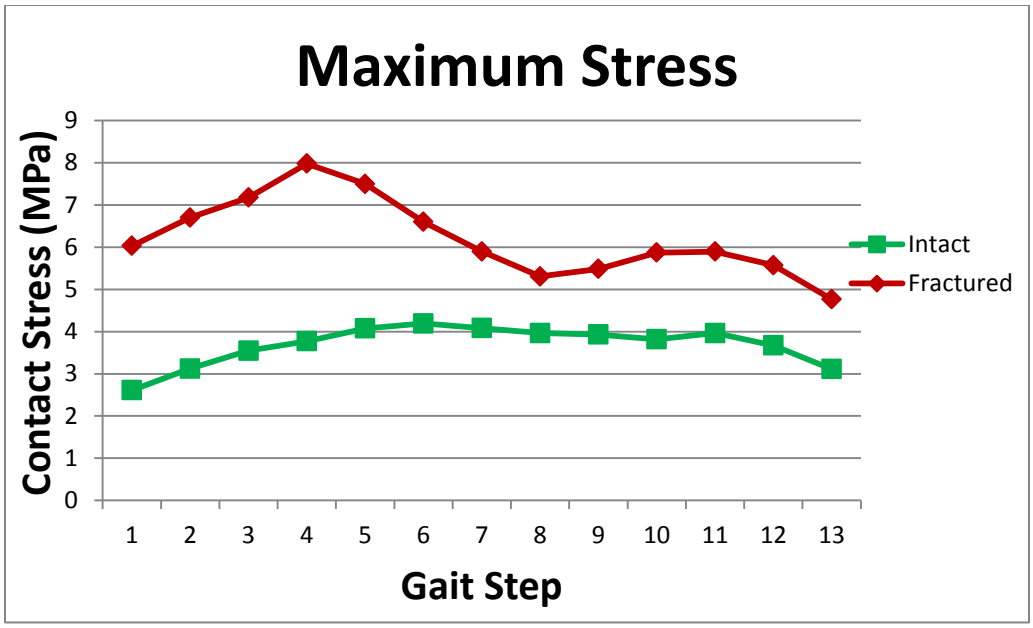

Figure 40 – Plot of the intact contralateral (green) and fractured (red) maximum contact stress for Fractured Specimen #1 at each step in the gait cycle. The step-off along the fracture line caused elevated contact stresses in the fractured case.

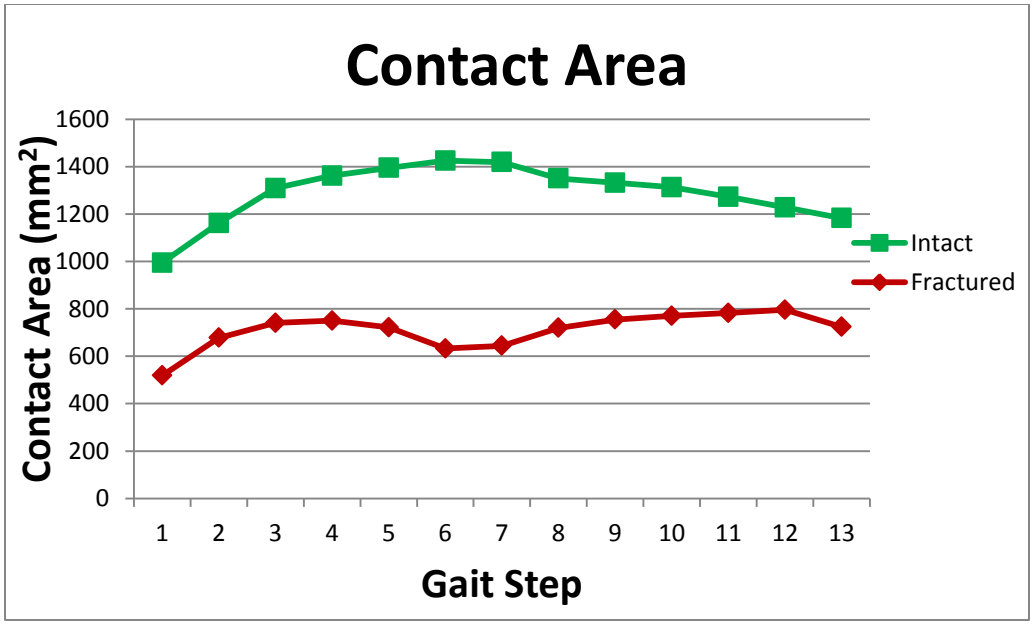

Figure 41 - Plot of the intact contralateral (green) and fractured (red) contact area for Fractured Specimen #1 at each step in the gait cycle. The fractured case had a lower contact area during the entire gait cycle due to the residual surface incongruities.

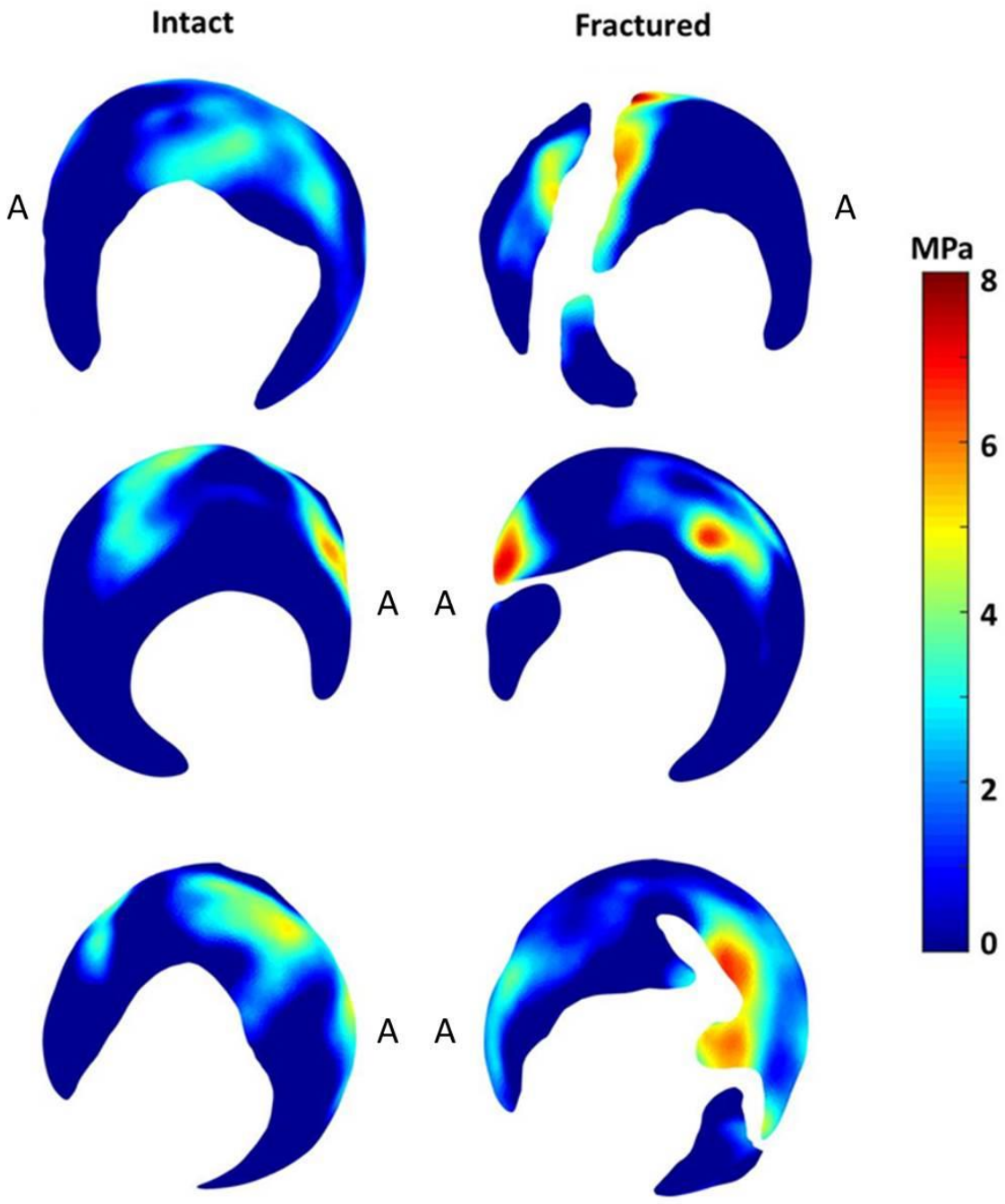

Figure 42 – DEA contact stress distributions at heel-strike of the intact contralateral (left column) and fractured hip (right column) for three different acetabular fracture patients. The top specimen was a fracture of the right hip, the middle and bottom specimens were fractures of the left hip. The plots are marked with an 'A' on the anterior side of the cartilage.

By utilizing a validated DEA model to compute contact stress in a large population of acetabular fractures, information can be gained that advances the understanding of elevated contact stresses and its role in all forms of OA. Furthermore, DEA can be used to develop and test methods of preventing elevated contact stress from joint incongruity and therefore improve patient outcomes. One possible method would be intra-operative techniques to assess the contact stress associated with candidate fracture reductions during operation. Surgically reducing a displaced intra-articular fracture to an anatomical state restores joint congruity, lessening the joint contact stress exposure. By giving the surgeon live feedback of the mechanical result of the fracture reduction, the surgeon can evaluate the quality of the candidate reduction and make an informed decision to adjust the reduction. Implementing this novel technique will require deducing fragment poses from intra-operative fluoroscopic images correlated with pre-operative CT models. However, due to the inherently fast computational time of DEA, this step would have minimal impact on the time duration of surgery.

Like all computational models there are some limitations to consider when using DEA. It is important to realize DEA tends to over-predict contact stresses and under-predict regions of low contact stress due to its inability to model cartilage as a poroelastic surface that deforms, or "squishes" outwards when pressure is applied. This attribute is most relevant along edges of contact surfaces.

The accuracy of the DEA model is largely dependent on several factors. First, the quality of bone and cartilage surfaces is dependent on the resolution of the CT and MRI imaging. In the validation study, the CT & MRI images had isotropic voxel spacing ranging from 0.35 – 0.5 mm. Larger voxel spacing generates greater stair-step segmentation artifact, reducing the quality of bone and cartilage models.

Secondly, cartilage material properties are dependent upon the rate at which load is applied. Assumptions must be made on the Young's modulus and Poisson's ratio, both

of which have a linear relationship with resultant contact stress magnitudes. The contact surfaces are also assumed to be frictionless.

Several assumptions were made regarding cartilage surfaces. For the acetabular fracture and PAO cases, only CT scans were available which cannot be used to accurately segment soft tissue such as cartilage. Therefore, a cartilage surface was approximated using a uniform projection from the subchondral bone. This creates a cartilage surface with constant thickness, which in reality, cartilage surfaces do not have. Therefore, a smoothing algorithm was used that approaches sphericity. The smoothing eliminates surface incongruities while also changing the cartilage thickness based on the new distance between the smooth cartilage surface and incongruent subchondral bone. The means by which the cartilage surface is smoothed greatly influences the DEA contact stress output. Image resolution is the root factor of what degree of surface smoothing will be needed. With a finite imaging resolution it is impossible to create a perfectly exact model of a patient's cartilage. An alternative method to uniform projection followed by smoothing would be an atlas-based definition of cartilage thickness. An atlas-based definition uses an estimated cartilage position template to register the target image to and propagate the atlas labels to the target image. Since the subjects in this study have either dysplastic or fractured hips that vary greatly in structure, registration to an estimated position would be very challenging.

The DEA algorithm used in this work has been previously validated in the knee [45] and ankle [46] but had yet to be validated in the hip. The ball-and-socket configuration of the hip causes unique modeling difficulties that are not present in the knee or the ankle. When imaging planar cartilage surfaces in the knee and ankle, image slices are orthogonal to the surface, creating discrete boundaries that are easier to segment than the curvilinear surface of the acetabular and femoral cartilage.

A limitation in this study is only walking gait was analyzed. Other activities of daily living such as running, sitting, or stair ascent/descent have different anatomical

motions and forces that were not validated in this study. The forces and rotations applied in the gait cycle for this study are from averaged data collected from instrumented hip implants of four elderly subjects (age 51-76) who do not have dysplastic hips or previous acetabular fractures. The inter-individual variation of forces and rotations indicate the average forces and rotations would change if more subjects were included. However, despite variations in loads applied, the DEA methodology was valid based on agreement with physical tests of different loading appositions.

Overall, it was seen that DEA is a stable and accurate computational model of contact stress in the hip joint. Validating DEA in the hip lays the foundation for future work applying the DEA method to diagnose patients at risk of OA development due to elevated contact stress, as well as the ability to develop and test clinically applicable intra-operative methods of preventing deleteriously elevated joint contact stress. Doing so will change the assessment and treatment of intra-articular fractures for the betterment of patients and healthcare system as a whole.

REFERENCES

1. March, L., et al., *Burden of disability due to musculoskeletal (MSK) disorders.* Best Pract Res Clin Rheumatol, 2014. **28**(3): p. 353-366.
2. Nho, S.J., et al., *The burden of hip osteoarthritis in the United States: epidemiologic and economic considerations.* J Am Acad Orthop Surg, 2013. **21 Suppl 1**: p. S1-6.
3. Buckwalter, J.A. and J.A. Martin, *Osteoarthritis.* Adv Drug Deliv Rev, 2006. **58**(2): p. 150-67.
4. Bitton, R., *The economic burden of osteoarthritis.* Am J Manag Care, 2009. **15**(8 Suppl): p. S230-5.
5. Dezateux, C. and K. Rosendahl, *Developmental dysplasia of the hip.* Lancet, 2007. **369**(9572): p. 1541-52.
6. Moraleda, L., et al., *[Dysplasia in the development of the hip]*. Rev Esp Cir Ortop Traumatol, 2013. **57**(1): p. 67-77.
7. Storer, S.K. and D.L. Skaggs, *Developmental dysplasia of the hip.* Am Fam Physician, 2006. **74**(8): p. 1310-6.
8. Jin, H. and J.L. Lewis, *Determination of Poisson's ratio of articular cartilage by indentation using different-sized indenters.* J Biomech Eng, 2004. **126**(2): p. 138-45.
9. Barker, M.K. and B.B. Seedhom, *The relationship of the compressive modulus of articular cartilage with its deformation response to cyclic loading: does cartilage optimize its modulus so as to minimize the strains arising in it due to the prevalent loading regime?* Rheumatology (Oxford), 2001. **40**(3): p. 274-84.
10. Hurwitz, D.E., D.R. Sumner, and J.A. Block, *Bone density, dynamic joint loading and joint degeneration. A review.* Cells Tissues Organs, 2001. **169**(3): p. 201-9.
11. Lane, N.E. and J.A. Buckwalter, *Exercise and osteoarthritis.* Curr Opin Rheumatol, 1999. **11**(5): p. 413-6.
12. Sankar, W.N., et al., *Femoroacetabular impingement: defining the condition and its role in the pathophysiology of osteoarthritis.* J Am Acad Orthop Surg, 2013. **21 Suppl 1**: p. S7-S15.
13. Ganz, R., et al., *Femoroacetabular impingement: a cause for osteoarthritis of the hip.* Clin Orthop Relat Res, 2003(417): p. 112-20.
14. Brown, T.D., et al., *Posttraumatic osteoarthritis: a first estimate of incidence, prevalence, and burden of disease.* J Orthop Trauma, 2006. **20**(10): p. 739-44.
15. Bhandari, M., et al., *Predictors of clinical and radiological outcome in patients with fractures of the acetabulum and concomitant posterior dislocation of the hip.* J Bone Joint Surg Br, 2006. **88**(12): p. 1618-24.
16. Saterbak, A.M., et al., *Clinical failure after posterior wall acetabular fractures: the influence of initial fracture patterns.* J Orthop Trauma, 2000. **14**(4): p. 230-7.
17. Dwyer, M.K., et al., *The acetabular labrum regulates fluid circulation of the hip joint during functional activities.* Am J Sports Med, 2014. **42**(4): p. 812-9.
18. Kuhlman, G.S. and B.G. Domb, *Hip impingement: identifying and treating a common cause of hip pain.* Am Fam Physician, 2009. **80**(12): p. 1429-34.
19. Polkowski, G.G. and J.C. Clohisy, *Hip biomechanics.* Sports Med Arthrosc, 2010. **18**(2): p. 56-62.
20. Bergmann, G., et al., *Hip contact forces and gait patterns from routine activities.* J Biomech, 2001. **34**(7): p. 859-71.
21. Hashimoto, N., et al., *Dynamic analysis of the resultant force acting on the hip joint during level walking.* Artif Organs, 2005. **29**(5): p. 387-92.
22. Gu, D.Y., et al., *The shape of the acetabular cartilage surface and its role in hip joint contact stress.* Conf Proc IEEE Eng Med Biol Soc, 2010. **2010**: p. 3934-7.

23. Daniel, M., A. Iglic, and V. Kralj-Iglic, *The shape of acetabular cartilage optimizes hip contact stress distribution.* J Anat, 2005. **207**(1): p. 85-91.
24. Anderson, D.D., et al., *Contact stress distributions in malreduced intraarticular distal radius fractures.* J Orthop Trauma, 1996. **10**(5): p. 331-7.
25. Brown, T.D., et al., *Contact stress aberrations following imprecise reduction of simple tibial plateau fractures.* J Orthop Res, 1988. **6**(6): p. 851-62.
26. Anderson, D.D., et al., *Is elevated contact stress predictive of post-traumatic osteoarthritis for imprecisely reduced tibial plafond fractures?* J Orthop Res, 2011. **29**(1): p. 33-9.
27. Segal, N.A., et al., *Elevated tibiofemoral articular contact stress predicts risk for bone marrow lesions and cartilage damage at 30 months.* Osteoarthritis Cartilage, 2012. **20**(10): p. 1120-6.
28. Mavcic, B., et al., *Cumulative hip contact stress predicts osteoarthritis in DDH.* Clin Orthop Relat Res, 2008. **466**(4): p. 884-91.
29. Weinstein, S.L., *Natural history and treatment outcomes of childhood hip disorders.* Clin Orthop Relat Res, 1997(344): p. 227-42.
30. Kellgren, J.H. and J.S. Lawrence, *Radiological assessment of osteo-arthrosis.* Ann Rheum Dis, 1957. **16**(4): p. 494-502.
31. Altman, R., et al., *The American College of Rheumatology criteria for the classification and reporting of osteoarthritis of the hip.* Arthritis Rheum, 1991. **34**(5): p. 505-14.
32. Gossec, L., et al., *OARSI/OMERACT initiative to define states of severity and indication for joint replacement in hip and knee osteoarthritis. An OMERACT 10 Special Interest Group.* J Rheumatol, 2011. **38**(8): p. 1765-9.
33. Matta, J.M., *Fractures of the acetabulum: accuracy of reduction and clinical results in patients managed operatively within three weeks after the injury.* J Bone Joint Surg Am, 1996. **78**(11): p. 1632-45.
34. McKinley, T.O., et al., *Basic science of intra-articular fractures and posttraumatic osteoarthritis.* J Orthop Trauma, 2010. **24**(9): p. 567-70.
35. Freutel, M., et al., *Finite element modeling of soft tissues: material models, tissue interaction and challenges.* Clin Biomech (Bristol, Avon), 2014. **29**(4): p. 363-72.
36. Stewart, K.J., et al., *Implementing capsule representation in a total hip dislocation finite element model.* Iowa Orthop J, 2004. **24**: p. 1-8.
37. Anderson, A.E., et al., *Effects of idealized joint geometry on finite element predictions of cartilage contact stresses in the hip.* J Biomech, 2010. **43**(7): p. 1351-7.
38. Grosland, N.M., et al., *IA-FEMesh: an open-source, interactive, multiblock approach to anatomic finite element model development.* Comput Methods Programs Biomed, 2009. **94**(1): p. 96-107.
39. Blankevoort, L., et al., *Articular contact in a three-dimensional model of the knee.* J Biomech, 1991. **24**(11): p. 1019-31.
40. Schuind, F., et al., *Force and pressure transmission through the normal wrist. A theoretical two-dimensional study in the posteroanterior plane.* J Biomech, 1995. **28**(5): p. 587-601.
41. Fregly, B.J., et al., *Sensitivity of knee replacement contact calculations to kinematic measurement errors.* J Orthop Res, 2008. **26**(9): p. 1173-9.
42. Abraham, C.L., et al., *A new discrete element analysis method for predicting hip joint contact stresses.* J Biomech, 2013. **46**(6): p. 1121-7.
43. Kloosterman, G., *Contact methods in finite element solutions.* University of Twente, 2002.
44. Anderson, D.D., et al., *Physical validation of a patient-specific contact finite element model of the ankle.* J Biomech, 2007. **40**(8): p. 1662-9.
45. Stockman, T.J., *Early Targeting of Knee Osteoarthritis: Validation of Computational Methods.* University of Iowa, 2014.

46. Anderson, D.D., et al., *Implementation of discrete element analysis for subject-specific, population-wide investigations of habitual contact stress exposure.* J Appl Biomech, 2010. **26**(2): p. 215-23.
47. Elkins, J.M., et al., *The capsule's contribution to total hip construct stability--a finite element analysis.* J Orthop Res, 2011. **29**(11): p. 1642-8.
48. Henak, C.R., et al., *Specimen-specific predictions of contact stress under physiological loading in the human hip: validation and sensitivity studies.* Biomech Model Mechanobiol, 2014. **13**(2): p. 387-400.
49. Armand, M., et al., *Outcome of periacetabular osteotomy: joint contact pressure calculation using standing AP radiographs, 12 patients followed for average 2 years.* Acta Orthop, 2005. **76**(3): p. 303-13.
50. Yoshida, H., et al., *Three-dimensional dynamic hip contact area and pressure distribution during activities of daily living.* J Biomech, 2006. **39**(11): p. 1996-2004.
51. Genda, E., et al., *Normal hip joint contact pressure distribution in single-leg standing--effect of gender and anatomic parameters.* J Biomech, 2001. **34**(7): p. 895-905.
52. Armiger, R.S., et al., *Three-dimensional mechanical evaluation of joint contact pressure in 12 periacetabular osteotomy patients with 10-year follow-up.* Acta Orthop, 2009. **80**(2): p. 155-61.
53. Tsumura, H., et al., *A computer simulation of rotational acetabular osteotomy for dysplastic hip joint: does the optimal transposition of the acetabular fragment exist?* J Orthop Sci, 2005. **10**(2): p. 145-51.
54. Eckstein, F., et al., *Quantitative analysis of incongruity, contact areas and cartilage thickness in the human hip joint.* Acta Anat (Basel), 1997. **158**(3): p. 192-204.
55. Shepherd, D.E. and B.B. Seedhom, *Thickness of human articular cartilage in joints of the lower limb.* Ann Rheum Dis, 1999. **58**(1): p. 27-34.
56. Li, W., et al., *Human hip joint cartilage: MRI quantitative thickness and volume measurements discriminating acetabulum and femoral head.* IEEE Trans Biomed Eng, 2008. **55**(12): p. 2731-40.
57. Martin, C.T., Heiner A.D., Pugely A.J., Noiseux N., *Protrusion after medial acetabular wall breach in total hip arthroplasty.* Transactions of the 60th Annual Meeting of the Orthopaedic Research Society, 2014.
58. Rudert, M.J., et al., *A new sensor for measurement of dynamic contact stress in the hip.* J Biomech Eng, 2014. **136**(3): p. 035001.
59. Hartmann, J.M., et al., *Compliance-dependent load allocation between sensing versus non-sensing portions of a sheet-array contact stress sensor.* Iowa Orthop J, 2009. **29**: p. 43-7.
60. Kilburg, A.T., *Development of an Expedited Objective Fracture Severity Assessment Methodology.* University of Iowa, 2012.
61. Shivanna, K., *Automating Patient-Specific Diarthrodial Joint Contact Model Development.* University of Iowa, 2006.
62. Kern, A.M., *Large population evaluation of contact stress exposure in articular joints for prediction of osteoarthritis onset and progression.* University of Iowa, 2011.
63. Mechlenburg, I., et al., *Cartilage thickness in the hip measured by MRI and stereology before and after periacetabular osteotomy.* Clin Orthop Relat Res, 2010. **468**(7): p. 1884-90.
64. Shepherd, D.E. and B.B. Seedhom, *The 'instantaneous' compressive modulus of human articular cartilage in joints of the lower limb.* Rheumatology (Oxford), 1999. **38**(2): p. 124-32.
65. Olson, S.A., et al., *Biomechanical consequences of fracture and repair of the posterior wall of the acetabulum.* J Bone Joint Surg Am, 1995. **77**(8): p. 1184-92.

66. Malkani, A.L., et al., *Increased peak contact stress after incongruent reduction of transverse acetabular fractures: a cadaveric model.* J Trauma, 2001. **51**(4): p. 704-9.
67. Tateuchi, H., et al., *Compensatory turning strategies while walking in patients with hip osteoarthritis.* Gait Posture, 2014. **39**(4): p. 1133-7.
68. Jang, E.M., M.H. Kim, and W.G. Yoo, *Comparison of the Tibialis Anterior and Soleus Muscles Activities during the Sit-to-stand Movement with Hip Adduction and Hip Abduction in Elderly Females.* J Phys Ther Sci, 2014. **26**(7): p. 1045-7.
69. Ferber, R., I.M. Davis, and D.S. Williams, 3rd, *Gender differences in lower extremity mechanics during running.* Clin Biomech (Bristol, Avon), 2003. **18**(4): p. 350-7.
70. Ortolani, M., *Congenital hip dysplasia in the light of early and very early diagnosis.* Clin Orthop Relat Res, 1976(119): p. 6-10.
71. Barlow, T.G., *EARLY DIAGNOSIS AND TREATMENT OF CONGENITAL DISLOCATION OF THE HIP.* Proc R Soc Med, 1963. **56**: p. 804-6.
72. Murray, K.A. and J.R. Crim, *Radiographic imaging for treatment and follow-up of developmental dysplasia of the hip.* Semin Ultrasound CT MR, 2001. **22**(4): p. 306-40.
73. Janzen, D.L., et al., *Three-dimensional CT measurement of adult acetabular dysplasia: technique, preliminary results in normal subjects, and potential applications.* Skeletal Radiol, 1998. **27**(7): p. 352-8.
74. Tsumura, H., H. Miura, and Y. Iwamoto, *Three-dimensional pressure distribution of the human hip joint--comparison between normal hips and dysplastic hips.* Fukuoka Igaku Zasshi, 1998. **89**(4): p. 109-18.
75. Hipp, J.A., et al., *Planning acetabular redirection osteotomies based on joint contact pressures.* Clin Orthop Relat Res, 1999(364): p. 134-43.
76. Perry, K.I., R.T. Trousdale, and R.J. Sierra, *Hip dysplasia in the young adult: an osteotomy solution.* Bone Joint J, 2013. **95-B**(11 Suppl A): p. 21-5.
77. Furnes, O., et al., *Hip disease and the prognosis of total hip replacements. A review of 53,698 primary total hip replacements reported to the Norwegian Arthroplasty Register 1987-99.* J Bone Joint Surg Br, 2001. **83**(4): p. 579-86.
78. Pavlik, A., *The functional method of treatment using a harness with stirrups as the primary method of conservative therapy for infants with congenital dislocation of the hip. 1957.* Clin Orthop Relat Res, 1992(281): p. 4-10.
79. Grill, F., et al., *The Pavlik harness in the treatment of congenital dislocating hip: report on a multicenter study of the European Paediatric Orthopaedic Society.* J Pediatr Orthop, 1988. **8**(1): p. 1-8.
80. Ganz, R., et al., *A new periacetabular osteotomy for the treatment of hip dysplasias. Technique and preliminary results.* Clin Orthop Relat Res, 1988(232): p. 26-36.
81. Sutherland, D.H. and R. Greenfield, *Double innominate osteotomy.* J Bone Joint Surg Am, 1977. **59**(8): p. 1082-91.
82. Hopf, A., *[Hip acetabular displacement by double pelvic osteotomy in the treatment of hip joint dysplasia and subluxation in young people and adults].* Z Orthop Ihre Grenzgeb, 1966. **101**(4): p. 559-86.
83. Leitz, G. and R. Reck, *Necessarily disappointing results after tripleosteotomy in the dysplastic hip joint.* Arch Orthop Trauma Surg, 1979. **95**(4): p. 271-3.
84. Trumble, S.J., K.A. Mayo, and J.W. Mast, *The periacetabular osteotomy. Minimum 2 year followup in more than 100 hips.* Clin Orthop Relat Res, 1999(363): p. 54-63.
85. Mechlenburg, I., et al., *Changes in load-bearing area after Ganz periacetabular osteotomy evaluated by multislice CT scanning and stereology.* Acta Orthop Scand, 2004. **75**(2): p. 147-53.

86. Rab, G.T., *Lateral acetabular rotation improves anterior hip subluxation.* Clin Orthop Relat Res, 2007. **456**: p. 170-5.
87. Maeyama, A., et al., *Periacetabular osteotomy reduces the dynamic instability of dysplastic hips.* J Bone Joint Surg Br, 2009. **91**(11): p. 1438-42.
88. Zou, Z., et al., *Optimization of the position of the acetabulum in a ganz periacetabular osteotomy by finite element analysis.* J Orthop Res, 2013. **31**(3): p. 472-9.
89. Siebenrock, K.A., et al., *Anteverting periacetabular osteotomy for symptomatic acetabular retroversion: results at ten years.* J Bone Joint Surg Am, 2014. **96**(21): p. 1785-92.
90. Marchelli, G.L., et al., *Joint-specific distance thresholds for patient-specific approximations of articular cartilage modeling in the first ray of the foot.* Med Biol Eng Comput, 2014. **52**(9): p. 773-9.
91. Hodge, W.A., et al., *Contact pressures in the human hip joint measured in vivo.* Proc Natl Acad Sci U S A, 1986. **83**(9): p. 2879-83.
92. Henak, C.R., et al., *Role of the acetabular labrum in load support across the hip joint.* J Biomech, 2011. **44**(12): p. 2201-6.
93. Konrath, G.A., et al., *The role of the acetabular labrum and the transverse acetabular ligament in load transmission in the hip.* J Bone Joint Surg Am, 1998. **80**(12): p. 1781-8.